Pyramidal Cell Responses to Temporally Structured Stimuli: Experiments and Computer Simulations

Thesis by

Alexander D. Protopapas

In Partial Fulfillment of the Requirements
for the Degree of
Doctor of Philosophy

California Institute of Technology
Pasadena, California

1998
(Submitted December 9, 1997)

Acknowledgments

A hungry bear does not dance.

Greek proverb

Much like the bear in the proverb, I required nourishment to complete this work. There are many people who fed me intellectually and otherwise during the course of my stay at Caltech and I would like to thank those who made my experience here especially rewarding.

First I would like to thank my advisor Jim Bower who gave me all the freedom I wanted to pursue the research that I found most interesting. It is only now that I realize how lucky I was to be given the material support and encouragement to do the things that I enjoyed most.

I'd also like to thank Susan De Riemer, my undergraduate advisor, for encouraging me to continue in science and Apostolos Georgopoulos whose work had convinced me in those same naive years that the brain was a tractable problem.

My greatest thanks goes to the members of my lab past and present who challenged and entertained me with their thoughtful insights. To Karim Elaagouby, Upi Bhalla, Erik DeSchutter, and Dieter Jaeger I wish to express my gratitude for the advice on modeling and electrophysiology. I also want to thank Mitra Hartmann, Chris Assad, Fidel Santamaria, Mike Vanier, Hamid Bolouri, and Yoshi Kubota for enlightening scientific discussions and useful comments on various manuscripts and thesis chapters. Of course none of the work presented here would have been possible without the excellent systems support provided by Dave Bilitch, Venkat Jagadish, and John Uhley.

Finally I would like to thank my family and friends who provided me with emotional support throughout this entire endeavor. I could not have gotten to this point without the perseverance that my mother and father taught me. My brother Anthony

who chose to express his scientific talents through the Peace Corps has also been a constant inspiration to me. Lastly, but not leastly, I would like to thank my long-time friends Eric "Hoss" Haxthausen, Kevin Lyskowski, Joe Regal, Jon Unglaub, Liz Beuttner, and Mignon Belongie who had to put up with my complaining when things were not going well. In this regard I'd like to especially thank Alice Paquette who undoubtedly had to put up with more than her fair share.

Abstract

Oscillations in the field potential recorded from piriform cortex can be broadly categorized into slow and fast frequency ranges. The slow wave is correlated with respiration and sniffing. During respiration it is typically in the 1-4 Hz range but during sniffing it increases in frequency and is often referred to as the theta rhythm (4-12 Hz). The faster oscillations (30-50 Hz, also called gamma) appear in response to odor stimuli and are always modulated by the slower rhythm. Oscillations in the field potential are believed to reflect synchronized synaptic input to the dendrites of pyramidal neurons in the piriform cortex. In this thesis I use a combination of experimental and computer simulation techniques to study the consequences of pyramidal cell input meant to approximate the temporal characteristics of cortical oscillations.

Because the precise spatial and temporal control of synaptic inputs is not possible in an experimental preparation, I constructed a detailed biophysical simulation of a layer II pyramidal cell from piriform cortex where such control would be possible. The passive and active properties of this model were tuned to experimental measurements that I made from pyramidal cells *in vitro*. The model was able to match a wide range of physiological behavior including subthreshold oscillations and responses to multiple levels of current injection. Spatio-temporal patterns of synaptic input that have been suggested to underlie gamma oscillations in piriform cortex were then used as input to the model. The effects of a single such pattern of input were longer lasting than the duration of a single gamma oscillation suggesting that a pyramidal cell integrates input over multiple gamma oscillations during the course of bursts of gamma oscillations modulated by the respiratory / theta rhythm. When bursts of gamma activity in the model were separated by 650 $msec$ or more, the first burst had no effect on the second, implying that these neurons might be able to isolate the effects of sufficiently spaced sniffs or bouts of sniffing.

To determine how well current injections with the temporal characteristics of cor-

tical oscillations might be represented in the spike trains of pyramidal cells, I used a reconstruction algorithm to estimate the structure of the stimulus from spike train data. By comparing the estimate to the actual stimulus I was able to quantify the amount of stimulus information contained in the spike train. I found that stimuli filtered at frequencies of 0-10 Hz and 4-12 Hz were much better represented in the pyramidal cell spike trains than 0-40 Hz stimuli designed to include the entire frequency range of cortical oscillations. The effects of norepinephrine (a neuromodulator released during arousal) on spike coding were also studied. I found that while norepinephrine increased the amount of stimulus information in the spike train, a change in decoding strategy to extract this information from the spike train was not required.

Contents

List of Figures

List of Tables

1

Introduction

They have turned phlogiston into a vague principle which consequently adapts itself to all explanations for which it may be required. Sometimes this principle has weight, and sometimes it has not; sometimes it is free and sometimes it is fire combined with the earthly element; sometimes it passes through the pores of vessels and sometimes they are impervious to it. It is a veritable Proteus changing in form at each principle.

Antoine-Laurent Lavoisier (1743-1794)

Although the efforts of neurobiologists have been successful in correlating behavior to neural activity and localizing function within the brain, little progress has been made in producing a convincing theory of how neurons function in groups. In this sense, neurobiology is undeveloped relative to most of modern science because it lacks the central paradigms which seem to characterize other areas of scientific endeavor so well. There is nothing that approximates a periodic table as in chemistry, or quantum theory as in physics, or even a central dogma as in molecular biology. There are a few theories that appear to be universally accepted by neurobiologists such as the neuron doctrine which states that neurons are distinct cellular and computational elements in the brain (see Shepherd, 1991, for a history of this doctrine); however, there does not appear to be a universally accepted theory of how groups of neurons process or code information. Some progress has been made in the study of central pattern generators where much of the behavior that is seen experimentally has been successfully replicated in computer simulations (see Marder and Calabrese (1996)),

but often these simulations have been so complex that one may argue that they amount to moving a preparation from the electrophysiologist's recording chamber to the computer screen. Some efforts have been made to develop a quantitative theory of central pattern generators, but these are far from complete (Kopell, 1988). In the case of the mammalian brain, experimental data is sparse, computer simulations are crude, and mathematical theories are speculative at best.

In this sense, neuroscience is much like alchemy was before it became chemistry. Today's neuroscientists, much like the alchemists of the 17th century, have amassed a large but most likely inadequate amount of data in what has essentially been a theoretical vacuum. The absence of well constrained hypotheses meant that each alchemist could formulate his or her own hypothesis and the lack of data made most hypotheses equally plausible. In the worst cases, the dearth of data prompted many alchemists to ascribe supernatural causes to the phenomena they were observing. Unfortunately, some respected contemporary scientists have followed in this tradition by explaining the nebulous concept of consciousness through an evocation of dualism (Eccles 1994) and hitherto unformulated physical theories (Penrose 1989). More "mundane" but equally poorly constrained hypotheses of neural information processing have been developed around the cortical oscillations which are present in most brain areas.

The primary goal of this thesis is to help constrain some of these theories of cortical oscillations by asking what they mean in terms of the behavior of a single neuron in the piriform (olfactory) cortex. For the remainder of this chapter I will provide background on the piriform cortex and a summary of experimental and simulation data on cortical oscillations. I will then turn my attention to how I intend to clarify issues pertaining to oscillations and conclude with an overview of this thesis.

1.1 Cortical oscillations

1.1.1 Evidence of cortical oscillations

The term cortical oscillations refers to the rhythmic fluctuations that are seen in the electroencephalogram (EEG). Because the EEG falls under the rubric of field potential recordings, an understanding of the physical basis for field potentials is required before an interpretation of EEG data can be attempted.

The electric field around a neuron can be related to the extracellular current that is generated when a ligand- or voltage-gated conductance is activated. A neuron can be thought of as a complex circuit consisting of resistors, capacitors, and batteries and like any circuit it must obey Kirchoff's Law which states that the sum of all currents entering and leaving a node must equal zero. This means, for example, that a synaptic current entering the dendrite will necessarily have to exit somewhere to complete the circuit. The current generated extracellularly by this process is related to the field potential. A graphical depiction of this is shown in figure 1.1.

The EEG refers to field potential recordings made over a large cortical area using an array of electrodes or a single large electrode. Recordings are usually made from the cortical surface or the scalp. EEGs are typically classified according to their frequency which ranges from 1-100 Hz. In the following sections the discussion is restricted to gamma (30-50 Hz) and theta (4-12 Hz) frequencies.

One of the first examples of cortical oscillations was presented fifty-five years ago when Adrian recorded from the olfactory system of the hedgehog and found oscillatory activity in the olfactory bulb and piriform lobe in response to odor stimuli (Adrian 1942). Since then oscillations have also been observed in the visual, somatosensory, motor, and auditory cortices as well as in the hippocampus (see Ketchum and Haberly (1991) and Gray (1994) for comprehensive surveys). Furthermore, oscillations have recently been observed to occur in the brain areas of a number of invertebrate species as well (see Hildebrand and Shepherd (1997) for a review and comparison to cortical oscillations).

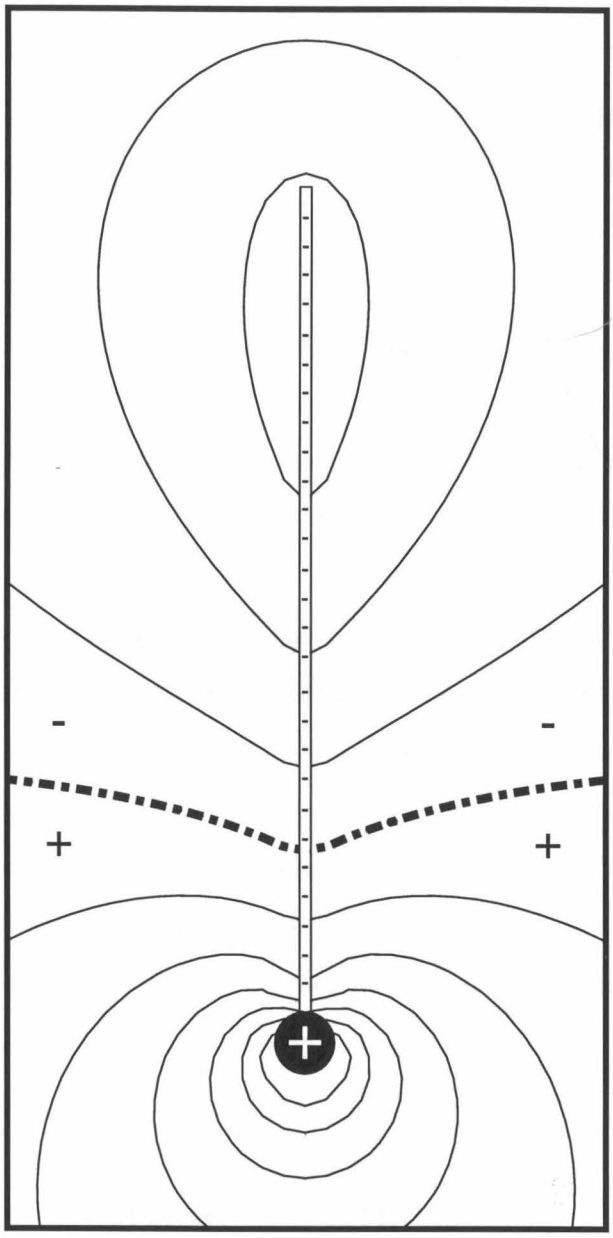

Figure 1.1: A model cell shows the distribution of current sources and sinks and extracellular isopotential contours at the moment when the cell is receiving excitatory input all along its apical dendrite. The thick contour shows the area of zero potential. Contour lines above the zero line give negative potentials. Below the zero line are positive potentials. Minus signs represent current sinks (current flowing into the cell) while the plus sign depicts a current source (current flowing out of the cell).

1.1.2 Oscillations and behavior

Since Adrian's early work, a number of studies (mostly by Freeman and colleagues) have examined the effects of different behaviors on the pattern of oscillations in piriform cortex. An early study by Freeman (1960) showed that spontaneous piriform cortex activity in the awake cat showed a slow wave in the EEG that correlated to the respiratory rhythm, on top of which bursts of fast oscillations (gamma frequency) were sometimes superimposed. An example of this data is shown in figure 1.2. Furthermore, he found that the presentation of meat, fish, and milk odors produced an increase in the amplitude of the fast oscillations in hungry, but not satiated cats. Results from Bressler (1988) demonstrated that the conditioning of stimuli also affected the oscillatory response of piriform cortex, further supporting the idea that context affects oscillations.

Results from other cortical areas suggest that oscillations arise primarily when the animal is attending. For example, Murthy and Fetz (1996) have found that oscillatory activity (20-40 Hz) occurred most often in sensorimotor cortices of the monkey during untrained exploratory behavior and much less often during trained repetitive wrist motions. Similarly, Nicolelis and colleagues (1995) found an increase in 7-12 Hz oscillations across areas in the brain stem, thalamus, and cortex of the rat during attentive states. Hippocampal studies in the rat have also revealed increases in theta (Ranck 1973) and gamma activity (Bragin et al. 1995) during exploratory behaviors.

1.1.3 Theories of cortical oscillations

The ubiquity of cortical oscillations has prompted many investigators to suggest that they must reflect some fundamental property of neural computation. In this section I briefly summarize different theories regarding the functional significance of oscillations.

The carrier wave hypothesis holds that amplitude modulated patterns of cortical oscillations reflect information processing. Bressler (1990) and Freeman and

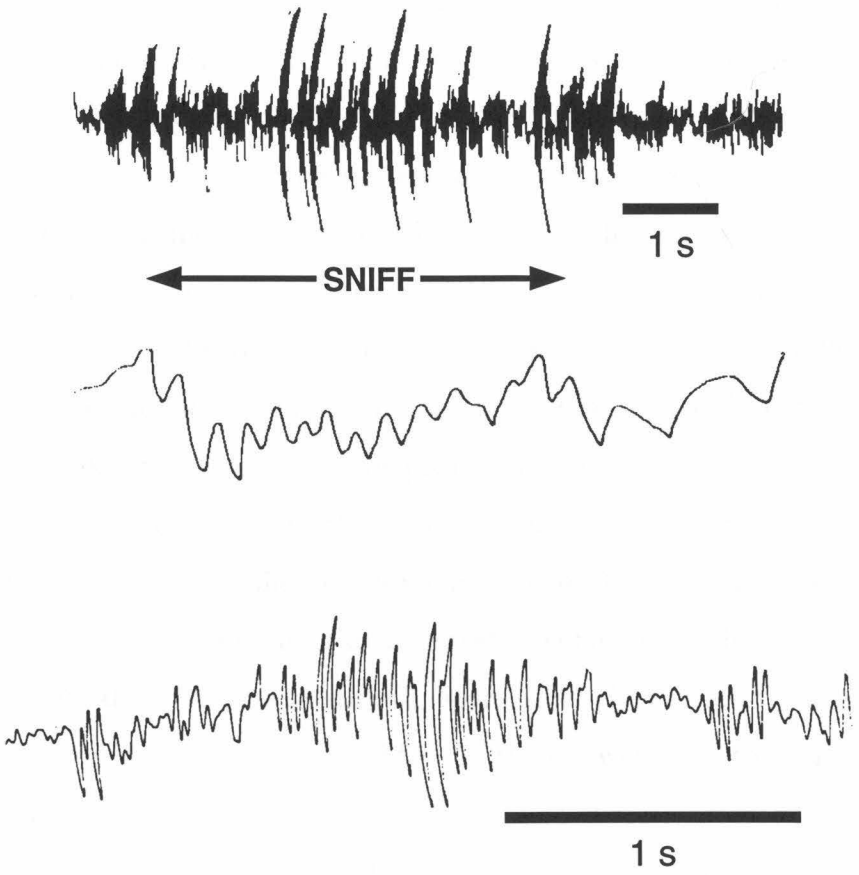

Figure 1.2: Examples of EEG recordings from awake-behaving cat (Freeman, 1960). Top trace shows EEG response when the cat is sniffing. Note how respiration/sniffing modulates fast oscillations (gamma frequency) into bursts. Bottom trace shows an EEG recording at greater temporal resolution.

colleagues (Freeman and Barrie 1994) are its main proponents. Recordings from electrode arrays over piriform cortex indicated changes in the spatial patterns of EEGs in response to conditioned stimuli (Bressler 1988) and earlier work by Freeman (1960) had indicated that the motivational state of the animal had a large effect on EEG activity. Findings such as these suggested that EEG patterns coded for the context of the stimulus as well as the stimulus itself (Freeman and Barrie 1994). Freeman then postulated that a perceptual state might be represented in limit cycle type attractors as revealed by EEG recordings (Freeman 1991). Later theoretical work suggested that perceptions might instead be represented by chaotic attractors (Freeman and Barrie 1994); however, more recent experimental work has discounted the possibility of even uncovering attractor dynamics from EEG recordings (Barrie et al. 1996). A less speculative interpretation of coherent oscillations by Bressler (1990) suggested that oscillations act to facilitate information transfer between different brain areas by synchronizing spikes that are bound for projection areas.

Despite the discovery of cortical stimulus induced oscillations in the 1940's, the present excitement over this phenomenon can be traced to an experimental study by Gray and colleagues in 1989 which demonstrated coherent oscillations in area 17 of the anesthetized cat in response to stimuli. More precisely, this study showed that two bars moving in concert across the visual field of the cat were able to elicit synchronous oscillations, but when the bars moved in opposite directions, oscillations became significantly less coherent. These results were interpreted in the context of an earlier theoretical paper by von der Malsburg and Schneider who had constructed an abstract model to demonstrate how auditory stimuli can be recognized in a noisy background (von der Malsburg and Schneider 1986). This work suggested that this could be accomplished through a synchronization of spikes among neurons that coded for the same stimulus. The authors further speculated that such a mechanism could account for "selective attention" in other sensory modalities as well. This idea was refined into the more popular binding hypothesis in a study that analyzed coherent oscillations in the cat visual system (Eckhorn et al. 1988) and found stimulus induced oscillations over distant areas of the visual cortex. Briefly stated, the binding hypothesis suggests

that different features of a single stimulus are "bound" together through synchronous neural activity in different brain areas.

In response to the speculation that coherent oscillations may represent a mechanism for binding stimulus features, Wilson and Bower (1991) constructed a biologically realistic model of visual cortex to study the function and generation of stimulus induced coherent oscillations. The main conclusion of this work was that oscillatory behavior is a natural outcome of network architecture and is not stimulus dependent. Furthermore, coherent oscillations only appear when repeated trials are averaged, suggesting that such a mechanism would not be sufficient for binding the features of a stimulus during a single trial. Instead, these authors speculate that oscillations act to coordinate neural activity within and between cortical areas.

A more recent theory goes one step further and suggests that gamma oscillations reflect the clocking of cortical computations (Jefferys et al. 1996). This work draws its inspiration from hippocampal experimental (Traub et al. 1996a, Whittington et al. 1995) and modeling (Traub et al. 1996b) studies which suggest that networks of inhibitory interneurons are tonically activated in the gamma range by slow excitation mediated by metabotropic glutamate receptors. These cells then form networks of interneurons that fire synchronously in the gamma range. The inhibitory network is able to sustain this oscillatory activity independent of fast excitation coming from pyramidal cells, but inhibitory cells are still able to entrain pyramidal cells through fast $GABA_A$ inhibition. This has led Jefferys, Traub, and Whittington (1996) to suggest that the inhibitory neurons act as "clocks" which synchronize the activity of pyramidal cells which play the role of "central processing units."

Other hypotheses implicate cortical oscillations in attention and learning. For example, Murthy and Fetz (1996) have found that exploratory behaviors induce gamma oscillations in the sensorimotor cortices of monkey. In one case, researchers have used the presence of oscillations during attentive behavior to speculate about their possible function as a hallmark for consciousness (Crick and Koch 1990). The learning hypothesis as put forth by Wolf Singer (1993) states that oscillations may act to modulate synaptic plasticity. For example, the degree of synchrony in cell firing that

would supposedly underlie oscillations could determine whether a synapse will show long term depression or long term potentiation. Thus, the plasticity of synapses may be determined by when synaptic input arrives relative to the phase of the oscillation.

1.1.4 Analysis and critique of oscillation hypotheses

One thing that should be clear from this brief review of cortical oscillations is that much like the phlogiston of Lavoisier's time they appear to have a certain protean quality about them. Some researchers see them when the animal is attending, others during the presentation of a particular stimulus, and still others when the animal is anesthetized. One difficulty in sorting out the different hypotheses of cortical oscillations is that they all appear somewhat vague and the veracity of one does not necessarily exclude the others. For example, there is no reason to imagine that if oscillations are involved in attentive behavior that they do not also reflect some kind of cortical clocking. Some assessment of the different hypotheses can be made by examining the experimental data. For example, both the binding and attention hypotheses are problematic because oscillations vary tremendously upon repeated presentation of a single stimulus (Freeman 1960, Freeman and Barrie 1994) and oscillations are apparently even present in the anesthetized cat (Gray et al. 1989).

The ideas that oscillations may simply reflect the coordination of neural activity, or the clocking of cortical computation, are attractive in that they do not appear to contradict any of the experimental data, yet taken to their logical extreme these theories would suggest that oscillations merely indicate that a particular cortical area is active. If this is indeed the case, then cortical oscillations as a ubiquitous phenomenon become considerably less interesting, unless we ask what kind of computations occur during the time scale of the oscillations in different brain areas. In order to do this we must understand the synaptic and single cell activity that underlie these oscillations. Given that different cortical areas have different neural architectures, we can be certain that the computations that underlie oscillations in different brain areas will also be different. However, the homogeneity within individual cortical regions might mean

that oscillations in a particular area may reflect a specific neural computation. In order to assess this possibility, however, we must first understand the neural activity that occurs during the course of a single oscillation. Luckily, such an understanding is possible under certain experimental conditions in the piriform cortex to which we now turn our attention.

1.2 Overview of the piriform cortex

In vertebrates, odorants come into contact with receptor cells in the nasal epithelium which then project to the olfactory bulb which in turn projects to piriform cortex (see Buck, 1996, for a review of vertebrate olfactory system). Piriform cortex makes strong feedback connections to the bulb as well. Projections from the piriform cortex also go to the olfactory tubercle, the olfactory peduncle, and the superior colliculus. Reciprocal connections are made with the amygdala and entorhinal cortex as well. The entorhinal cortex projects to the hippocampus, and it is believed that the piriform cortex's proximity to the hippocampus may explain the evocative nature of olfactory memory (Slotnick et al. 1991). Piriform cortex also projects to a neorcortical olfactory area in the orbitofrontal cortex via direct and transthalamic pathways. Neuromodulatory inputs come from basal forebrain (cholinergic) and brainstem (noradrenergic, serotonergic, and dopaminergic). The hypothalamus also provides input. Figure 1.3 summarizes piriform cortex connectivity to other brain areas. More complete reviews of piriform cortex connectivity can be obtained in Haberly (1990b) and Lynch and Granger (1991).

A number of features make piriform cortex unique among primary sensory cortical areas. Unlike primary auditory, visual, and somatosensory cortices, it receives its afferent input directly from the olfactory bulb, rather than via the thalamus. Also, it has a trilaminar structure in contrast to the six layered neocortex of primary cortices for other sensory modalities. Phylogenetically it is much older than neocortical areas and is commonly referred to as paleocortex. Interestingly, piriform cortex is surprisingly similar among reptiles and mammals (Haberly 1990a). This is striking when one

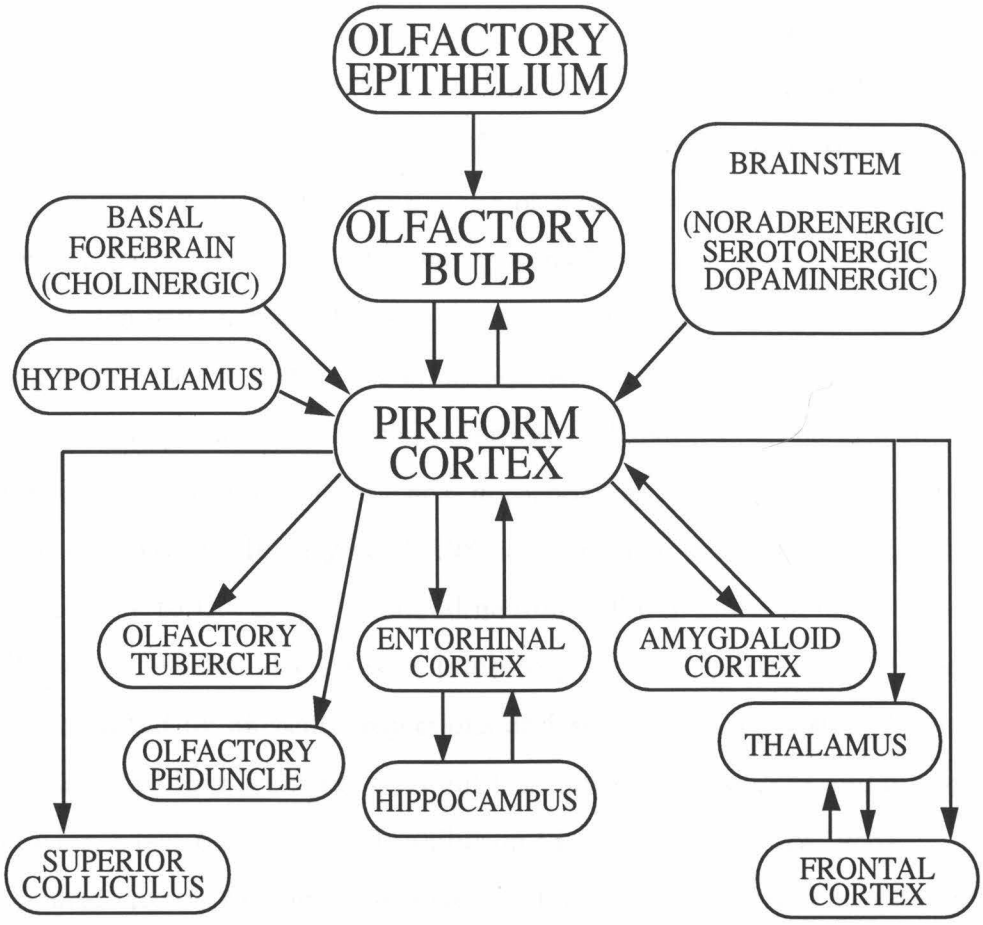

Figure 1.3: Piriform cortex connectivity to other brain areas.

compares the dramatic changes that have occurred in auditory, visual, and somatosensory cortices in the 200 million years since the evolutionary history of reptiles and mammals diverged, suggesting that perhaps piriform cortex has been in some sense optimized for solving the computational problems associated with olfaction (Haberly 1990a).

Piriform cortex also distinguishes itself as a key player in certain types of epilepsy. Its role in this disease is beyond the scope of this thesis and so a brief review of recent work in this regard has been placed in appendix A.

1.2.1 Neural architecture

Piriform cortex has three layers, typically labeled I, II, and III where I is the most superficial and III is the deepest. Superficial pyramidal cells, which are the subject

of this thesis, have their apical dendrites in layer I, their somata in layer II, and their basal dendrites in layer III (Haberly 1983). Deep pyramidal cells are oriented identically in piriform cortex except that their somata are located exclusively in layer III (Tseng and Haberly 1989b). Both types of pyramidal neurons are believed to be excitatory (Haberly 1990b). Multipolar neurons have their somata located in layer III but their dendritic arborizations are organized radially and are confined to layer III (Tseng and Haberly 1989b). It is unclear whether these neurons are excitatory or inhibitory. Many anatomically characterized multipolar neurons in layer III show the presence of GABA and glutamic acid decarboxylase (an enzyme necessary for the production of GABA) (Haberly et al. 1987); however, intracellular studies suggest a greater similarity to the deep pyramidal neurons (Tseng and Haberly 1989a) which are excitatory. Two broad classes of inhibitory neurons exist. One appears to be primarily activated by afferent projections and generates a very slow K^+-mediated inhibition and the other is excited by input from pyramidal neurons and is responsible for generating a fast Cl^--mediated inhibition (Tseng and Haberly 1988).

The neural circuitry of piriform cortex is illustrated in figure 1.4. Afferent input originating in the mitral and tufted cells of the bulb arrives in layer Ia of the piriform cortex where it makes contact with pyramidal cells and feedforward inhibitory cells (Price 1973, Haberly and Behan 1983). Pyramidal cells then send projections to other pyramidal cells within the piriform cortex (Heimer 1968, Haberly and Behan 1983, Haberly and Presto 1986). Caudally directed projections from rostrally located pyramidal cells terminate on the superficial Ib portion of pyramidal cell dendrites (Heimer 1968, Luskin and Price 1983). Likewise, rostrally directed projections from caudally located neurons terminate on the deep Ib portion of pyramidal cell dendrites (Luskin and Price 1983). Local excitatory connections appear to be made on the basal dendrites of pyramidal neurons (Haberly and Presto 1986). Multipolar neurons receive input from pyramidal cells and project to thalamus (Price et al. 1991). The feedforward K^+-mediated inhibition acts on pyramidal cell dendrites primarily in layer I (Tseng and Haberly 1988). A fast Cl^--mediated inhibition is active across the entire apical dendrite, but the inhibition present in the proximal dendrite and soma

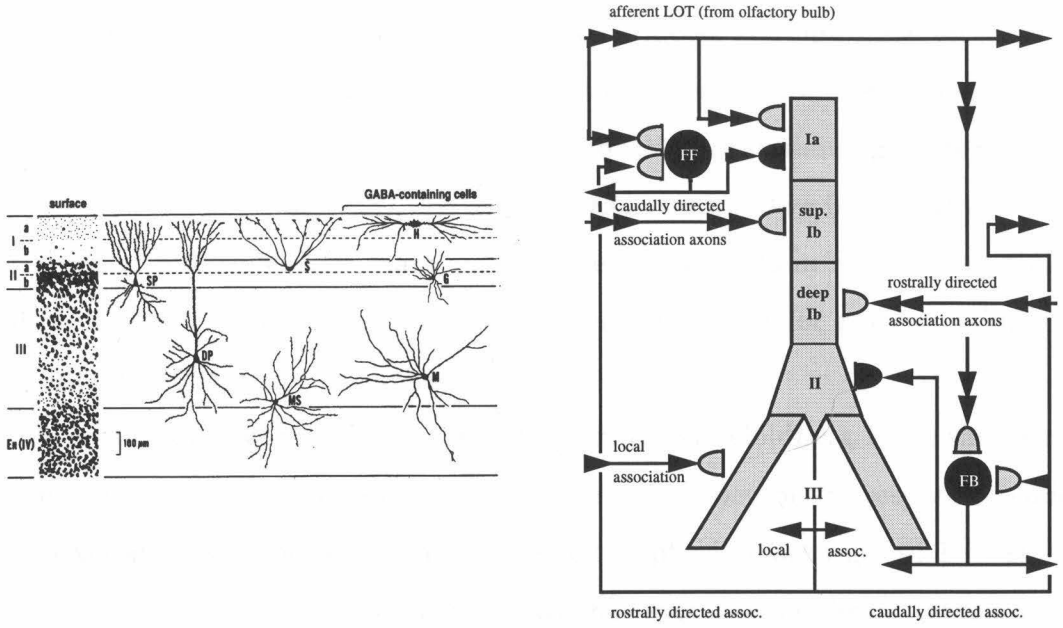

Figure 1.4: Left half shows morphology of different cell classes in piriform cortex and the anatomical layers where they are located. SP, superficial pyramidal cell; DP, deep pyramidal cell; MS, spiny multipolar cell; S, semilunar cell; H, superficial horizontal cell; G, small globular soma cell; M, multipolar aspiny cell. With the exception of SP, DP, and MS cells, almost nothing is known about the physiology of the other cell classes. Piriform cortex layers are shown on the left. En refers to the endopiriform nucleus. Left side of figure is adapted from Haberly, 1990b. The right side of the figure shows a simplified diagram of the neural circuitry impinging on an SP cell. FF and FB refer to feedforward and feed back inhibitory cells respectively. Single arrowheads signify local connections and double arrowheads signify distant ones.

appears to be controlled independently (Kanter et al. 1996).

1.2.2 Response to olfactory stimuli in the piriform cortex

Olfactory responses in piriform cortex have been characterized using a variety of methods. Human positron emission tomography (PET) studies show a bilateral activation of piriform cortex in response to odorant presentation (Zatorre et al. 1992), corroborating clinical evidence that had suggested the piriform cortex is involved in odor discrimination and identification (Levin et al. 1985, Zatorre and Jones-Gotman 1991). Technical barriers preventing the magnetic resonance imaging (MRI) of piriform cortex in the human brain have recently been overcome in a functional MRI study which agrees with the results of the PET study, but has higher spatial resolution

(Yang et al. 1997). Mapping studies using 2-deoxyglucose staining show an increase in piriform cortex activity in response to odor stimuli, but in contrast to neocortical studies using the same technique, there is no indication that staining patterns code for stimuli (Cattarelli et al. 1988). Extensive EEG studies have been performed by Walter Freeman and colleagues examining changes in the EEG in response to stimuli in several different behavioral contexts (see Freeman (1975) for review). Some of these results were discussed in section 1.1.2.

Single unit recordings in anesthetized rats (Nemitz and Goldberg 1983) show excitatory and suppressive responses of single piriform cortex neurons in response to odor stimuli. Excitatory responses typically consisted of phasic discharges of 1-12 spikes lasting up 1.2 s (Nemitz and Goldberg 1983); however, similar firing rates appear to be present in awake-behaving rats in the absence of odor stimulation (McCollum et al. 1991). A more comprehensive recent study examined the activity of piriform cortex single unit response to odorants in the context of reward following an olfactory discrimination task (Schoenbaum and Eichenbaum 1995). These researchers found that a minority of cells fired in response to single odors, while most fired in response to several different ones. Furthermore, activity was affected by identity and reward associations. Spiking rates appeared to be in agreement with previous studies (Nemitz and Goldberg 1983, McCollum et al. 1991). Experiments in awake-behaving and anesthetized monkey (Tanabe et al. 1975) yield results that are similar to those seen in rats, demonstrating broadly tuned excitatory and suppressive responses to odor stimuli.

1.2.3 Function within the olfactory system

The computational function of the piriform cortex within the olfactory system is ambiguous. Lesions in piriform cortex in humans interfere with the ability to identify, match, and discriminate between odors (Jones-Gotman and Zatorre 1993, Abraham and Mathai 1983, Eichenbaum et al. 1983, Jones-Gotman and Zatorre 1988) without abolishing the sense of smell or interfering with adaptation or discrimination of odor

intensity (Eichenbaum et al. 1983, Abraham and Mathai 1983). However, these results are difficult to interpret because lesions in orbitofrontal cortex appear to cause similar deficits (Potter and Butters 1980, Jones-Gotman and Zatorre 1993). Since piriform cortex projects to orbitofrontal cortex, it is unclear whether these deficits are specifically a result of piriform cortex damage or simply a lack of olfactory input to the orbitofrontal region.

Several hypotheses of piriform cortex computational function have also been developed on the basis of mathematical and biophysical models. None of these hypotheses contradict the lesion studies cited above, but they differ amongst themselves in terms of the computational mechanisms by which piriform cortex identifies different odors. Most of these models (Wilson and Bower 1988, Hasselmo et al. 1992, Barkai et al. 1994) contend that the piriform cortex acts as a kind of associative memory. In an associative memory, a set of patterns is stored in a network of neurons (artificial or biological) in such a way that when a new pattern is presented to the network, it reacts by producing the stored pattern which is most similar to the pattern that has been presented. In this sense, associative memories are content addressable, because they are able to recall stored patterns on the basis of the "content" of a presented pattern (Hertz et al. 1991). The contention that piriform cortex acts as an associative memory is partially based on perceived similarities between the neural architecture of piriform cortex and the connectivity patterns used in abstract models of neural networks (Hopfield 1982). For example, piriform cortex receives distributed input and pyramidal cells make dense connections with each other, attributes that are reminiscent of Hopfield-type networks (Haberly and Bower 1989). A more thorough assessment of computational models of piriform cortex function is presented in appendix B.

1.2.4 CSD analysis

I have just finished discussing the possible computational role of piriform cortex in odorant identification. Earlier in this chapter it was mentioned that fast oscillations

appear in the piriform cortex in response to odor stimuli. It would therefore be useful to understand the physiological behavior that might underlie these oscillations since this might provide insight into how piriform cortex accomplishes odor identification. Recent studies have moved in this direction by helping to elucidate the synaptic activity that may underlie fast oscillations. These are discussed below.

If a brain area has a laminar organization and the neural circuitry is well understood, current source density (CSD) analysis can be used to elucidate the spatio-temporal patterns of synaptic input that underlie field potential recordings. By calculating the gradient of the field potential along the depth of a brain structure, one can locate current sources and sinks in space and time. These current sources and sinks can then be correlated to currents induced by different synaptic pathways. It is thus possible to understand the synaptic activity that underlies the field potential. A more detailed explanation of this technique and its applications can be found in Mitzdorf (1985).

Haberly and colleagues have used the evoked potential induced by a strong shock to the LOT (piriform cortex afferent pathway) to perform a CSD analysis in the piriform cortex (Ketchum and Haberly 1993a, Rodriguez and Haberly 1989). They found a stereotyped spatio-temporal pattern of synaptic input in response to this stimulus. A systems model was then constructed to match CSD data with what is known about the spatial distribution of synaptic inputs on pyramidal neurons (Ketchum and Haberly 1993b). Although a strong shock to the LOT is a somewhat artificial stimulus, a weak shock is able to elicit an oscillatory field potential in the 40 Hz (i.e., gamma) range (Ketchum and Haberly 1993c). Interestingly, each oscillation appears to reflect the pattern of synaptic input seen in the strong shock case. A comparison of CSD results from strong and weak shock results is shown in figure 1.5. Ketchum and Haberly (1993c) have suggested that this pattern may also underlie the gamma oscillations seen in response to odor stimuli in awake-behaving animals. Surprisingly the patterns are almost identical in opossum (Rodriguez and Haberly 1989) and rat (Ketchum and Haberly 1993a) despite the approximately 100 million years that separate these animals phylogenetically. This suggests that this pattern of

synaptic input may be central to the computational function of the piriform cortex (Ketchum and Haberly 1993a). Chapter three of this thesis deals with the possible computational implications of this pattern of synaptic input.

1.3 Overview of this thesis

In this thesis I examine the response properties of a single layer II piriform pyramidal neuron using experimental slice techniques and a biologically realistic single cell simulation. The thrust of this work is to understand how single pyramidal cells respond to stimuli that are temporally structured to approximate the oscillations seen in piriform cortex.

Chapter 2 describes a detailed single cell simulation of a layer II pyramidal cell from piriform cortex. Model morphology was taken from an anatomical reconstruction of a stained neuron. Parameters describing the passive electrical properties of the neuron were derived from experimental data recorded in the lab. The simulation's behavior was tuned to match experiments showing subthreshold and suprathreshold behavior in pyramidal cells. Experimental and modeling results showing that the injection of current noise can increase and sustain subthreshold oscillations are also discussed. The work described here establishes the single cell model that is used to study the effects of physiologically plausible patterns of synaptic input in the next chapter.

Chapter 3 describes the single cell model's response to patterns of synaptic input believed to underlie the gamma oscillations seen in piriform cortex. The effects of this pattern of input on the electrotonic structure of the neuron and its somatic spiking patterns are discussed in detail. The possibility that spike timing may reveal information about the synaptic origin of input is also explored. Multiple iterations of the pattern believed to underlie gamma oscillations are repeated to simulate the gamma bursts seen riding on top of respiratory waves in the EEG of awake-behaving animals. Results demonstrate that the effects induced by individual gamma inputs is

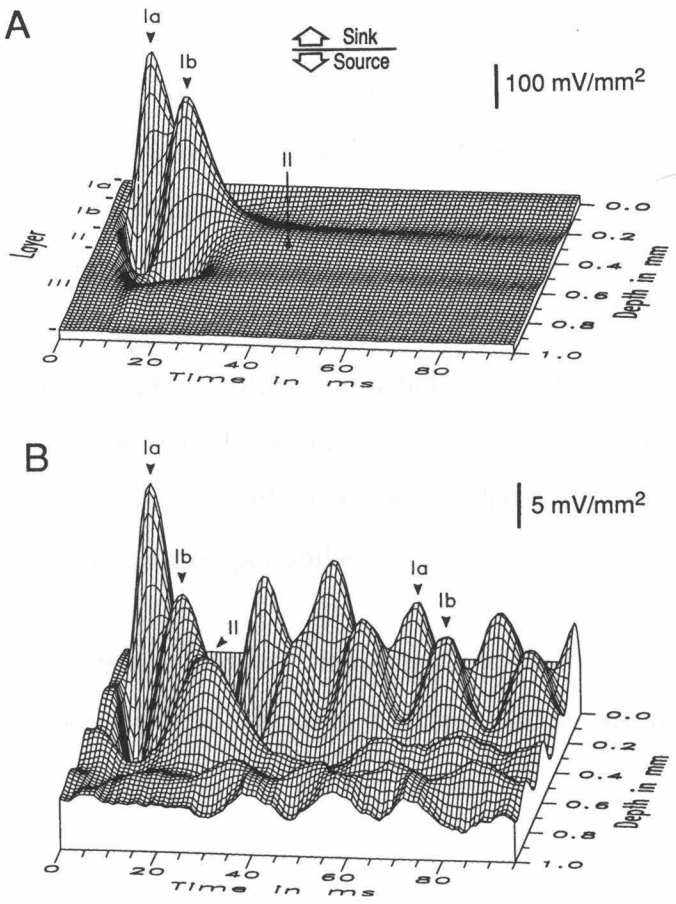

Figure 1.5: CSD results from strong (top) and weak (bottom) LOT shocks. Bottom trace is reminiscent of the fast oscillations seen in the EEG of awake-behaving animals and appears to be a repetition of CSD pattern seen in the strong shock case. CSD analysis allows one to deduce the pattern of synaptic input underlying field potential data. The pattern underlying this data is used as a stimulus for a single cell model in chapter 3. Top is taken from Ketchum and Haberly, 1993a, and bottom from Ketchum and Haberly, 1993b.

longer lasting than the duration of a single gamma oscillation. However, when bursts are separated by a sufficient amount of time, they are essentially independent of each other. The implications of this result in the context of the computational meaning of gamma and theta oscillations is discussed.

Chapter 4 uses information theoretic techniques to explore the extent to which spike trains from piriform cortex pyramidal cells can represent stimuli which approximate the temporal structure of cortical oscillations. Results showed that stimuli that were filtered at frequencies of 0-10 Hz and 4-12 Hz (approximating slow oscillations) were represented in spike trains twice as well as stimuli filtered at 0-40 Hz (meant to include all oscillation frequencies, including the gamma frequency). The effects of norepinephrine (a neuromodulator believed to be present during arousal) on spike coding were also explored. Norepinephrine was found to increase the amount of stimulus information in the spike train while decreasing the amount of stimulus information that is represented per spike.

Chapter 5 concludes this thesis with a summary of the contributions of this work to research in neuroscience and discusses directions for future research.

2

Realistic Simulation of a Pyramidal Cell Based on *In Vitro* Experiments

2.1 Abstract

We constructed a detailed compartmental model of a layer II piriform cortex pyramidal cell using a digital reconstruction of a stained neuron. The passive properties of the model were fitted to data that we collected from whole-cell recordings in slice. Active properties were modeled using only conductances experimentally shown or suggested to exist. The model is able to replicate a wide range of behavior seen experimentally including spike timing, spike shape, subthreshold oscillations, and dynamic response over a wide stimulus range. One aspect of pyramidal cell behavior that we were unable to initially model were the low frequency oscillations that follow brief spike trains. However, after adding noise to the current injection we were able to elicit the persistent oscillations seen experimentally. Experimental noise injections yielded similar results and also allowed us to quantify pyramidal cells' subthreshold frequency responses for comparison to our model. We conclude that our model is a good phenomenological representation of a pyramidal cell and discuss the possible role of noise in the real neuron.

2.2 Introduction

The primary purpose for constructing the model presented here was to test its response to patterns of synaptic input believed to underlie the cortical oscillations

described in chapter 1. However, in order to have confidence that the conclusions gleaned from such a simulation study could be applied to the biological system, it was necessary to build a model that was constrained by experimental data whenever possible. Therefore, we performed a number of *in vitro* experiments to parameterize the active and passive properties of the neuron that had not been described by previous experimental studies. Specifically, we felt that any realistic representation of a piriform cortex pyramidal cell would require the characterization of its passive properties using the whole-cell recording technique as well as a description of voltage-dependent subthreshold oscillations since these properties would undoubtedly affect a neuron's response to temporally structured stimuli.

Once tuned, parameters in the model were fixed, and it was used to explore the subthreshold membrane oscillations observed in these neurons. The model predicted and experiments confirmed that the presence of noise in the current injections used to stimulate simulated and real pyramidal cells was able to generate subthreshold oscillations in the 4-12 Hz range. This area of the frequency spectrum is biologically important because it falls into the range of the theta frequency which roughly approximates the rat's sniffing rate (Macrides et al. 1982) and slow EEG activity in the olfactory cortex (Woolley and Timiras 1965). This result suggests that unpatterned input in the piriform pyramidal neuron may still produce a patterned response (i.e., subthreshold oscillations in the theta frequency range) and underscores the importance of building realistic single cell models.

Previous efforts to model piriform cortex pyramidal cells have focused on the construction of simplified representations of neurons that were designed to only be used in network simulations (Wilson and Bower 1992, Barkai et al. 1994). In contrast to these studies, the model presented here is more realistic and able to match a wider range of physiological behavior including spiking behavior and subthreshold oscillations that match data from experimental recordings.

2.3 Methods

2.3.1 Experimental slice procedures

Slice preparation Female Sprague-Dawley rats of 3-5 months (for sharp recordings) and 6-8 weeks (for whole-cell recordings) in age were decapitated under ether anesthesia following procedures approved by the animal care and use committee at Caltech (protocol #1156). The brains were removed and bathed in cooled medium previously bubbled with 95% O_2 and 5% CO_2 during the slicing procedure. A vibratome (OTS 3000M) was used to cut five coronal 400 μm thick slices from every brain starting at 0.4 mm caudal to the anterior commissure. Slices were kept at room temperature in vials containing medium bubbled with the gas mixture described above for 2 hours before recording. The medium used to bathe the slices was made with distilled water and consisted of (in mM): $NaHCO_3$ 26, $NaCl$ 124, KCl 5, KH_2PO_4 1.2, $CaCl_2$ 2.4, $MgSO_4$ 1.3, and dextrose 10. In addition, kynurenic acid (661 μM) was added to the medium used to bathe the slices in the vials and during slicing to prevent neuronal damage due to excitotoxicity; however, medium without kynurenic acid was used to perfuse the slices during the course of experiments. During recording, the slice was placed at the bottom of a submersion-type slice chamber, with the temperature maintained at 31-34 °C. Medium passed through the chamber at a rate of approximately 2.5 ml/min. When channel blockers were added (see below), recordings were collected after perfusing the slice for six minutes which our measurements indicated was the time necessary for cell properties to stabilize. In those recordings where channel blockers were used, only one recording was made per slice.

Cell identification All recordings were made from Layer II of piriform cortex. This cell layer is clearly visible as a translucent strip when the slice is transilluminated and has been shown to contain the cell bodies of superficial pyramidal cells (Haberly 1985). In addition, the physiology of these neurons is well characterized (Barkai and Hasselmo 1994, Tseng and Haberly 1989a) to the extent that these neurons can be identified by their physiology alone. A schematic representation of the slice is shown

in figure 2.1.

2.3.2 Recording procedures

Intracellular recordings were performed using two different electrode techniques, whole-cell and sharp electrode. Neuronal spike trains used in calculating frequency vs. current (F/I) curves were obtained with sharp electrodes because their fine tips prevent the washout effects commonly seen with whole-cell electrodes (Horn and Marty 1988, Pusch and Neher 1988). The electrical leak introduced into the cell with sharp electrodes has little effect on action potential generation (Staley et al. 1992). Sharp electrodes were filled with 3 M potassium acetate solution and had impedances of 75-130 $M\Omega$.

Whole cell recording techniques were used for all other experimental procedures, as this technique minimizes disturbances of the neuron's passive electrical properties (Staley et al. 1992). Electrodes used for whole cell recording had impedances of 2.5-10.0 $M\Omega$ and were filled with one of two solutions. Solution 1 contained (in mM): potassium gluconate 140, $HEPES$ 10, $NaCl$ 10, $EGTA$ 0.2, $MgATP$ 2, and $NaGTP$ 0.2 with pH 7.5 adjusted with KOH and osmolarity of 300 $mosm$. Solution 2 contained (also in mM): potassium gluconate 120, KCl 10, $EGTA$ 10, $HEPES$ 10, $MgCl_2$ 2, $CaCl_2$ 2, Na_2ATP 2, with pH 7.3 adjusted with KOH and osmolarity 290 $mosm$ (Major et al. 1994). Both electrode solutions were passed through a 0.02 μm filter before use. More than one solution was used in order to explore the possible ways in which the solution could affect the behavior of the neuron. We found that changing electrode solutions had no effect on results. To account for the presence of diffusion potentials due to the use of gluconate electrode solutions, we subtracted 8 mV from our membrane potential recordings in accordance with a previous study that had measured this to be the diffusion potential for gluconate solutions (Zhang and Krnjević 1993).

A Neurodata two channel amplifier (Neurodata Instruments Corp., NY, NY) was used to inject current and record membrane potential for both sharp and whole-

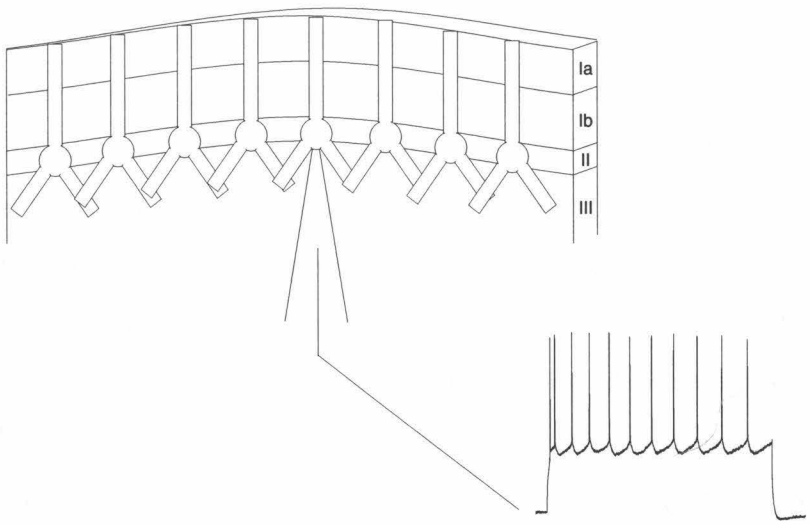

Figure 2.1: Diagram of slice recording. Whole-cell and sharp current clamp recordings are taken from layer II where the somata of superficial pyramidal cells are densely packed. Layer II is clearly discernible from the other layers during electrode placement.

cell recordings. For some whole-cell experiments, an Axoclamp 2A amplifier (Axon Instruments, Foster City, CA) was also used. Stimulation was controlled by software developed in our laboratory. Data was recorded on VHS videotape using a Neurodata 4 channel Neuro-Corder and digitized with a MetraByte A/D converter.

In order to minimize the effects of stray capacitance on the measurement of time constants, we used a wave function generator (Wavetek, San Diego, CA) to drive a sinusoidal current (1 kHz) through the electrode prior to entering the slice. By plotting current against voltage, Lisajous plots were obtained. A phase lag between the current and voltage traces was represented by an elliptical Lisajous figure and indicated the presence of uncompensated stray capacitance. Capacitance compensation and bridge balance were adjusted until the ellipse resembled a single horizontal line which indicated that the bridge was completely balanced and the electrode capacitance was completely compensated. This technique is similar to those used in other studies (Major et al. 1994, Park et al. 1983).

Stimulating with broadband noise We used broadband noise in our current injections to examine the subthreshold frequency response characteristics of piriform

pyramidal cells. White noise was generated using the *MATLAB* (Mathworks, Natick, MA) random number generator and was normally distributed around a mean of zero. The noise was then saved to a file and used repeatedly to stimulate the cell at different levels of depolarization. During stimulation, the noise stimulus was sampled at 10 kHz. Periods of depolarization lasted 4.0 s. Experiments were done using the whole-cell technique because patch electrodes responded better to fluctuating inputs, produced less noisy recordings, and preserved the electrical integrity of the neuron. However, as previously mentioned, whole-cell recording always raises the issue of wash-out, which may affect the active properties of the neuron. We ultimately decided that for this series of experiments this was the lesser of two evils.

Pharmacology To block synaptic currents in the pyramidal cell, we used 6-cyano-7-nitroquinoxaline-2,3-dione (CNQX) (Research Biochemicals International, Natick, MA) to block AMPA-type glutamate receptors, DL-2-amino-5-phosphonovaleric acid (APV) (Sigma, St. Louis, MO) to block NMDA-type glutamate receptors, and picrotoxin (PCTX) (Research Biochemicals International) to block $GABA_A$ receptors. Slices were always bathed for at least 6 minutes prior to recording.

For experiments where sodium channels were blocked, we used tetrodotoxin (TTX) (Research Biochemicals International). Recordings were started 6 minutes or more after the initial application to the bath, although TTX efficacy was often evident in 1-2 minutes following application when action potentials could no longer be elicited by depolarizing pulses. Cesium chloride was sometimes used with TTX as a general potassium channel blocker.

2.3.3 Analysis of experimental data

Complete current vs. voltage (I-V) curves were obtained for each cell by injecting a series of 600 $msec$ long current pulses into the cell. Injections generally started at -0.4 or -0.2 nA and proceeded by regular increments until the neuron began to fire. Up to 25 voltage traces were averaged for each current level to minimize the effects of noise. Trials containing spontaneous EPSPs were discarded so as not to affect time constant

calculations, although these were rare. Based on these measurements, cellular input resistance was calculated by taking the slope of the linear regression fit to the linear portion of the I-V curve. Values for τ_0 and τ_1 for charging and decaying portions of the pulses were obtained using the graphical method of exponential peeling (Rall 1969). We found the more general Levenberg-Marquardt method for nonlinear curve-fitting (Press et al. 1992) did not generate results that were as accurate. All curve fitting and exponential peeling was done on a Sun workstation using *MATLAB* and analysis software developed in the lab. Statistical analysis was done using EXCEL (Microsoft, Redmond, WA).

F/I curves were obtained by calculating the inverse of the interspike interval (in Hz) and plotting this against time of spike occurrence and magnitude of current injection in a three-dimensional plot.

2.3.4 Modeling techniques

Approach to modeling At the present time many single-cell simulations are considered realistic in the sense that they are constructed from realistic dendritic morphologies and possess passive and active membrane properties that have been experimentally determined. Nonetheless, many caveats come with this approach to "realistic" modeling. For example, voltage-clamp data often comes from experiments that were not done at body temperature. Even when care is taken to perform experiments under conditions that are as physiological as possible, the modeler is still left guessing with regards to the positioning of different currents in the model, the uniformity of membrane resistance, etc. Although our approach to constructing our single cell model is similar to others, we additionally require that our model closely match the integrative behavior of a real pyramidal cell. For example, instead of simply setting voltage-gated current densities and passive transient properties based on experimental data and setting channel densities so that the cell can simply spike, we require that our model be able to match a real pyramidal cell's behavior over multiple stimulus levels. Our matching requirements include realistic spike timings and spike

shape as well as subthreshold behavior. By adhering to these strict requirements, we feel more confident that our model can tell us something about the behavior of real pyramidal cells even if the biophysical details of our implementation are off.

Simulator Our pyramidal cell model was implemented on version 1.4 of the GENESIS neural simulator (Bower and Beeman 1995) using the Hines method of integration (Hines 1984) for the fast and accurate solutions of branched dendritic trees. Simulations were performed on several Sun SPARC 2, 10, and 20 workstations using a time step of 10 μs which produced numerically accurate results. It took approximately 10 minutes to generate 1.0 s of simulated activity on a SPARC 20 workstation.

Cell morphology The morphology of the model neuron was based on the digitized image of a biocytin stained layer II pyramidal cell (provided by Mark Domroese in the laboratory of Lew Haberly at the University of Wisconsin, Madison). The cell was digitally reconstructed using NED, a neural editing and tracing system developed in John Miller's laboratory at the University of California, Berkeley. The digital reconstruction was then converted into a model cell with 503 electrical compartments. The soma of the cell was represented by a single spherical compartment with a diameter of 10.43 μm. The digital reconstruction and electrotonic representation of the cell are shown in figure 2.2.

Modeling spines It has been shown previously (Larkman 1991) that dendritic spines constitute a significant portion of total neuronal membrane surface area, contributing significantly to the passive properties of cells (Wilson 1992, De Schutter and Bower 1994a). Accordingly, as in previous modeling efforts (Rapp et al. 1994, De Schutter and Bower 1994a), the passive effects of the spines were modeled in the current simulations by increasing the membrane area of dendritic regions where spines are known to exist. Unfortunately, the exact number of spines on piriform pyramidal cells is not yet known; therefore, spines were added to the model based on data from visual cortex pyramidal neurons indicating densities of 1.3 mm^{-1} of dendritic length (Larkman 1991). Consistent with previous anatomical work on piriform pyramidal

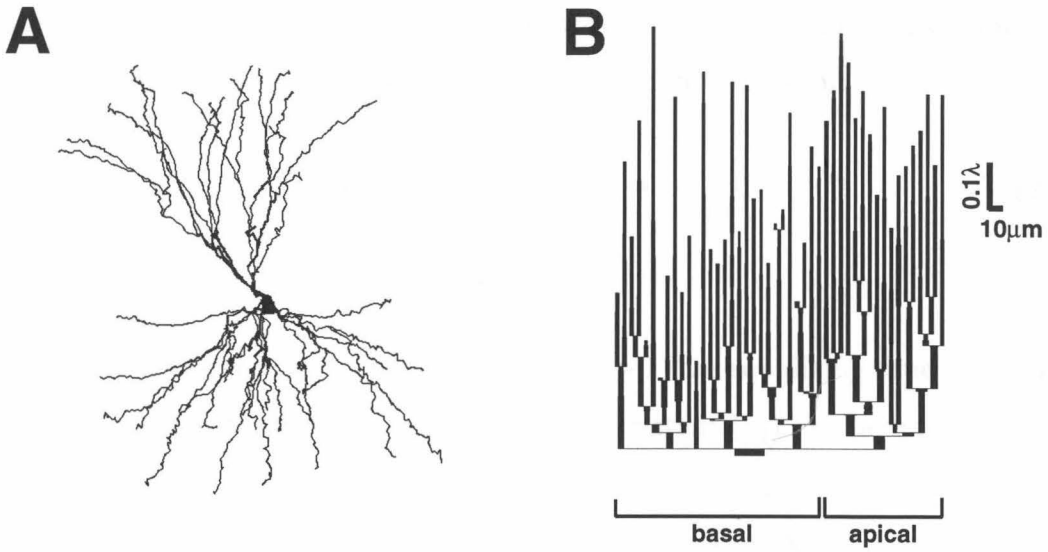

Figure 2.2: A: Digitized representation of the neuron morphology used in this simulation. B: A dendrogram representing the electrotonic structure of the model neuron. Note that the most distal portions of the apical and basal dendrites are approximately equidistant from the soma. Electrotonic distance from the most distal tips of the dendrites to the soma is approximately 1 λ.

cells (Haberly 1983), these spines were added evenly to the surface area of the basal and apical dendrites, but not on the apical trunk or soma, where spines are rare. The added area was calculated by modeling each spine as a cylinder with one closed end. Values for spine diameter (0.40 μm) (Haberly and Presto 1986) and length (0.75 μm) (Haberly 1983) were taken from anatomical studies of piriform pyramidal cells.

Calculating passive properties The passive properties of the model were established based on experimentally obtained values for input resistance (R_{in}), membrane time constant (τ_0), and first equalizing time constant (τ_1). Note again that experimental values for passive properties were obtained in slices bathed in Cs^+ and TTX in order to prevent the contamination of transient responses by voltage-gated currents. We arrived at a value for R_m (transmembrane resistance in units of $k\Omega \cdot cm^2$) by varying this parameter in the model until R_{in} was in the range of experimental values. The axial resistance had only a small effect on the value of R_{in}. Once this had been done, we were able to calculate a value for C_m based on τ_0 in the following way. Assuming a neuron is approximated as a cylinder of finite length with sealed

ends and is also considered entirely passive (with uniform axial and transmembrane resistance), decay transients can be expressed as the following sum:

$$V = C_0 e^{-t/\tau_0} + C_1 e^{-t/\tau_1} + C_0 e^{-t/\tau_0} + \cdots + C_n e^{-t/\tau_n} \tag{2.1}$$

(Rall, 1969)

where τ_0 is the membrane time constant, τ_n's (for n > 1) are equalizing time constants, and C_n represent constants. The membrane time constant (τ_0) can be expressed as:

$$\tau_0 = R_m C_m \tag{2.2}$$

where R_m is unit transmembrane resistance and C_m is unit membrane capacitance. Equalizing time constants represent the time it takes for charge to equalize over shorter lengths of cylinder as n increases (Rall 1989). Unlike τ_0, equalizing time constants also depend on axial resistance and so R_a was varied until we were able to obtain reasonable fits to the experimentally determined values for τ_1. Previous studies have used identical approaches to fit passive model parameters to experimental data (Rapp et al. 1994, Major et al. 1994).

Equations used to model voltage- and Ca^{2+}-dependent currents Voltage-gated currents were modeled using the standard Hodgkin-Huxley formalism (Hodgkin and Huxley 1952):

$$I_{ion} = m^p h^q z^r \bar{g}(E - E_{rev}) \tag{2.3}$$

where I_{ion} represents the current characterized by a particular ionic conductance, m is the voltage and time dependent activation gate, h is the voltage- and time-dependent inactivation gate, and z is the calcium- and time-dependent activation gate for calcium activated conductances. E is the membrane potential and E_{rev} is the reversal potential for the ionic current. The voltage-dependent gates are described by the following equation:

$$\frac{\partial m}{\partial t} = \frac{m_\infty - m}{\tau_m} \tag{2.4}$$

idem for h

where m_∞ is the steady state activation and τ_m is the time constant for activation.

Calcium-dependent gates were modeled using the Hodgkin-Huxley formalism as well, except that they were dependent on calcium concentration instead of membrane potential. This method was also used by Traub *et al.* (1991) to model a calcium-dependent potassium current in their simulation of a hippocampal pyramidal cell.

Because the extremely steep Ca^{2+} concentration gradient across the cell membrane makes the Ca^{2+} current nonohmic, better performance was obtained using the Goldman-Hodgkin-Katz (GHK) equation (Goldman 1943, Hodgkin and Katz 1949):

$$I_{Ca^{2+}} = Pz^2 \frac{EF^2}{RT} \frac{[Ca^{2+}]_i - [Ca^{2+}]_o \exp(-zFE/RT)}{1.0 - \exp(-zFE/RT)} \tag{2.5}$$

where P is permeability (distance/time) and is modeled in the same way that conductance was modeled for the voltage-dependent currents; z has a value of 2 (the valance of Ca^{2+}); E is membrane potential; F is Faraday's constant; R is the gas constant; and T is temperature. The external concentration of Ca^{2+} ($[Ca^{2+}]_o$) is set to 2 mM. In order to account for the change in membrane resistance that will accompany the opening of Ca^{2+} channels, we calculate Ca^{2+} conductance by finding the chord conductance (Jack et al. 1988):

$$g = \frac{I_{Ca^{2+}}}{E - E_{Ca^{2+}}} \tag{2.6}$$

where $E_{Ca^{2+}}$ is calculated using a variation of the Goldman-Hodgkin-Katz voltage equation that takes into account both monovalent and divalent ions (Jan and Jan 1976):

$$E_{Ca^{2+}} = \frac{RT}{F} \ln\left(\frac{-b + \sqrt{b^2 - 4ac}}{2a}\right) \tag{2.7}$$

where

$$a = 4[Ca^{2+}]_i + P_{K^+/Ca^{2+}}[K^+]_i + P_{Na^+/Ca^{2+}}[Na^+]_i \tag{2.8}$$

$$b = P_{K^+/Ca^{2+}}([K^+]_i - [K^+]_o) + P_{Na^+/Ca^{2+}}([Na^+]_i - [Na^+]_o) \tag{2.9}$$

$$c = -4[Ca^{2+}]_o - P_{Na+/Ca2+}[Na^+]_o - P_{K+/Ca2+}[K^+]_o \tag{2.10}$$

and $P_{X/Ca2+}$ represents the permeability ratio of ion X to Ca^{2+}. Because Ca^{2+} channels are impermeable to Mg^{2+} and Cl^- ions, they are not included in the above equations. $P_{K/Ca2+}$ and $P_{Na/Ca2+}$ represent permeability ratios for the L-type Ca^{2+} channel and have values of 3.33×10^{-4} and 8.547×10^{-4} respectively (Hille 1992). When the model is in its resting state, it has a calcium reversal potential of 67.4 mV which is consistent with the values of 40-70 mV seen experimentally (Hille 1992). Changes in calcium channel permeability are modeled using the Hodgkin-Huxley formalism with the permeability taking the place of conductance.

Calcium dynamics There is little experimental data on the calcium dynamics in piriform pyramidal neurons; nonetheless, because we incorporated a calcium-dependent current into our model, it was necessary for us to construct an ad-hoc model that would at least operate within a plausible range. In order to do this, we borrowed from several previously existing models of calcium dynamics. To model calcium diffusion within the soma, we used a 40 shell model which was identical to that used by Sala and Hernandez-Cruz (1990). To convert current through the calcium channels into calcium concentration in the outermost shell, we used the following equation:

$$\frac{d[Ca^{2+}]}{dt} = BI_{Ca2+} - \frac{[Ca^{2+}]}{\tau} \tag{2.11}$$

where B is a scaling factor with value 22.4×10^5 mM/nA and τ is the decay time constant with value 5 $msec$. This model generated realistic calcium concentrations with values ranging from the baseline 50 nM to the micromolar range. Values for B and τ were obtained by searching for values which allowed us to realistically model the AHP current without generating unrealistic values for calcium concentration.

Parameters for the kinetics of ionic currents Parameters for current kinetics were modeled to specifically fit voltage-clamp data from piriform pyramidal cells when available (CaF, CaS, KA, KM, KAHP). For some channels (NaF, NaP, Kdr), however,

there are no published records of voltage clamp data. In these cases voltage clamp data was used from the closely related hippocampal pyramidal neurons. The sources for kinetic parameters are discussed below. The parameters used to model different voltage-gated conductances are shown in table 2.1.

Fast and persistent sodium currents Parameters for the fast sodium current were obtained from a model study by Traub et al. (1991) of a CA3 hippocampal pyramidal cell. Slight modifications were made to these parameters in order to shift the midpoint of the activation curve to higher membrane potentials. This was done in order to increase the threshold of sodium spiking in the model so that it would better represent the piriform pyramidal cell (Tseng and Haberly 1989a).

In order to replicate physiological results accurately, it was necessary to include a persistent sodium conductance in this model, even though there is, as yet, no direct experimental evidence for this conductance. This is the only conductance we have included in the model with no direct experimental evidence. We found that without this current, curves plotting spike count vs. current injection were much steeper than what we found experimentally. This conductance has been shown to exist in hippocampal pyramidal cells (French et al. 1990). In the current model, kinetic equations for the persistent sodium current come from a study by McCormick and Huguenard (1992). Again, the activation curve was shifted to the right in order to adjust model behavior to match the spiking threshold seen experimentally (Tseng and Haberly 1989a).

The delayed rectifier Parameters for the delayed rectifier are identical to those used in Traub et al.'s (1991) model of a hippocampal pyramidal cell (Traub et al. 1991).

Potassium A-current Banks et al. (1996) recently characterized the A-current in piriform pyramidal neurons of the rat. We used the parameters obtained in this study to model the A-current in our simulation.

Table 2.1: Parameters for active currents used in the model. The first column lists the currents using their abbreviated names: NaF (fast sodium), NaP (persistent sodium), Kdr (potassium delayed rectifier), Kfir (potassium fast inward rectifier), KM (potassium M-current), KAHP (slow calcium activated potassium current), CaF (fast calcium), CaS (slow calcium). The column labeled "Power" contains the exponents to which the respective gates are raised. Other columns are self-explanatory.

Channel	E_{rev} (mV)	*gate*	*power*	α	β	x_∞	τ_x (ms)	*Channel Density* (mS/cm^2)
NaF	55	m	2	$\frac{0.32(36.2+V)}{1.0-\exp\left(\frac{36.2+V}{-4.0}\right)}$	$\frac{0.28(9.2+V)}{\exp\left(\frac{9.2+V}{5.0}\right)-1.0}$	$\frac{\alpha}{\alpha+\beta}$	$\frac{1.0}{\alpha+\beta}$	280.1
		h	1	$0.128\exp\left(\frac{32.3+V}{-18.0}\right)$	$\frac{4.0}{1.0+\exp\left(\frac{9.3+V}{-5.0}\right)}$	$\frac{\alpha}{\alpha+\beta}$	$\frac{1.0}{\alpha+\beta}$	
NaP	55	m	1	$\frac{0.091(V+48.0)}{1.0-\exp\left(\frac{V+48.0}{-5.0}\right)}$	$\frac{-0.062(V+48.0)}{1.0-\exp\left(\frac{V+48.0}{5.0}\right)}$	$\frac{1.0}{1.0+\exp\left(\frac{43.0+V}{-5.0}\right)}$	$\frac{1.0}{\alpha+\beta}$	6.5
Kdr	−90	m	1	$\frac{-0.016(39.2+V)}{\exp\left(\frac{39.2+V}{-5.0}\right)-1.0}$	$0.25\exp\left(\frac{54.3+V}{-40.0}\right)$	$\frac{\alpha}{\alpha+\beta}$	$\frac{1.0}{\alpha+\beta}$	27.0
KA	−90	m	3	$0.5\exp\left(\frac{0.5V+19.65}{15.4}\right)$	$0.5\exp\left(\frac{0.5V+19.65}{-15.4}\right)$	$\frac{\alpha}{\alpha+\beta}$	$\frac{1.0}{\alpha+\beta}$	7.0
		h	1	$0.04\exp\left(\frac{0.9V+59.13}{-6.86}\right)$	$0.04\exp\left(\frac{0.1V+6.57}{6.86}\right)$	$\frac{\alpha}{\alpha+\beta}$	$\frac{1.0}{\alpha+\beta}$	
KM	−96	m	1			$\frac{1.0}{1.0+\exp\left(\frac{35.0+V}{-10.0}\right)}$	$\frac{330.0}{11.3\left(\exp\left(\frac{V+35.0}{20.0}\right)+\exp\left(\frac{V+35.0}{-10.0}\right)\right)}+10.89$	11.5
KAHP	−96	m	1	$\min\left(\frac{[Ca^{2+}]}{0.52\mu M}, 0.01\right)$	0.0005	$\frac{\alpha}{\alpha+\beta}$	$\frac{1.0}{\alpha+\beta}$	1.3
CaF	*ghk*	m	2			$\frac{1.0}{1.0+\exp\left(\frac{42.0+V}{-2.0}\right)}$	$\frac{1.0}{\exp\left(\frac{102.0+V}{-26.7}\right)+\exp\left(\frac{26.8+V}{18.2}\right)}+1.0$	See Text
		h	1			$\frac{1.0}{1.0+\exp\left(\frac{84.0+V}{2.0}\right)}$	$\frac{18.0}{\exp\left(\frac{82.0+V}{-2.7}\right)+\exp\left(\frac{28.0+V}{28.0}\right)}+3.0$	
CaS	*ghk*	m	1			$\frac{1.0}{1.0+\exp\left(\frac{32.0+V}{-10.0}\right)}$	$\frac{1.0}{\exp\left(\frac{3.2+V}{-6.7}\right)+\exp\left(\frac{16.8+V}{18.2}\right)}+3.0$	See Text
		h	1			$\frac{1.0}{1.0+\exp\left(\frac{40.0+V}{35.0}\right)}$	$\frac{350.0}{\exp\left(\frac{35.0+V}{12.0}\right)+\exp\left(\frac{25.0+V}{-12.0}\right)}+10.0$	

Non-inactivating muscarinic potassium current Support for the existence of a slow non-inactivating muscarinic potassium current (M-current) in the piriform pyramidal cell comes from both voltage clamp (Constanti and Galvan 1983, Constanti and Sim 1987a) and pharmacological studies (Constanti and Sim 1987b) in the guinea pig. Unfortunately, these studies were not complete enough to fully model the activation and time constant of these channels. However, Constanti and Galvan (1983a) have reported that the olfactory M-current is very similar to that found in bullfrog sympathetic ganglion cells which has been carefully described and modeled (Yamada et al. 1989). The current model uses this description with kinetics that are three times faster than those used by Yamada et al. This was necessary in order for the model to replicate the fast adaptation seen experimentally. It was also necessary because the kinetics which Yamada et al. used were based on experiments done at 22 °C and the recordings described in this chapter were done at 31-34 °C.

Fast inward rectifying potassium current The fast inward rectifier is a well characterized voltage-gated current in the piriform pyramidal cell. However, it only becomes significantly active at membrane potentials more negative than -100 mV (Constanti and Galvan 1983). Because it is unlikely that a neuron will ever reach this level of hyperpolarization under healthy physiological conditions, this current was excluded from our simulations.

Slow and fast calcium currents Evidence for the existence of a voltage-activated Ca^{2+} current comes from voltage clamp studies in the guinea-pig olfactory cortex (Constanti et al. 1985). Unfortunately, this study made no effort to determine the number of channel types that underlie this Ca^{2+} current. In this study, we began our modeling efforts by trying to model the current with a single set of kinetics, but were unable to match experimental data under these conditions. Instead, it was necessary to include two sets of distinct Ca^{2+} channel kinetics: one with low-threshold and fast inactivation (CaF, for Ca^{2+} fast) and the other with higher threshold and much slower inactivation (CaS, for Ca^{2+} slow). The low-threshold rapidly inactivating current

resembles the calcium T-current which is also present in hippocampal pyramidal neurons (Fisher et al. 1990). The second current has slower inactivation and becomes active at more depolarized levels. It is difficult to classify this conductance as a known calcium current because it differs significantly from the N, L, and P-types that have been found in hippocampal pyramidal neurons (Fisher et al. 1990, Mintz et al. 1992). Most likely, this current represents an amalgamation of the non-T type currents found in the piriform pyramidal neuron. CaS appears faster than P and L-type currents and becomes active at lower membrane potentials than N and L-type currents (Regan 1991, Tsien et al. 1988). Nonetheless, combining the CaF and CaS currents allows the model to accurately replicate the calcium current seen under voltage clamp (Constanti et al. 1985). An additional explanation for the lack of agreement between CaS and the calcium currents found in the hippocampus is that the currents analogous to the N, P, and L- types in the piriform cortex may have different kinetics from the ones found in hippocampus. It is known, for example, that N and P-type currents can differ significantly between cell types (Mintz et al. 1992, Tsien et al. 1988).

Calcium-dependent after-hyperpolarizing potassium current The presence of a slow calcium-dependent potassium current is supported by voltage clamp and pharmacological evidence in the guinea-pig (Constanti and Sim 1987a). The kinetics and biophysics of calcium dependent potassium conductances have been shown to be quite complex (Sah 1995). For example, studies of hippocampal neurons have shown that some Ca^{2+}-dependent potassium currents can be significantly activated by Ca^{2+} released from internal stores, rather than channels in the plasma membrane (Uneyama et al. 1993). Because there is very little data available in piriform pyramidal cells concerning the complex dynamics that underlie this current, we have chosen to implement a relatively simple model of calcium dynamics (see equation 2.11 above). Parameters for the current are shown in table 2.1. Other single cell simulations have used identical methods to model calcium dynamics and Ca^{2+}-activated potassium currents (Traub et al. 1991, De Schutter and Bower 1994b).

Location of voltage-gated currents All of the voltage-gated channels described here were located in the somatic compartment of the model. The dendrite was modeled as entirely passive. Recent work has shown that a number of voltage-gated membrane currents are present in the dendrites of hippocampal (Spruston et al. 1995, Magee and Johnston 1995) and neocortical (Stuart and Sakmann 1994) pyramidal neurons. The existence of voltage-gated currents in layer II piriform pyramidal cells is not yet known, but one study has suggested that at least one subtype of N-type calcium channels that is present in hippocampal and neocortical dendrites is absent from the apical dendrites of the piriform pyramidal neurons (Westenbroek et al. 1992). Layer II pyramidal neurons also tend to have relatively short apical dendrites which suggests that EPSPs may not require the same level of amplification to reach the soma that might be required in some neocortical pyramidal neurons. Furthermore, a study by Stuart and Sakmann (1995) shows that amplification of EPSPs in neocortical cells are amplified by axosomatic, not dendritic, sodium currents (Stuart and Sakmann 1995). Recent studies have also suggested that the active properties of the pyramidal cell dendrite may serve a role primarily in the plasticity of synapses (Magee and Johnston 1997, Markram et al. 1997), not in the temporal patterns of firing seen in the soma and axonal initial segment. For all the reasons cited above, we chose not to include active conductances in the dendrites of our model.

Quantifying comparisons between experimental and modeled records Individual channel densities were varied until the model could replicate the active behavior seen in the real cell. Three criteria were used to judge the quality of the fit. The first was a similarity in spike shape and subthreshold depolarizations during the course of a current pulse. The second was in the pattern of spiking activity over the course of a single depolarizing current pulse. The third was how the neuron responded to current injections of varying intensities.

To compare subthreshold behavior in the model and experimental neurons, we compared power spectra of membrane potential over the range of 1-100 Hz and at different average membrane potentials.

2.4 Results

2.4.1 Current voltage relations in pyramidal cells

Physiology In this study we initially recorded from 16 pyramidal neurons using the whole-cell recording technique to obtain the data used to fit the passive properties of our model. The results for one cell are shown in figure 2.3. Part A shows the response to current injection in the presence of normal slice medium and part B shows the response in the presense of TTX and Cs^+. A comparison of A and B shows that the blockade of active conductances greatly increases the input resistance and time constant of these cells. The sag at hyperpolarizing levels in B indicates that not all the active conductances are blocked with TTX and Cs^+; however, the level of hyperpolarization needed to see this sag suggests that it does not interfere with the determination of time constants for these cells in a physiological range.

Figure 2.3C plots the I/V curve for the data presented in parts A and B. In the absence of blockers (n=16), pyramidal neurons had an average input resistance of 98.3 $M\Omega$ (S.E. 16.0). When TTX and Cs^+ were added to the bath, input resistance increased 54 percent on average from its previous value. Significant increases were also seen in the duration of τ_0 and τ_1 after the addition of blockers. This suggests that active conductances contribute substantially to the ostensibly passive properties of a pyramidal neuron in its resting state. A comparison of passive data taken from cells in the presence and absence of blockers is shown in table 2.2.

Model Results and Mechanisms Because the passive properties of the model were tuned on the responses of pyramidal cells to current injection in the presence of TTX and Cs^+, the model replicates these results well except for the slight sags seen in the experimental recordings. The second column of traces in figure 2.3 shows the current-voltage relation for the model cell. As in the experimental I-V curve, the input resistance of the model cell increases substantially (38 percent) in the absence of K^+ and Na^+ currents (meant to simulate the effects of Cs^+ and TTX).

In order to calibrate the model's passive properties, we used the data collected

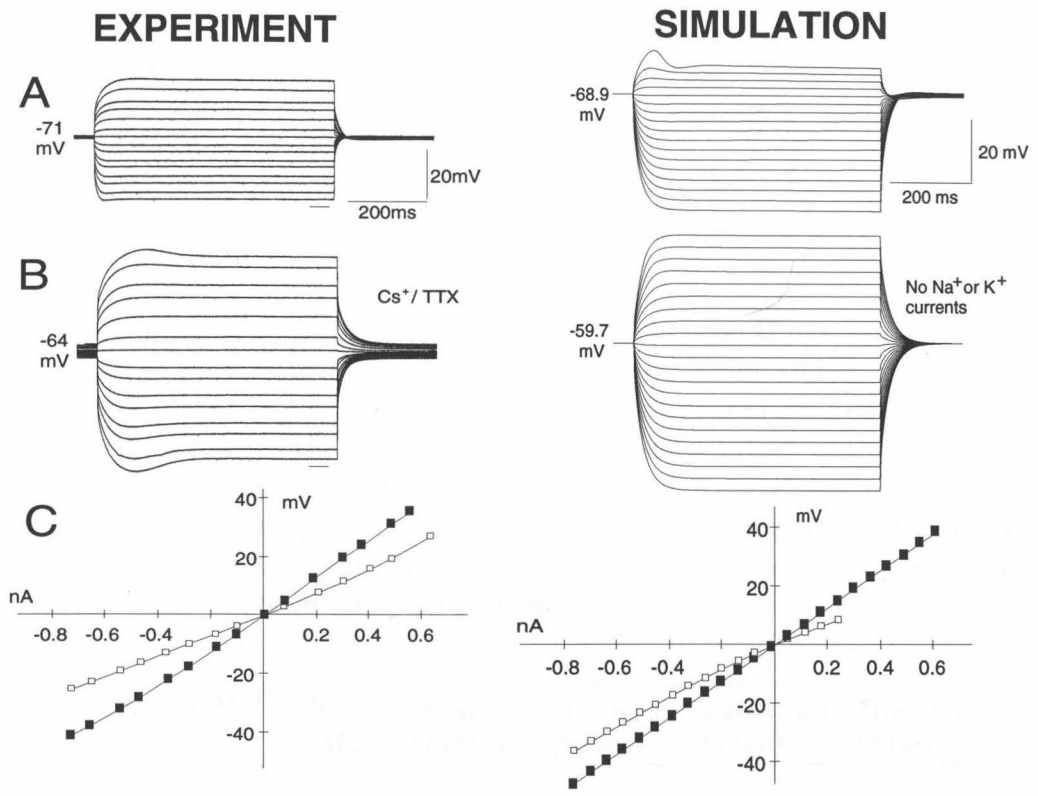

Figure 2.3: Whole-cell recordings of passive properties of layer II pyramidal cell. Experimental traces in A and B show responses to current steps from the same neuron. Top trace (A) shows response in the absence of voltage-gated channel blockers. B shows response in the presence of 5 mM Cs^+ and 1 μM TTX. Current steps of equal magnitude were used to generate both traces. Part C of the experimental recordings shows an I-V curve for the same neuron used in parts A and B. Open squares represent data points collected in the absence of blockers and filled boxes in the presence of Cs^+ and TTX. Membrane potential in C is taken from the portion of graphs A and B indicated by the line segment at the bottom right of these traces. I-V relations in both the presence and absence of blockers appear linear, but the I-V relation for the Cs^+/TTX block shows a much steeper slope, indicating a higher input resistance. The second column of traces shows the responses of the simulated neuron. The results shown in part B of the simulated data traces show simulation results when Na^+ and K^+ currents are removed. This was done to simulate the effects of Cs^+ and TTX. In part C of the simulated data, the blocker-free I-V curve stops short because greater levels current injection induced spiking.

Table 2.2: Experimental data from whole-cell recordings in layer II pyramidal neurons. The first row shows data from cells where blockers were never added. The second and third rows are meant to provide a comparison of cell properties before and after Cs^+ and TTX were added to the bath and so only include a subset of the 16 neurons sampled above. A comparison of the second and third rows shows that voltage-gated currents can appreciably affect the ostensibly passive properties of a neuron. Following the addition of blockers, time constants become twice as long and input resistance increases by approximately 50 percent.

	n	$R.M.P.$ (mV)	R_{in} $(M\Omega)$	$\tau_{0(charge)}$ $(msec)$	$\tau_{1(charge)}$ $(msec)$	$\tau_{0(discharge)}$ $(msec)$	$\tau_{1(discharge)}$ $(msec)$
no blockers	16	-70.3	98.3	10.41	0.87	11.76	1.25
		(0.78)	(16.0)	(0.84)	(0.13)	(0.96)	(0.19)
no blockers	10	-70.5	80.7	11.10	0.81	11.58	1.00
		(3.2)	(14.2)	(1.13)	(0.33)	(1.10)	(0.31)
blockers	10	-62.6	120.8	24.29	1.26	23.18	1.45
		(5.2)	(25.0)	(2.72)	(0.21)	(2.42)	(0.19)

from whole-cell recordings. The overall input resistance of the model cell was 62 $M\Omega$ (closest experimental recording: 60 $M\Omega$). By removing all the voltage-gated conductances from the model and setting R_m to 30 $k\Omega cm^2$ and R_a to 350 Ωcm, the model displayed time constants that fell well within the range seen experimentally with τ_0 and τ_1 taking values of 23.56 $msec$ and 2.10 $msec$ (closest experimental recording: 2.25 $msec$) respectively. Setting the parameters for passive behavior allowed us to explore the electrotonic structure of the neuron as well. Figure 2.2 B shows a dendrogram representing the electrotonic structure of the piriform pyramidal cell. The electrotonic extent of the apical tree is similar to that seen in hippocampal neurons (Major et al., 1994); however, unlike hippocampal (Major et al. 1994) and neocortical (Zador et al. 1995) pyramidal cells, the electrotonic extent of the basal and apical dendrites is approximately equal.

To match F/I data recorded with sharp electrodes, we first had to adjust passive parameters in the soma to simulate the electrical leak caused by the sharp electrode. The parameter R_m in the soma was set to 0.24 $k\Omega cm^2$ achieving an R_{in} of 21.6 $M\Omega$ and a charging time constant of 5.35 $msec$. Experimental data show values of 24 +/- 9 (SD) $M\Omega$ for R_N (Barkai and Hasselmo 1994) and 8.2 +/- .9 (SE) $msec$ (Tseng and Haberly 1989b) for membrane time constant.

2.4.2 The relationship between current injection and spiking frequency

Physiology The first column in figure 2.4 shows the spiking responses of an experimentally recorded pyramidal cell to current injection. As is characteristic of these cells, increased current injection results in an increasing number of spikes with two rapid spikes at the beginning of the pulse followed by spikes at longer intervals which slowly increase with the duration of the stimulation. These data are summarized in figure 2.5A in the form of spike count/current plots where spike numbers are plotted against threshold normalized current injection. Using the S-I method described by Barkai and Hasselmo (1994), we obtain S-I values ranging from 1.1-23.4 (n=5: S-I:1-

10, n=7: S-I:11-20, n=1: S-I >20) which agree with previous studies (Barkai and Hasselmo 1994).

Model A comparison of the model and real neuron's response to current injection is shown in figure 2.4. The results of the model under similar levels of depolarizing current injection are shown in the records of figure 2.5. As in the real data, increased current injection produces an increased spiking output of the modeled cell. Figure 2.5 shows a more quantitative measure of similarity between model and experiment in the form of spike number vs. current injection and F/I plots. The model is able to capture the qualitative features of pyramidal cell behavior, most notably the almost linear relationship between spike number and current injection and the steep fall off in the F/I curves across different levels of current injection.

2.4.3 Detailed timing of action potentials in response to current injection

Physiology In addition to their general increase in spiking frequency, figure 2.4 experimental traces also indicate that layer II pyramidal cells in slice generate characteristic action potential timings in response to current injection. When current injection is just over spiking threshold, a single action potential is produced on the sharp rising edge of the membrane potential. As current injection levels are increased, this spike is followed rapidly by a second action potential with subsequent spikes occurring with increasing delay. It should be noted that even with large current injections, the first two action potentials typically occur in rapid succession. Following these two action potentials, there is rapid adaptation from the initially fast spiking of the first two spikes. This is followed by a much more gradual adaptation during which the interspike interval increases only very slowly. This is most clearly seen in the F/I curves shown in figure 2.5 where frequency falls off very rapidly with time of occurrence in the spike train. This is characteristic of most of the neurons we have recorded from as well as previous reports (Tseng and Haberly 1989b).

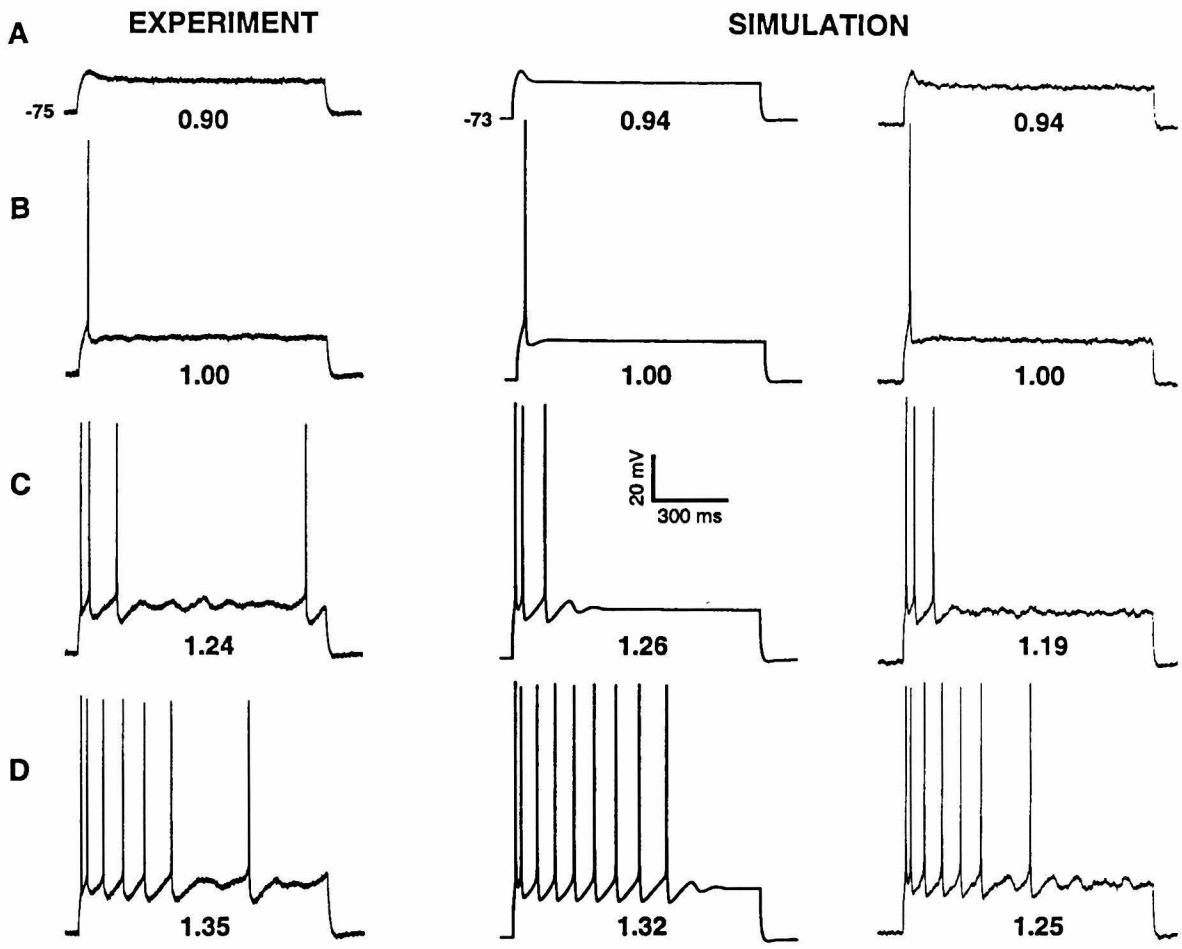

Figure 2.4: Comparison of spike trains from experimental recordings and the model. Experimental and simulated data are shown on the same x- and y- scale. Traces in the left column show an example of an experimental recording. Center column shows response of the model to similar levels of current injection. Rightmost column shows results from the model with the addition of white noise (sampled at 1 kHz with standard deviation: 0.060 nA) to the current injection. Numbers beneath each trace represent the threshold normalized current injection. A. Responses to subthreshold current injection. The fast spikes seen in later traces appear to ride on top of the short latency hump seen here. B. Traces show a single spike in response to threshold level current injection. C. This comparison illustrates the model's ability to replicate the fast spike doublet that occurs at the beginning of many pyramidal neuron spike trains. Subthreshold oscillations seen in the experimental traces following spikes are also seen in the model. D. Again, spiking patterns and subthreshold events in the model and experimental data show great similarities. The simulation results where noise was added to the current injection are especially successful in recreating the persistent subthreshold oscillations that are seen in the experimental traces (C-D). A small hyperpolarization following the end of the depolarizing pulse is also present in the experimental and simulated traces.

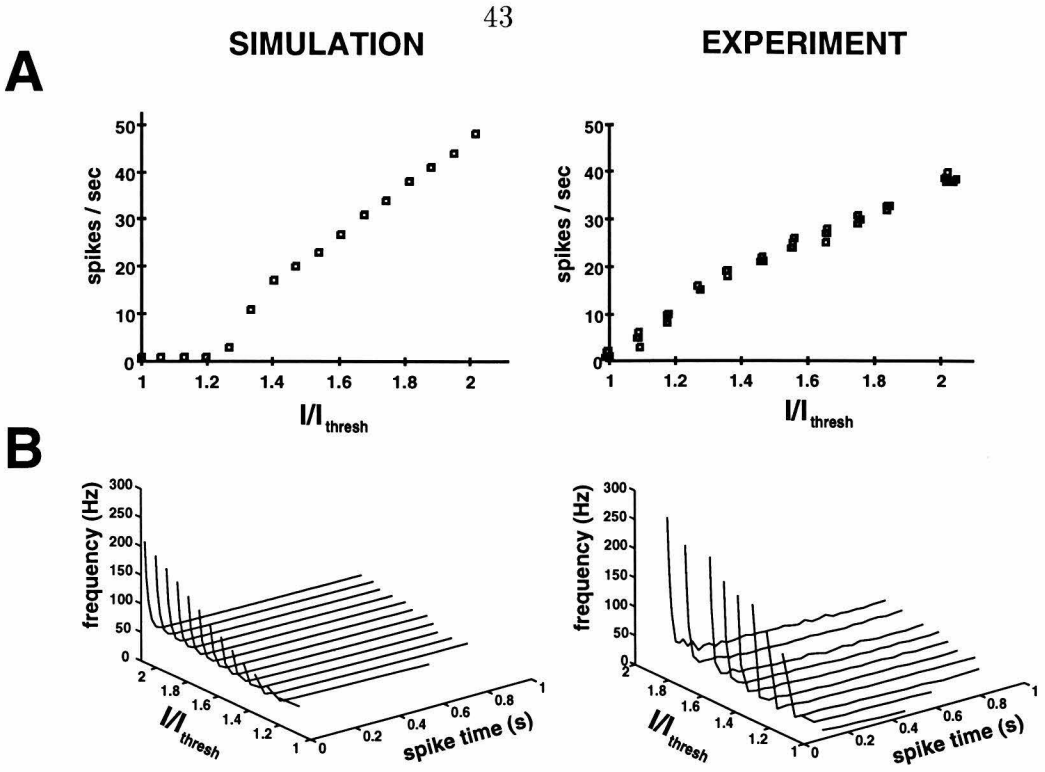

Figure 2.5: Comparison of input/output data from experiment and simulation. A: Spike count during injection of 1 *sec* constant current pulses of different magnitudes. X-axis shows input current over current required to cause the neuron to spike. B: F/I curves show instantaneous frequency plotted against current amplitude and spike time during the depolarizing pulse. Experimental data come from the same neuron. Simulated data come from the same simulation run. For clarity, only a subset of points was used to generate experimental F/I curves.

Model A closer examination of the simulation results in figure 2.4C indicates that the model replicates the timing of spike trains quite accurately, especially immediately after the onset of current injection. The more quantitative measure of similarity between experimental and simulated data shown in figure 2.5 also indicates a close correspondence between the experimental and modeled data.

The most challenging aspect of constructing the model was generating the very fast spikes that came at the beginning of a spike train. In the model, this behavior was due primarily to the presence of NaP and the precise level of A-current. The NaP current activates rapidly and remains active as long as the cell is depolarized. This causes the cell to initially spike rapidly until the KM current is activated. The A-current channel density is critical in controlling the latency of the first spike and

hence the rapid spiking seen at the beginning of piriform pyramidal cell spike trains. Increasing the A-current channel density generally increased the latency of the first spike and the interval between the rapid spikes at the beginning of the train.

The other characteristic pattern of firing of these cells is the spiking adaptation that occurs following the first two spikes. Adaptation appears to be a discontinuous process in the piriform pyramidal cell with the instantaneous frequency of spikes falling at first rapidly from hundreds of Hz to tens of Hz and then slowing down more gradually. In the model, the KM current was primarily responsible for the initial fast adaptation and the KAHP for the slower adaptation typically seen at the end of spike trains. This fits well with experimental data which indicate that the KAHP current is significantly slower than KM in these neurons (Constanti and Sim 1987a). Calcium channels also played a role in this behavior by regulating the activity of KAHP.

2.4.4 Subthreshold oscillations in membrane potential following current injection

Physiology The final characteristic of pyramidal cell response to current injection that we examined is the presence of subthreshold oscillations shown in figure 2.4 C and D. These oscillations are generally seen following the spikes that occur early during the current injection and appear to be in roughly the 10 Hz range. Typically, late occurring action potentials appear to be triggered by the rising edge of these oscillations.

Model A closer examination of the response of the model to current injection demonstrates that the model, on its own, is capable of accurately replicating the hump in membrane voltage following the onset of subthreshold current injection (figure 2.4 III A). However, the model by itself does not replicate the subthreshold voltage oscillations that persist during the current injection at suprathreshold levels. While two cycles of damped oscillations are clearly present following the first 3 spikes in the

simulated spike train in figure 2.4 C, persistent oscillations are absent. However, as we discuss in greater detail later, addition of noise can generate persistent oscillations in the model (third column in figure 2.4).

2.4.5 The effects of individual membrane currents on the behavior of the model

Each of the currents in the model appears to serve a distinct function in the cell. Spike width and height are determined almost entirely by the relative channel densities of the NaF and Kdr currents. The Kdr current is also primarily responsible for the amount of undershoot. The role of other currents is restricted primarily to spike spacing and the structure of subthreshold events.

An effort was made to also model the more subtle aspects of subthreshold events in order to expand the model's explanatory power. A hump on which the early fast spikes ride is evident in both the experimental and model traces (see figure 2.4). In the model this is largely the result of delayed KM activation cutting off depolarization due to NaP. Similarly the damped subthreshold oscillations seen following spikes in figure 2.4 are a result of the interplay between NaP, Kdr, and KM.

Figure 2.6 summarizes the activation of the different membrane currents during the course of a spike train. The graphs for the NaF and CaF currents show only significant conductance changes during action potentials, suggesting that these currents do not play a role in subthreshold events. In contrast, conductances for NaP, CaS, Kdr, and KM do change during the course of the subthreshold oscillations and the voltage ramps that precede spiking. These conductances also show changes during spiking. The KM current differs from the other currents that are active during spiking because it entirely misses the first spike. It is this behavior that underlies the short interspike interval between the first two spikes in the train. When the neuron is no longer spiking the KM conductance slowly decreases. The KAHP conductance is the longest lasting and slowest of all the currents. Its response to spiking is seen only as small ripples riding on top of a much more slowly acting conductance. Even after the current step

is over, the conductance stays active for hundreds of milliseconds.

The same currents (NaP, KM, Kdr) that are responsible for the damped subthreshold oscillations seen in the model in the absence of noise also underlie the persistent oscillations seen in the presence of noise (see below).

2.4.6 Robustness of model to changes in channel densities

In order to test the robustness of the model, we systematically varied each of the channel densities for each current by 20 percent above and below the values used in the simulations discussed in this chapter. The resulting spike count vs. normalized current injection traces are plotted with the normal model response in figure 2.7. As the figure illustrates, the model is very robust to 20 percent fluctuations in channel density. The sole exception is the persistent sodium current where a 20 percent decrease in channel density generates a response curve that is much steeper than what is normally seen. Although the graph in figure 2.7 measures model response only by plotting spike count vs. normalized current injection, we also found that the form of the model's response to individual current injections following 20 percent variations in channel densities did not change significantly from the control condition. For the sake of brevity, this data is not shown here.

2.4.7 Generating subthreshold membrane oscillations with noise

Model The third column in figure 2.4 shows how the addition of noise sampled at 1 kHz with SD 0.075 nA improves the match of modeled data to experimental recordings by introducing persisting subthreshold oscillations. White noise sampled at 1 kHz was added to the current injection values with standard deviations of 0.025, 0.075, 0.100, and 0.200 nA. The results of the simulations are shown in figure 2.8. As can be clearly seen, the presence of noise appears to give rise to the persistent low frequency oscillations seen in the experimental traces.

The presence of persistent oscillations appears to be dependent on the level of

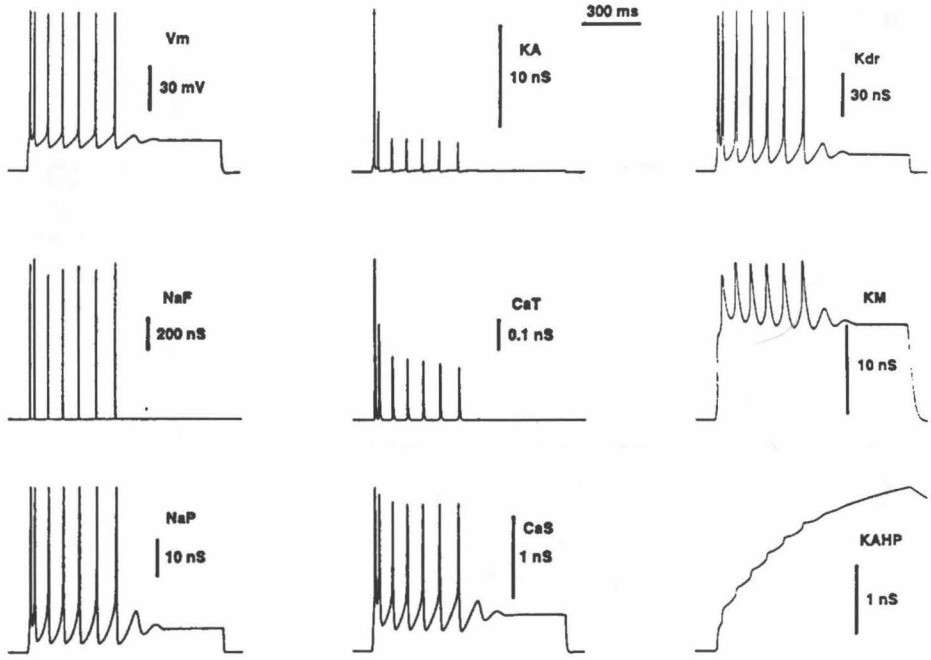

Figure 2.6: Active conductances underlying behavior seen in spike trains. A plot of membrane potential during the course of a spike train is shown in the trace labeled V_m. Conductance traces illustrate the role of different voltage-gated conductances in different aspects of pyramidal cell behavior. The trace labeled NaF represents conductance changes associated with the fast sodium current. NaF appears to only contribute significantly to the formation of spikes, remaining inactive when the neuron is not spiking. The trace labeled NaP represents the activity of the persistent sodium conductance. It is active during spiking, but also at subthreshold potentials. It appears to form a hump beneath the first two fast spikes and is present during the subthreshold oscillations that follow the spike train. It is also active between spikes. The two calcium currents modeled CaS (slow calcium) and CaF (fast calcium) are both active during spiking, although CaS is also active at subthreshold potentials. Potassium currents are labeled Kdr (delayed rectifier), KM (M-current), and KAHP (after hyperpolarizing current). Kdr appears to be active during spiking and subthreshold events. KM shows a significant amount of activity during spiking but is longer lasting in response to spikes than Kdr. It also shows a significant level of steady state activity in response to the depolarizing pulse and is active during the subthreshold events seen in the voltage trace (V_m). In contrast, the A current is active during spiking, but mostly absent during subthreshold activity. KAHP is the slowest of all the currents and shows a monotonic increase in response to the spike train, decaying only slightly following the end of the current pulse.

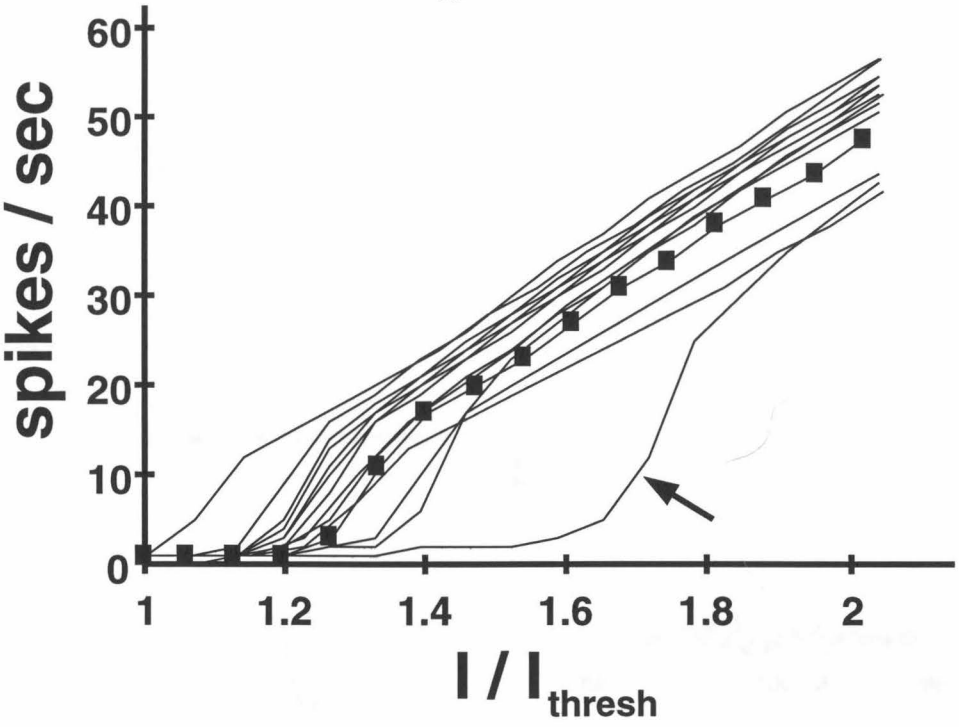

Figure 2.7: Robustness of model to 20 percent changes in individual channel densities. Curves represent simulation results where a particular channel density was increased or decreased by 20 percent. Points represented by filled squares constitute the normal response curve. These results indicate that the model is considerably robust to changes in individual channel densities. The sole exception is the NaP current. A 20 percent decrease in NaP channel density generates a response curve that is much steeper than what is normally seen in experiments and the model. This curve is indicated by the left pointing arrow in the figure.

depolarization and the magnitude of noise. Figure 2.8 A shows no oscillations in the model's response when noise with 0.075 nA SD is injected at resting potential. Yet this is the same level of noise used in part C where persistent subthreshold oscillations are most obvious. This suggests that these oscillations should only be seen at depolarized levels. The amount of noise also appears to be critical as can be seen from a comparison of parts B-D where mean current injection is kept constant and only the amount of noise is varied. In part B, where the noise has a value of 0.025 nA SD, the model's response shows no persistent subthreshold oscillations as is the case in simulation runs where no noise has been added to the current injection. At 0.075 nA SD noise, the persistent oscillations seen in the experimental traces of

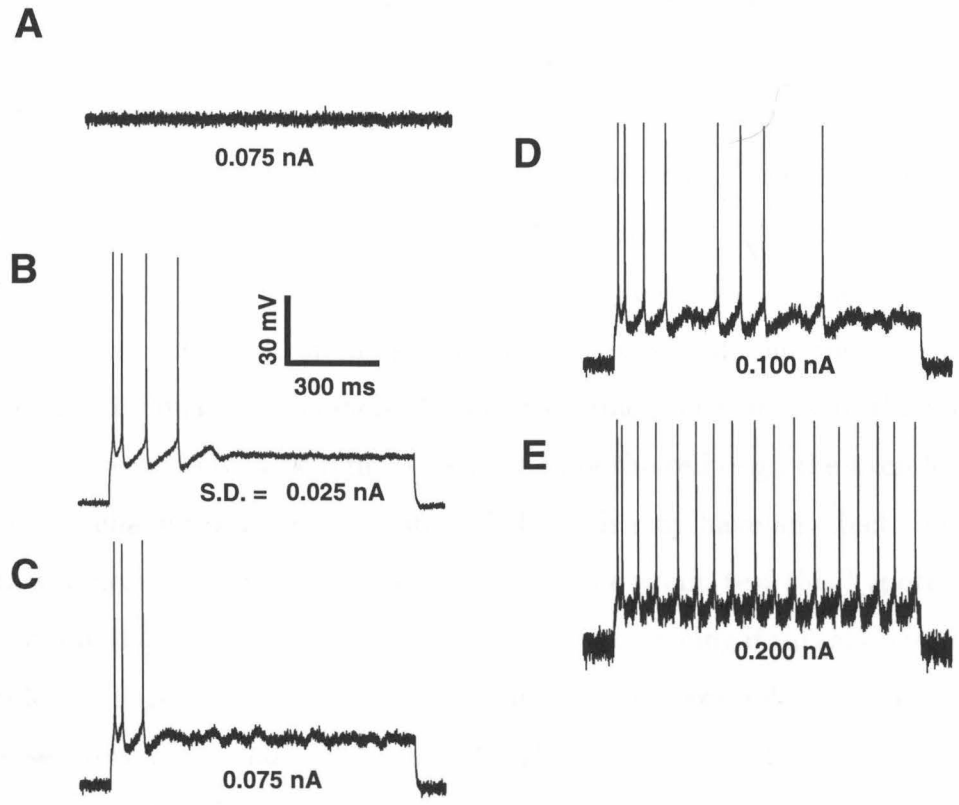

Figure 2.8: Traces generated by simulations where noise has been added to the current injected into the model. Numbers beneath each trace indicate the standard deviation of the noise in nA. All noise injections have a mean of 0 nA. The addition of noise produces traces that can better replicate the subthreshold events seen in experimental recordings. Trace A shows model response to 0.75 nA SD current injection at resting potential. Although this is the same noise level used to generate results shown in C, no subthreshold oscillations are seen.

figure 2.4 C are clearly replicated in the simulation results. At 0.10 nA SD noise, the spike failures seen in figure 2.4 D are also seen in the model; however, at much higher noise levels (0.20 nA SD), the model appears to fire regularly and subthreshold oscillations are no longer seen.

Testing effects of noise physiologically As just described in our model, the addition of broadband noise gives rise to the persistent subthreshold oscillations seen experimentally. Although no noise had to be added to the experimental preparation to elicit subthreshold oscillations, biological neurons have intrinsic noise generating mechanisms which are absent in most single cell simulations. While simulations of neurons are based on the deterministic Hodgkin-Huxley equations, the active currents in real neurons are the result of the stochastic processes that underlie the opening and closing of individual ion channels. It is conceivable that if many of the voltage-gated channels are densely packed in a small region of the cell (e.g., the axon hillock), the stochastic behavior of a small number of channels may have an effect similar to the injection of noisy current in the model. Ideally one would test this hypothesis by simply removing the noise from the biological neuron and seeing if this also eliminated subthreshold oscillations. However, such an approach (for example, cooling the cell) would also severely affect channel kinetics (Hodgkin and Huxley 1952). Therefore, we decided to explore the role of noise in the experimental preparation by looking to see whether or not subthreshold oscillations could be enhanced by adding noise to the constant current pulses used to stimulate pyramidal cells in slice. Furthermore, we felt that a broadband noise stimulus would be ideal for characterizing the neuron's subthreshold frequency response which could then be compared to our model's.

Results were obtained from 23 cells in 10 eight-week-old rats. Part A of figure 2.9 shows an example of the subthreshold response of a neuron injected with noise (SD = 0.05 nA). Part B shows the neuron's response to injected noise (SD = 0.10 nA) over a broad range of membrane potentials (-75 to -60 mV) and for frequencies up to 100 Hz. Two things are immediately obvious about the graph in part B. First, most of the power seems to be concentrated in the 1-20 Hz range and the second is that

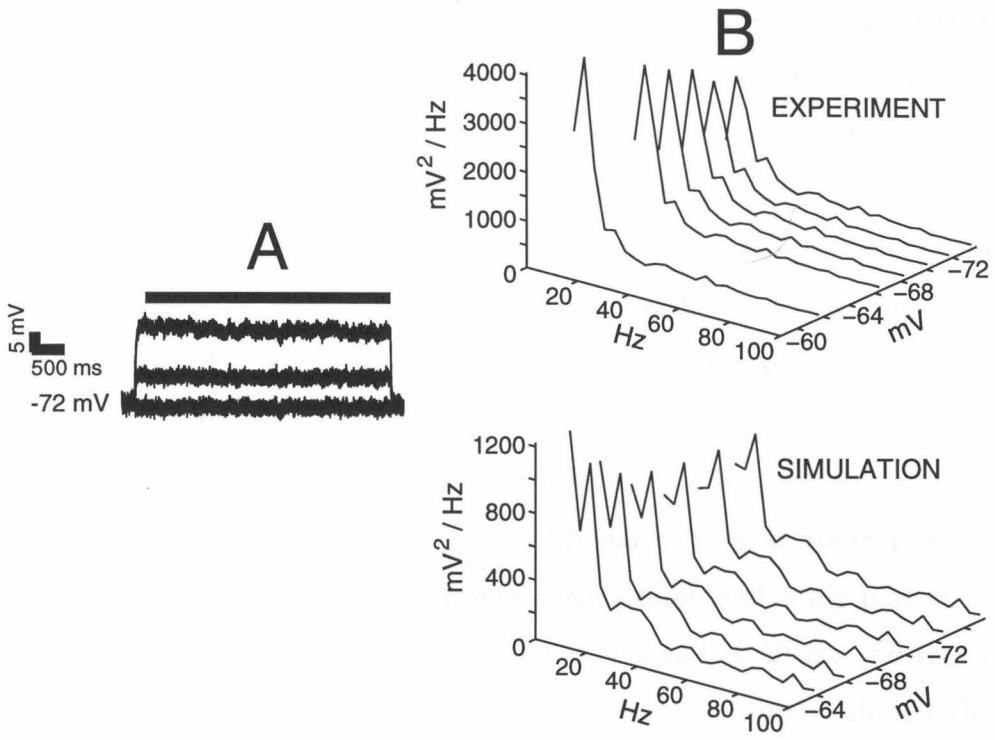

Figure 2.9: Part A shows sample subthreshold responses of a real neuron to injection of broadband noise (SD = 0.1 nA). Power spectra used in data analysis were taken over the time indicated by the thick line at the top of the traces. This was done to avoid the possible artifact resulting from the neuron's charging time. The top trace part B shows a real neuron's subthreshold frequency response plotted as power vs. frequency vs. mean membrane potential. Most of the power is contained within a frequency range of 0-30 Hz. Interestingly, low frequency components tend to increase in power as membrane potential becomes more depolarized. The lower trace in part B shows results from the model when the same stimulus used for experimental recordings was applied to the model. Qualitatively, the simulation's subthreshold response appears to be similar to that of the real neurons with most power being concentrated in the 0-30 Hz range and an increase in the power of lower frequency components occurring as the membrane potential becomes more depolarized.

there appears to be an increase in power as the cell is increasingly depolarized. The first point suggests that the neuron's subthreshold response to stimulus is essentially blind to events that occur at frequencies above 20 Hz, while the second point suggests that the neuron's frequency response is voltage-dependent; specifically, greater levels of depolarization amplify frequency components in the 4-12 Hz range. This effect is shown in figure 2.10 where the neuron's response to noisy current injections at different levels of depolarization is compared. As the figure shows, a depolarization that is just under threshold tends to amplify membrane potential fluctuations in the 4-12 Hz range. When the neuron is brought to a suprathreshold level but an area of the trace is examined where no spikes have occurred, subthreshold oscillations are amplified to a significantly greater extent.

To characterize the amount of depolarization-dependent amplification of different frequency components, we measured the slope of linear regression fits to power plotted against membrane potential on a log scale. An example of a log plot of power vs. membrane potential for frequency ranges of 4-12 Hz and 30-50 Hz and the corresponding regression lines is shown in part A of figure 2.11. A positive slope indicates increasing amplification of a frequency component, while a negative slope indicates a dampening of oscillations in that frequency range. The steepness of the slope reflects the magnitude of the amplification of subthreshold oscillations as a function of membrane potential. Part A of figure 2.11 shows that frequency components in the 4-12 Hz range are significantly amplified while those in the 30-50 Hz range remain approximately constant over increasing levels of depolarization. This point is reiterated in part B of the figure where the slopes of the linear regression lines are plotted against power over 4 Hz bins for a frequency range of 0-100 Hz. What is immediately obvious is that frequency components in the 0-16 Hz range show significantly higher slopes than higher frequencies. However, only frequency components in the 4-12 Hz range always showed a positive slope out of the 23 neurons we recorded from for this series of experiments. The presence of negative slopes for the 0-4 Hz bin is most likely due to sampling error because this bin would include oscillations that have such low frequencies that they occur only a few times during the course of stimulation and

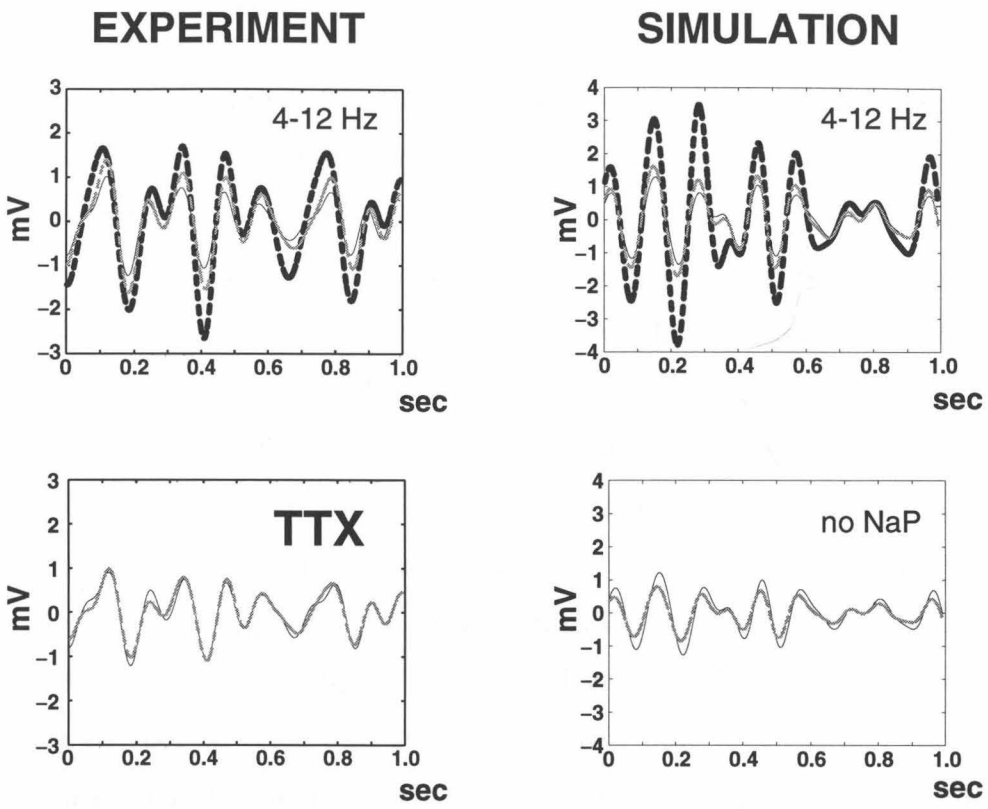

Figure 2.10: Waveforms containing white noise (SD = 0.1 nA) were added to depolarizing constant current pulses. The mean from the resulting changes in membrane potential was subtracted from each trace and the result was then bandpass filtered at 4-12 Hz in order to generate the graphs in this figure. The thin solid line represents the response of a real and simulated neuron at baseline while the thin gray dashed line represents the response of the neuron to a depolarization that is just below threshold levels. The thick black dashed line represents the response of the neuron at suprathreshold levels but in a region of the trace where the neuron is not actually firing. Both experimental and simulated traces show a depolarization dependent amplification of oscillations in the 4-12 Hz that is especially prominent at suprathreshold levels. In the model, this amplification effect is dependent on the presence of the persistent sodium current (NaP). As is shown in the graph in the lower right, elimination of the NaP current results in a dampening of oscillations at the more depolarized level indicated by the gray dashed line. Gray dashed and solid lines are taken at the same mean membrane potentials in both top and bottom traces. To test the possibility that NaP underlies amplification of subthreshold oscillations in the real neuron, we added TTX and found that it eliminated depolarization-dependent amplification of subthreshold oscillations.

hence have variable power from trial to trial. However, this argument would not hold at higher frequencies and in those cases it appears that there is little amplification or dampening in comparison to what is seen in the 0-16 Hz range.

To ensure that the voltage-dependent amplification of subthreshold oscillations was not an artifact of the electronics we were using, we performed the same noise injections we had used for the real pyramidal cell on a simple RC circuit and found that there was no voltage-dependent amplification of 4-12 Hz components of the stimulus. Additionally, because our model had shown that depolarization-dependent amplification of subthreshold oscillations requires the presence of the NaP current, we added 2 μM TTX to the slice bath to explore this possibility in the real neuron. The results of this experiment are shown in figure 2.10. TTX clearly eliminates the amplification of subthreshold oscillations in the 4-12 Hz range. Unfortunately, at the present time there is no specific blocker known to block NaP without also blocking NaF (Adams and Swanson 1996), so the possibility that NaF may play a role in this phenomenon can not be ruled out. Nonetheless, this experiment clearly shows that the amplification effect is dependent on sodium currents. The effects of TTX for multiple cells are shown in figure 2.12. Again, TTX appears to wipe out the effects of amplification. Similarly, we tested the effects of synaptic blockers (30 μM CNQX, 100 μM APV, 50 μM PCTX) and found that these had no effect (see figure 2.12).

Comparison of model to physiology Figures 2.10, 2.11, and 2.12 compare the subthreshold responses of the model to our physiological recordings. In figure 2.10 we find that the levels of amplification of subthreshold responses in the model are comparable to those seen in the physiological case. Similarly, removal of NaP appears to eliminate this amplification much as TTX does for the real neuron. The one difference is that in the model, removal of NaP appears to result in a dampening of the 4-12 Hz oscillations rather than the simple elimination of amplification. When comparing the amplification of different frequency components over a 0-100 Hz range, the model is qualitatively similar in that lower frequency components are in general more greatly amplified than higher frequency components; however, the

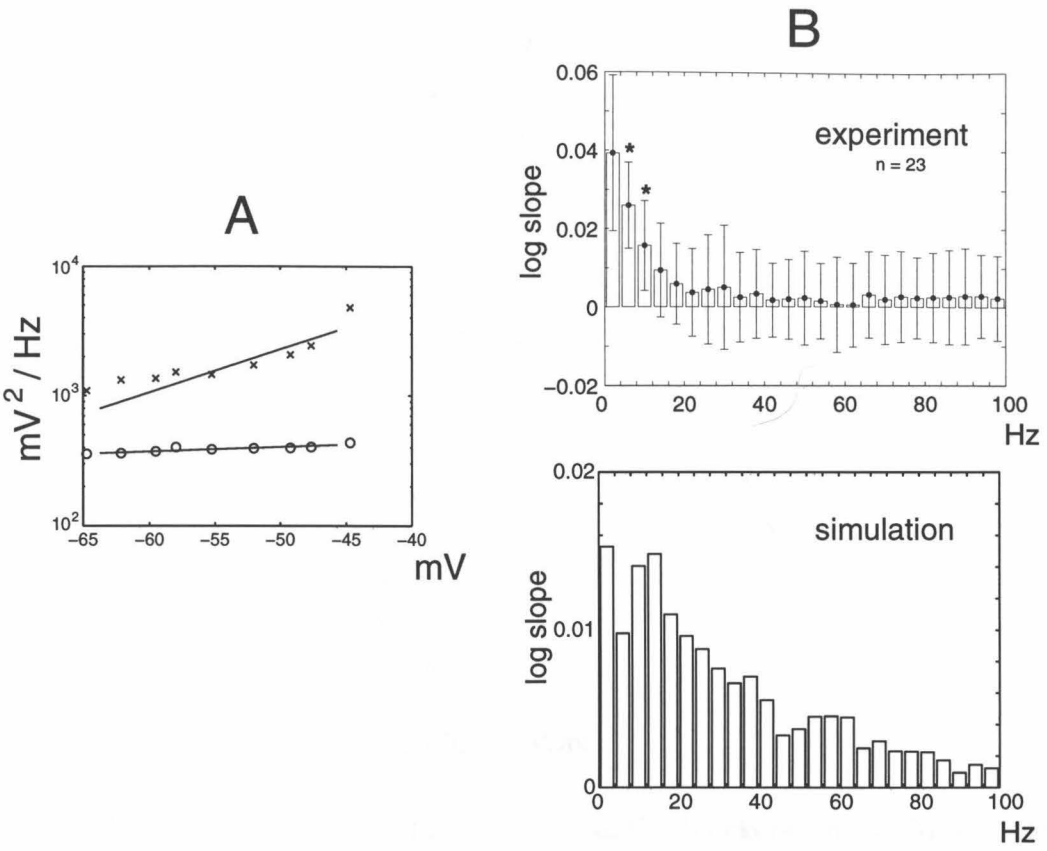

Figure 2.11: Part A shows a logarithmic plot of power in the 4-12 Hz (x's) and 30-50 Hz (o's) range versus mean membrane potential for an experimental recording where a neuron has been injected with broadband noise with a standard deviation of 0.10 nA. This graph shows that low frequency components that fall within the theta range (4-12 Hz) are significantly amplified as mean membrane potential increases, while higher frequency components representing the gamma range (30-50 Hz) are not. This is illustrated by a comparison of the slopes of the linear regression fits to the data shown as solid lines. Although the points plotted for some frequency ranges deviated significantly from linearity, the slope measure is still a useful measure to indicate the presence or absence of voltage-dependent amplifications of different frequency ranges. It is also a more intuitive measure than those that would be used by nonlinear fitting methods. The slopes of linear regression lines for data similarly plotted at frequency increments of 4 Hz are used to generate data for the bar graphs shown in part B. The top graph in part B shows results from 23 experimental recordings where white noise with SD 0.10 nA was added to the current injection. Error bars represent standard deviation. Asterisks indicate that all recordings showed a positive slope over the marked frequency range. Comparison with simulation results in the lower trace in part B show qualitatively similar results with the main difference being that experimental results show a much more selective amplification of components in the 0-12 Hz range.

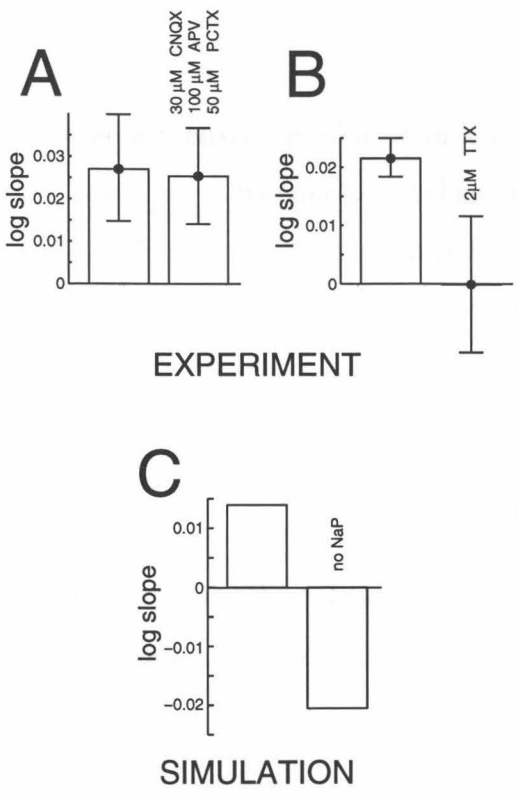

Figure 2.12: Part A shows the effects of synaptic blockers (n = 5) on the depolarization-dependent amplification of 4-12 Hz oscillations when cells are stimulated with broadband noise (SD = 0.1 nA). Synaptic blockers appear to have no significant effect. Part B shows the effects of sodium channel blocker TTX which effectively wipes out all depolarization-dependent amplification (n = 5). Part C shows a similar bar graph for the pyramidal cell simulation which shows a depolarization-dependent dampening of subthreshold oscillations in contrast to the simple elimination of depolarization-dependent amplification seen in part B.

fall off in voltage-dependent amplification levels from low to high frequencies is significantly less steep. Lastly, in figure 2.12, the pharmacological effects of TTX on the depolarization-dependent amplification of 4-12 Hz are compared to the effects of removing the NaP current in the model. Removal of NaP in the model resulted in a significant depolarization-dependent dampening of subthreshold oscillations in the 4-12 Hz range, suggesting that NaP's role in the model and real neuron may differ to some extent.

2.5 Discussion

In this chapter we have presented a realistic simulation of a single layer II pyramidal neuron from piriform cortex based on a morphology taken from a stained neuron. Using passive data from whole-cell recordings, we derived values for R_m, R_a, and C_m. Voltage-activated currents were added based on experimental evidence and were modeled using voltage-clamp data for the piriform pyramidal neuron when possible. The channel densities of these currents were then varied until the model could reproduce spike trains that resembled *in vitro* data. F/I curves were used to further constrain the model to experimental data and to ensure that it had a dynamic range similar to what is seen experimentally. Furthermore, we characterized the subthreshold frequency response in the real cell and found that our model could qualitatively match this behavior as well.

2.5.1 Response of pyramidal cells to current injection

As described in the results, the spiking behavior of the model was tuned by comparison to current injection results for 12 pyramidal cells. While 12 cells are a minimal sample for this purpose, our overall description of the firing properties of these cells closely matches the more extensive study of the same cells published previously by Barkai and Hasselmo (1994). For example, these authors report S-I values which range 1-23, and we find with our smaller sample values that range 1.1-23.4. Accordingly, we are confident that spiking behavior on which the model was tuned was accurate.

Where the present data differ substantially from previous reports is when the values obtained with whole-cell recording techniques in our experiments are compared to previous sharp electrode recordings. Whole cell techniques reveal substantially higher membrane input resistances than sharp electrode studies (Staley et al. 1992). In the case of the piriform cortex pyramidal cell, the previous sharp electrode study by Barkai and Hasselmo (1994) shows an average resting membrane potential (R.M.P.) of -76 mV and an average input resistance (R_{in}) of 24 $M\Omega$. Similarly, a study by Tseng and Haberly (1989b) shows a R.M.P. of -74.3 mV, and an R_{in} of 38.5 $M\Omega$.

In contrast, whole-cell recordings in this study generated values of -69.6 mV for the resting membrane potential and 98.3 $M\Omega$ for R_{in}. However, previous sharp recordings of membrane time constant did not differ significantly from whole-cell results with Tseng and Haberly's (1989b) sharp electrode study reporting an average membrane time constant of 8.2 $msec$, while we found a value of 10.02 $msec$ for the charging portion of the voltage curve and 11.03 $msec$ for the discharge.

Our whole-cell results are additionally interesting because they are taken from adult animals (8 week old rats). The vast majority of whole-cell studies are done in immature animals (1-3 weeks) because these preparations typically give a higher yield of successful recordings. Because we are interested in how the fully developed brain functions, we felt we should only record from neurons taken from adult brain even if our yield would be lower. Interestingly, a comparison with results from a whole-cell study done on piriform pyramidal cells from immature animals (9-18 day old rats) shows a significant difference in the input resistance of layer II cells (Banks et al. 1996). This study showed average input resistances of 178 $M\Omega$ for layer II pyramidal cells, while our results give us a value of 98.3 $M\Omega$ (a 45% smaller value). Unfortunately, we know of no whole-cell studies other than our own which look at the transient properties of piriform pyramidal cells (i.e., that derive values for τ_0 and τ_1) and so we can not compare these results to those from younger animals. Comparisons of input resistances in the hippocampal cells of young and adult animals show a similar trend where older animals tend to show lower input resistances than younger animals (Zhang and Krnjević 1993, Cherubini et al. 1989).

2.5.2 Functional significance of different voltage-gated conductances

The model described here contains seven voltage-gated currents (excluding Kfir). It is unlikely that we have accounted for all of the currents present in the real piriform pyramidal neuron. Experimental studies of hippocampal pyramidal cells suggest the existence of at least 17 currents in hippocampal neurons (Brown et al. 1990). The

cerebellar Purkinje cell is known to possess at least 10 distinct currents (De Schutter and Bower 1994b). In the absence of more detailed information on the currents present in the layer II pyramidal cell, we erred on the side of the conservative, only adding conductances if the match to physiology absolutely required it. In the next sections we will consider the appropriateness of the choices we have made for the presence and parameterization of individual conductances.

In the present model, the KM current was primarily responsible for the initial fast spike train adaptation and the KAHP current for the slower adaptation typically seen at the end of spike trains. There is voltage clamp data that indicates that the KAHP current is significantly slower than KM in these particular neurons (Constanti and Sim 1987a) which does not contradict our assertion; however, we know of no experimental studies that have tested the validity of our model directly. In principle, the predicted roles for the KM and KAHP conductances in these neurons could be tested pharmacologically. For example, carbachol is known to have an effect on KM and KAHP currents (Constanti and Sim 1987a) and has been shown to greatly reduce adaptation while slowing the decay of F/I curves in these neurons (Barkai and Hasselmo 1994, Hasselmo and Bower 1992). However, these previous studies used relatively high concentrations of carbachol (20 mM) which is know to reduce the activity of both KM and KAHP (Constanti and Sim 1987a). We would predict that lower carbachol concentrations in the range of 1-2 mM, which would selectively suppress the KAHP current, should affect adaptation later in a spike train elicited by a constant current pulse. This effect could then be compared to the more dramatic change in adaptation caused by higher concentrations of carbachol.

We found that the addition of a persistent sodium current (NaP) to our model greatly improved its performance. Specifically, we found that this current produced better S-I results and was also involved in the subthreshold oscillations following a train of action potentials. Furthermore, this current appeared to play a role in the fast spikes that are often seen at the beginning of a spike train. Although we know of no channel blockers that are specific to the NaP current, we predict that the addition of Ca^{2+} channel blockers should have no effect on subthreshold oscillations.

Interestingly, a study by Llinás and colleagues (1991) has shown that subthreshold oscillations in neocortical neurons are also dependent on a NaP-type current.

2.5.3 Subthreshold oscillations induced by noise

One interesting result from our simulation work is that broadband noise in the current injection can elicit the persistent subthreshold oscillations that we saw in our experimental data. At first glance the addition of current noise may seem like an implausible physiological explanation for the presence of subthreshold oscillations. However, one must consider the differences between a detailed single cell simulation and a real neuron. Almost all single cell simulations use the deterministic Hodgkin-Huxley equations to model voltage-gated conductances. Yet, in real neurons voltage-gated conductances are generated by discrete channels that operate on stochastic principles (Hille 1992). This suggests that noise might be intrinsic to real neurons.

Furthermore, studies of the distribution of Na^+ channels in neurons have indicated that high densities of Na^+ channels exist at the axon hillock (Angelides et al. 1988) where they are kept from diffusing into the soma (Kobayashi et al. 1992). A high concentration of channels in an electrotonically compact area such as the axon hillock may allow events at the single channel level to have macroscopic consequences. One simulation study has already suggested that stochastic channel-based simulations can display macroscopic behavior that diverges from the standard Hodgkin-Huxley model (Strassberg and DeFelice 1993). Unfortunately, this study did not address the issue of subthreshold oscillations. Ideally one would want to test the noise-induction of subthreshold oscillations experimentally. However, reducing channel noise (for example by cooling) would affect the kinetics of the channels (Hodgkin and Huxley 1952) which would make the interpretation of any results considerably more difficult.

Perhaps the most interesting aspect of the noise induced subthreshold oscillations is their functional implications. We showed experimentally that the addition of noise to a constant current pulse selectively amplifies oscillations in the membrane potential in the 4-12 Hz range. This frequency range is biologically relevant because it approx-

imates the sniffing rate (Macrides et al. 1982) and the EEG oscillations observed in piriform cortex (Woolley and Timiras 1965). Under more physiological conditions, synaptic background activity may act to induce subthreshold oscillations which may then lock to the sniffing rate or incoming activity from the olfactory bulb. Network modeling work done previously in our lab utilized a pyramidal cell model that showed no intrinsic subthreshold oscillations, yet showed that the network as a whole acted like an oscillator in the gamma (30-80 Hz) and theta (4-12 Hz) frequency ranges (Wilson and Bower 1992). Perhaps intrinsic oscillations in networks and single cells can interact constructively to amplify neural signals or reduce noise in the system. These questions are likely to be answered when single cell neurons with realistic subthreshold membrane properties are introduced into network models.

3

Pyramidal Cell Response to Physiologically Plausible Patterns of Synaptic Input

3.1 Abstract

Fast oscillations (30-50 Hz) modulated in bursts by the sniffing rate (4-12 Hz) are observed in response to odor stimuli in the piriform cortex of animals (Freeman 1960, Woolley and Timiras 1965). Recent current source density (CSD) studies (Ketchum and Haberly 1993a, Ketchum and Haberly 1993b, Ketchum and Haberly 1993c) have revealed the spatio-temporal patterns of synaptic activity that might underlie fast oscillations. In this study we use these patterns (gamma inputs) of input to study the response of a simulated pyramidal cell from piriform cortex and determine the possible computational utility of such a fixed pattern. Our findings show the following: 1. This spatio-temporal pattern of synaptic input can generate patterns of spike timing that indicate the origin of the synaptic input. 2. The fast $GABA_A$ inhibition that is part of this input pattern is able to increase the temporal requirements of suprathreshold excitation but does not act to bin spikes. 3. The physiological effects of a single gamma input last up to 4 times as long as a single gamma oscillation. 4. A gap on the order of 650 $msec$ is required to space out bursts of gamma inputs such that one burst does not affect the pyramidal cell's reponse to the second.

3.2 Introduction

Experimental work in a variety of systems has demonstrated the reliability of spike timing in response to multiple trials of identical stimuli. In the behaving monkey, spikes from individual units have been shown to line up in repeated trials with temporal jitter on the order of only a few miliseconds (Bair and Koch 1996). Additional studies (Bialek et al. 1991, Theunissen et al. 1996) in insects using information theoretic approaches have established that the precise timing of individual spikes carries a significant amount of information about the stimulus. One may deduce from these data that the temporal structure of synaptic inputs to single neurons must be tightly controlled in order to reliably reproduce spike timings in repeated trials.

Unfortunately, technical limitations stand in the way of determining the temporal structure of synaptic input to individual neurons in awake-behaving, or even anesthetized animals. Nonetheless, if the brain structure is laminar and a single neuronal population predominates, it is possible to apply current source density (CSD) analysis (see Mitzdorf, 1985, for review) to elucidate the spatio-temporal pattern of synaptic inputs to a population of neurons. This is done by calculating current sources and sinks at incremental depths and then correlating the sources and sinks to synaptic activity. Since synaptic inputs in many cortical areas are segregated along the dendritic tree of pyramidal neurons according to origin and type, one may further deduce which pathways are responsible for generating individual sources and sinks. The CSD approach is thus ideal for cortical areas where synaptic pathways are well known and areas have a precise laminar organization.

CSD studies in the piriform cortex of the rat and opossum have revealed a stereotyped spatio-temporal pattern of synaptic input to pyramidal neurons in response to a strong shock to the lateral olfactory tract (LOT) which carries afferent input from the olfactory bulb (Rodriguez and Haberly 1989, Ketchum and Haberly 1993a). Interestingly, the pattern of synaptic activity revealed in both of these studies is almost identical despite the approximately 100 million years that separate these species in evolutionary development (Ketchum and Haberly 1993a). This remarkable level of

conservation in synaptic behavior suggests that the particular spatio-temporal pattern of synaptic input revealed by the CSD analysis may be vital in the proper functioning of the olfactory systems of each of these species. When a weak shock is administered to the LOT, the field potential pattern elicited is highly reminiscent of the gamma oscillations seen in awake-behaving rats (Ketchum and Haberly 1993c). This result provides additional evidence that such patterns of synaptic activity may underlie neural behavior in the awake-behaving animal. CSD analysis based on these field potential oscillations reveals a repetition of the pattern seen in the strong shock case. Ketchum and Haberly (1993b) constructed a systems model in order to replicate the strong shock CSD results. Using this model and physiological and anatomical data about the piriform cortex, they were able to estimate the spike arrival time distributions for different synaptic pathways terminating on the apical branches of pyramidal neurons.

Previous work in our laboratory (Wilson and Bower 1991, Wilson and Bower 1992, De Schutter and Bower 1994b, De Schutter and Bower 1994a) has suggested that the biological details of single cells and networks are of paramount importance in determining the computational properties of these structures. We therefore used Ketchum and Haberly's arrival time distributions to stimulate our realistic model of a piriform pyramidal cell (chapter 2) in order to determine what the computational consequences of this stereotyped pattern of synaptic activity might be. By using only a single iteration of the CSD-inspired pattern of synaptic input we were able to model the cell's response to the synaptic input underlying a single gamma oscillation. EEG recordings from awake-behaving rats had indicated that a burst of theta modulated gamma oscillations consisted of an average of 7.2 gamma cycles (Woolley and Timiras 1965); therefore, we simulated burst activity by repeating the synaptic input pattern eight times.

Although previous studies have examined the effects of synchronous vs. asynchronous synaptic inputs (Agmon-Snir and Segev 1993, Murthy and Fetz 1994, Bernander et al. 1994) and random background synaptic activity (Bernander et al. 1991, Rapp et al. 1992), we know of no studies where physiologically plausible and exper-

imentally determined patterns of synaptic input have been used to study single cell behavior. The results presented here suggest that a biologically realistic pattern of synaptic input allows for greater complexity in the behavior of a neuron than these previous studies would suggest.

3.3 Methods

All modeling work was done using version 1.4 of the GENESIS neural simulator (Bower and Beeman 1995). The cell morphology, distribution and parameterization of voltage-gated conductances, and passive properties of the model cell were all identical to those described in chapter 2. The only difference was the addition of synaptic channels that is described here. Dr. Lewis Haberly of the University of Wisconsin, Madison, assisted us with determining the boundaries of anatomical layers in the model cell by observing the stained neuron from which the cell morphology was taken. In this study, we further expand the model by adding synaptic channels to the dendritic tree and controlling the timing of synaptic inputs.

Synaptic conductances Spikes arriving at synapses were represented by unit impulses. All synaptic conductances (except those mediated by $NMDA$ receptors) were modeled using the following impulse response:

$$G(t) = \bar{g}\frac{\tau_1\tau_2}{\tau_1 - \tau_2}\left(e^{-t/\tau_1} - e^{-t/\tau_2}\right) \tag{3.1}$$

with time to peak given by

$$t_{peak} = \frac{\tau_1\tau_2}{\tau_1 - \tau_2}\ln\left(\frac{\tau_1}{\tau_2}\right) \tag{3.2}$$

where $G(t)$ is conductance, $\bar{g}$ is maximal conductance, t is time, and τ_1 and τ_2 are time constants. Parameters for all synaptic conductances are shown in the table 3.1. The location and properties of individual receptor types are described below.

Table 3.1: Synaptic conductance parameters. *NMDA* conductance is implemented using the Holmes and Levy (1991) model.

Type	Location	$\tau_1(ms)$	$\tau_2(ms)$	$t_{peak}(ms)$	$E_{rev}(mV)$	*density* (mS/cm^2)
non-NMDA	*Ia*	1.50	3.00	2.08	0.0	11.62
NMDA	*Ia*			See Caption		0.05
non-NMDA	*superficial Ib*			idem		2.4
NMDA	*superficial Ib*			idem		0.3
non-NMDA	*deep Ib*			idem		2.4
NMDA	*deep Ib*			idem		0.3
$GABA_A$	*II*	1.00	5.50	2.08	−60.0	4.0
$GABA_B$	*Ia*	150.00	180.00	164.09	−90.0	0.4

3.3.1 Synaptic structure of the model

Layer Ia The lateral olfactory tract (LOT) carries axons from mitral and tufted cells in the olfactory bulb to the piriform cortex. Anatomical and physiological evidence show that afferent axons arriving via the LOT make excitatory connections exclusively onto the portion of pyramidal cell apical dendrites found in layer Ia (Heimer 1968, Rodriguez and Haberly 1989, Ketchum and Haberly 1993a, Price 1973, Haberly and Behan 1983). Pharmacological experiments performed in rat piriform cortex slices show that LOT induced excitation of pyramidal neurons is mediated by both *NMDA* and *non-NMDA* receptors in layer Ia (Jung et al. 1990, Kanter and Haberly 1990). A slow acting $GABA_B$ K^+-mediated inhibition is also present in layer I (Tseng and Haberly 1988). This inhibition is believed to originate in feedforward inhibitory neurons which are excited by LOT afferents (Tseng and Haberly 1988). In the model, afferent excitation (with *NMDA* and *non-NMDA* components) and $GABA_B$ inhibition are restricted to layer Ia.

The time constants for the *non-NMDA* synapses were chosen to fit experimental data on the time course of *non-NMDA* conductances in hippocampal pyramidal cells (Mason et al. 1991). Our model of *NMDA*-mediated synapses was identical to that used by Holmes and Levy (1991). Time constants for $GABA_B$ synapses were chosen to match experimental data on the time course of $GABA_B$ responses in rat

hippocampal neurons (Ling and Benardo 1994). The times to peak of all synaptic conductances are shown in table 3.1.

Layer Ib Anatomical studies in piriform cortex show that layer Ib contains projections from pyramidal cells in different areas of piriform cortex, as well as from other olfactory areas (Luskin and Price 1983). This layer can be further subdivided into superficial and deep areas. Physiological and anatomical evidence suggest that the superficial area contains caudally directed excitatory fibers from rostrally located piriform pyramidal neurons while deep Ib contains rostrally directed excitatory fibers originating in more caudally located piriform pyramidal neurons (Luskin and Price 1983, Rodriguez and Haberly 1989, Ketchum and Haberly 1993a). Pharmacological studies show the presence of both $NMDA$ and *non-*$NMDA$ type responses throughout layer Ib (Jung et al. 1990, Kanter and Haberly 1990). Experimental evidence further suggests that the $NMDA$ component in layer Ib is significantly stronger than that found in layer Ia (Kanter and Haberly 1990). This layer therefore had a higher $NMDA$ channel density.

Layer II Layer II of the piriform cortex contains the somata of the superficial pyramidal neurons. Physiological studies have shown the presence of a fast $GABA_A$ inhibition localized to layer II (Tseng and Haberly 1988, Kanter et al. 1996) and this is the sole location of the fast $GABA_A$ inhibition in the model. However, very recent work by Kanter et al. (1996) has shown the presence of a dendritic $GABA_A$-mediated inhibition that exists in layer I dendritic areas. This newly discovered $GABA_A$ mediated inhibition appears to operate independently of the layer II inhibition and seems to be primarily involved in the regulation of LTP (Kanter et al. 1996). Since these simulations do not address questions of synaptic plasticity, we have not included this synaptic current in our single cell model.

Layer II inhibition in the model differed from other types of synaptic input in that its amplitude was kept relatively constant (scaled to be able to cancel coincident suprathreshold excitation). This was done based on results from hippocampus

that show single GABAergic neurons (mediating $GABA_A$ inhibition) capable of effectively phasing spikes in hippocampal pyramidal neurons (Cobb et al. 1995) and furthermore that these interneurons contact up to 1000 pyramidal cells (Li et al. 1992, Sik et al. 1995). Recent hippocampal studies have also shown that networks of inhibitory neurons can become tonically activated such that they fire synchronously and independently of fast excitation from the pyramidal neurons that they inhibit (Whittington et al. 1995). Given these results, one might expect that this inhibition would not necessarily scale with the excitatory input that an individual cell is receiving. Also, since a single spike in an inhibitory interneuron is capable of having a dramatic effect on a pyramidal neuron, inhibition may very well be the result of a single synaptic event. Therefore, we should expect a constant amplitude for $GABA_A$ inhibition.

Layer III The basal dendrites of superficial pyramidal neurons and the somata of deep pyramidal neurons are located in layer III. Anatomical studies indicate that connections between local pyramidal cells are made on the basal dendrites of deep and superficial pyramidal neurons (Haberly and Presto 1986). Unfortunately, little is known about basal dendrite physiology and so we have chosen not to incorporate this system into our model.

Figures 3.1 and 3.2 summarize the synaptic receptor and pathway information described above.

3.3.2 Synaptic background activity

In order to better simulate the behavior of the cell in the awake-behaving animal, synaptic background activity was added to the model. In the absence of odor stimuli, single unit recordings from the piriform cortex of behaving rats reveals two types of spontaneously firing neurons: class I neurons had mean firing rates of less than 10 Hz (believed to be pyramidal cells) while class II (believed to be inhibitory interneurons) showed firing rates of 30-100 Hz (McCollum et al. 1991). We modeled this activity by using mean frequency values of 7 Hz for excitatory synapses and 50 Hz for

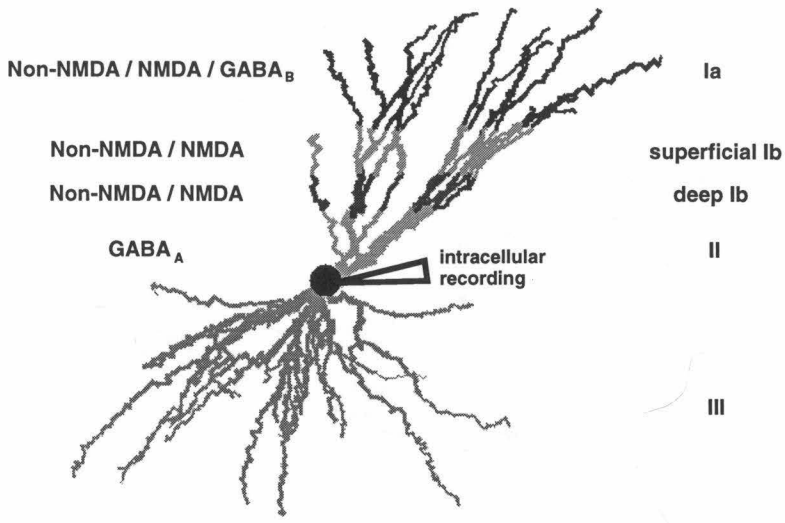

Figure 3.1: An anatomical representation of the model cell. Differently shaded areas represent anatomical layers within the piriform cortex and are labeled on the left. The soma (shown as a black sphere) is located in layer II. The receptors present in each layer in the model are listed on the left. All intracellular recordings shown in this chapter are recorded from the soma unless otherwise indicated.

inhibitory ones. Pyramidal neurons are believed to have on the order of 10,000 excitatory synapses (Larkman 1991); however, for reasons of computational efficiency, we modeled only 1022 background excitatory synapses. Similarly, only 66 $GABA_A$ and 200 $GABA_B$ background synapses were included in the model. In order to normalize for the greater number of synapses found in the real neuron, we used the following formula to calculate the effective mean frequency of individual modeled synapses:

$$\omega = \frac{N\theta}{M} \tag{3.3}$$

(Rapp et al. 1992)

where ω represents the effective mean frequency, N is the number of synapses in the real neuron, q is rate of firing in the biological system, and M is the actual number of synapses in the model. An identical procedure has been used in other single cell models (De Schutter and Bower 1994a, Rapp et al. 1992). For excitatory background synapses, an ω value of 70 Hz was used. Assuming that 20% of all synapses are

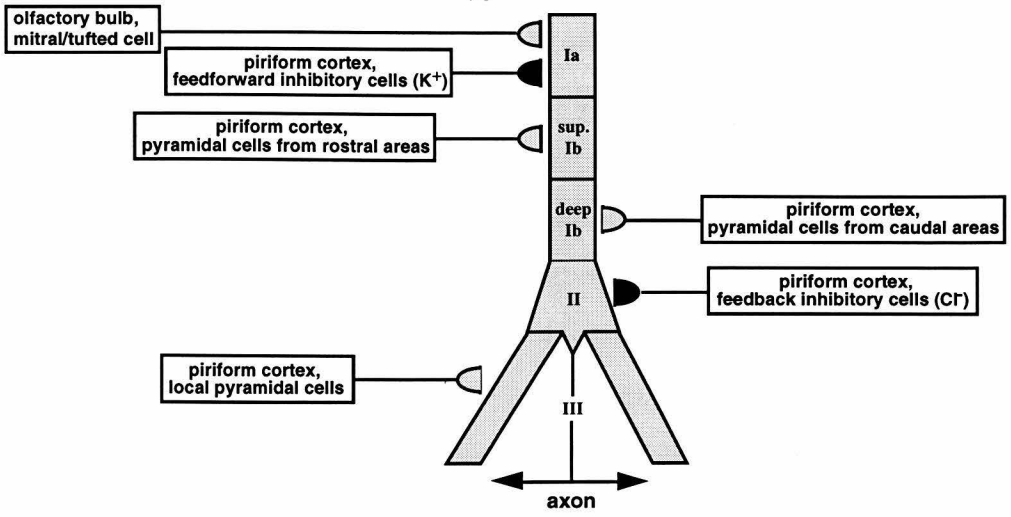

Figure 3.2: Input to piriform pyramidal cells is segregated to different layers depending on its origin. Afferent input terminates in layer Ia. Associative input to layer Ib tends to come from distant rostral and caudal pyramidal cells, while layer III input tends to come from local pyramidal cells. Because of the dearth of information about basalar inputs, this pathway is not incorporated into the model. All superficial pyramidal cells have their cell bodies in cortical layer II.

inhibitory (Peters 1987) and that there are equal numbers of $GABA_A$ and $GABA_B$ synapses, we calculated ω values of 950 Hz and 312 Hz for $GABA_A$ and $GABA_B$ synapses respectively.

Intracellular recordings from the motor cortex of conscious cat show that neuron resting potentials are typically 5-20 mV more depolarized than those seen in the *in vitro* motor cortex (Baranyi et al. 1993). Channel densities for background excitatory channels were adjusted to raise the resting potential of the model cell to the range seen by Baranyi and colleagues (1993). Channel densities for inhibitory background synapses were similar to those for excitatory background channels. Resting membrane potential in the presence of background activity was in the neighborhood of -62 mV.

3.3.3 Spike arrival times

Spike arrival times were modeled using results from a systems simulation constructed by Ketchum and Haberly (1993b) to explain the spatio-temporal pattern of sources and sinks seen in experimental current source density studies (Ketchum and Haberly

1993a, Rodriguez and Haberly 1989). In the Ketchum and Haberly (1993b) simulation, distributions of spike arrival times are derived for different excitatory pathways on the basis of anatomical and physiological data. These distributions when convolved with synaptic response functions in a cable representation of a population of piriform pyramidal cells was able to replicate experimental CSD data.

Since we are using these distributions to model input to a single piriform pyramdal neuron, we discretize the arrival time distributions such that they each represent histograms with a total of 100-300 synaptic events per excitatory pathway. This is based on the assumption that each pathway should be capable of generating an action potential and from studies of hippocampal neurons that indicate that epsps that are elicited by single axonal spikes range in amplitude from 30 to 665 μV (Sayer et al. 1990, Sayer et al. 1989, McNaughton et al. 1981). Figure 3.3 shows arrival time distributions used for excitatory pathways.

3.4 Results

Gamma oscillations (30-50 Hz) in the piriform cortex are typically evoked by the presence of odors in a context-dependent way (e.g., a hungry animal responding to food smells) in awake-behaving animals (Freeman 1960, Woolley and Timiras 1965). Gamma activity is further modulated by slower oscillations (1-4 Hz) that are correlated with respiration (Freeman 1959, Freeman 1960, Woolley and Timiras 1965) in such a way that a burst of gamma oscillations is superimposed on a single respiratory wave. During periods of sniffing, the slow wave increases in frequency to match the sniffing rate (Freeman 1960) which more closely approximates the theta rhythm (4-12 Hz) (Macrides et al. 1982). Periods of burst activity are usually separated by periods of relative quiescence.

The current source density analysis of Ketchum and Haberly (1993abc) suggests that piriform cortex pyramidal cells are subjected to repeated sequences of distal to proximal synaptic activation on their apical dendrites during each gamma oscillation in the EEG. For the remainder of this chapter we will refer to the pattern of synaptic

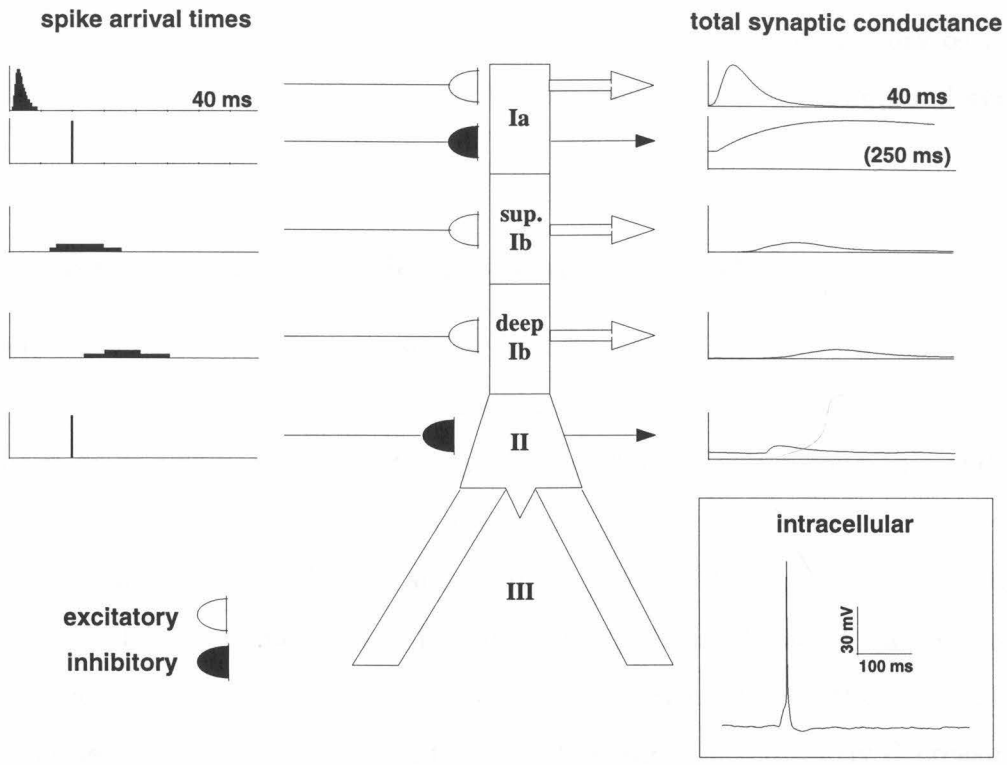

Figure 3.3: Model response to synaptic input believed to underlie a single gamma oscillation. Graphs on left show spike arrival time histograms for different pathways. Excitatory input along different pathways typically consisted of on the order of hundreds of spikes per spike arrival time histogram. The graphs on the right show summed synaptic input over respective dendritic layers for different pathways. Inset shows simultaneous intracellular recording.

activity believed to underlie a single gamma oscillation as a "gamma sequence." When this pattern is repeated many times to simulate burst activity, it will be called a "burst sequence." In the results that follow we describe the response of our model cell to the patterns of synaptic input believed to underlie gamma and respiratory oscillations. In the first section we examine the cell's response to realistic patterns of background synaptic input. This is later used as the baseline activity under which all subsequent simulations are performed. In the next section, we describe the model's response to the pattern of synaptic input believed to underlie a single gamma oscillation. The changes induced by this pattern of synaptic activity are longer lasting than the 25 *msec* duration of the gamma oscillations normally seen in the EEG and in the next section of the results we discuss the implications of these longer lasting effects in

the context of activity that takes place over the duration of a respiratory oscillation (100-250 $msec$). We begin with our results concerning random background synaptic input.

3.4.1 Response to random synaptic input

Random background activity was scaled to increase resting membrane potential by 7 mV in keeping with studies that compare resting potential in slice to intracellular recordings from awake animals (Baranyi et al. 1993). Having done this and using the rates of background firing described in our methods section, we obtained the baseline shown in figure 3.4 with standard deviation (SD) 0.43 mV. Addition of random synaptic input had two important consequences. First, it had a dramatic effect on the passive properties of the neuron by increasing the electrotonic length of the apical dendrite by as much as a factor of two and concomitantly decreasing the passive time constant from 23.6 to 9.7 $msec$. Bernander *et al.* (1991) reported similar results for their neocortical model with the electrotonic length of the cell changing by a factor of 3 and time constant decreasing by a factor of 10. The change in electrotonic structure is shown in figure 3.4. The decrease in time constant suggests that a neuron's integration time might be much shorter in the awake animal than slice data may suggest.

A second consequence of random synaptic input deals with the induced fluctuations in membrane potential. We compared the power spectra of membrane potential fluctuations in the presence and absence of voltage-gated currents and found that the cell's response differed significantly in each of those cases. Figure 3.5 shows the power spectra in the active and passive cases. The spectra associated with the absence of active conductances show a roughly monotonic decrease in power from low to high frequencies. This is in marked contrast to power spectra taken from instances where active conductances were included in the model. In these cases, an increase in power is seen in the frequency range of 5-15 Hz. This effect is not particularly sensitive to the types of synaptic input used ($non\text{-}NMDA$, $GABA_A$, and $GABA_B$), since it

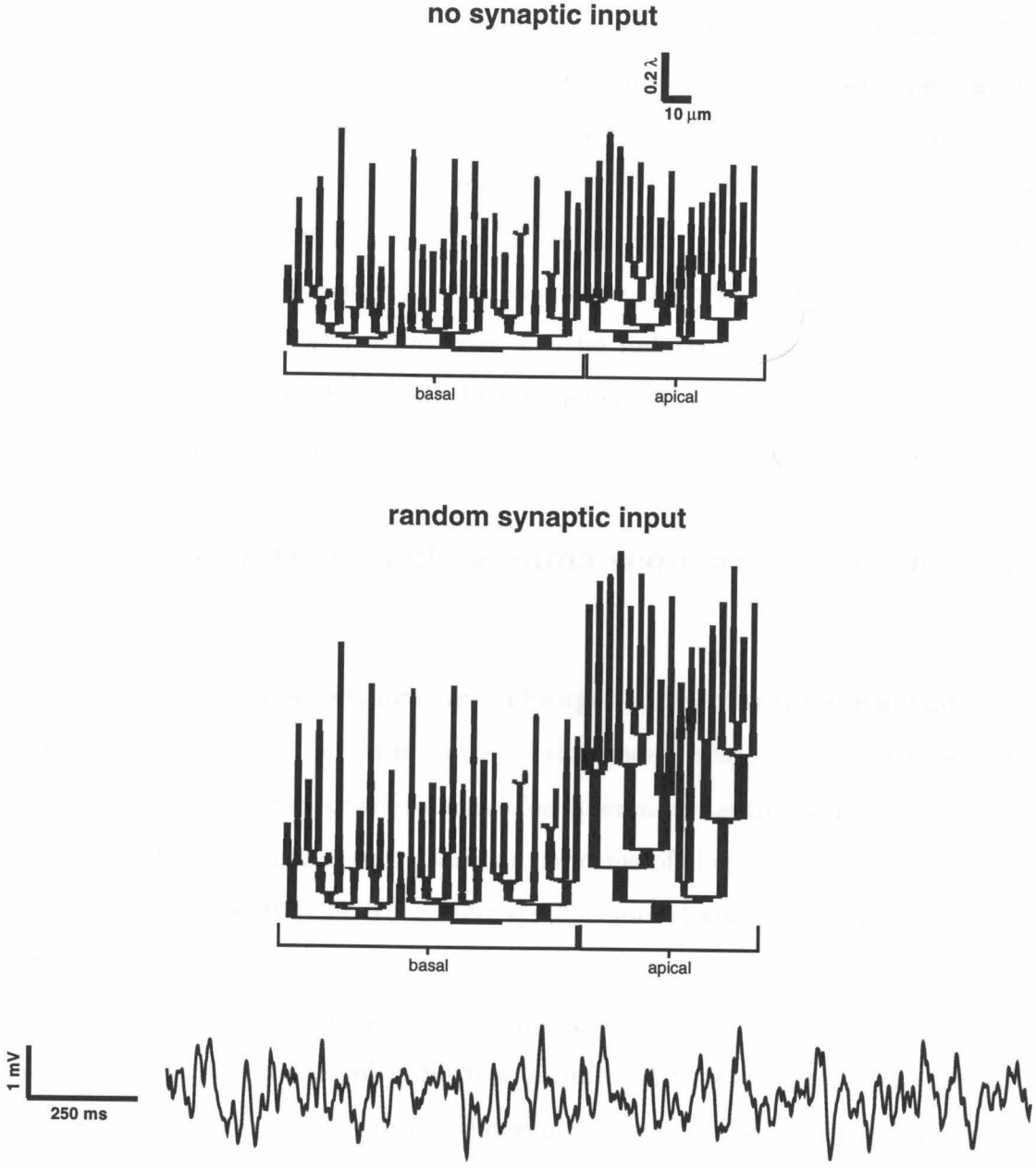

Figure 3.4: Changes in electrotonic structure due to the addition of random synaptic input. Random synaptic input increases the electrotonic length of the apical dendrite by approximately 50%. Membrane potential in the presence of synaptic background activity is shown at bottom.

is robust to the combination of synaptic inputs used in generating background noise (see Figure 3.5). Although different combinations of synaptic channel types used to induce background activity have an effect on the amplitude of the power spectra, the spectral profile remains constant. This suggests that synaptic noise of almost any type is capable of inducing low frequency (5-15 Hz) subthreshold oscillations. In chapter 2 we reported that the injection of broadband noise in piriform pyramidal neurons resulted in subthreshold oscillations in the theta rhythm range (4-12 Hz). Here we show that such oscillations may also be induced by background synaptic input. This result suggests that cortical neurons may be oscillating at physiologically relevant rhythms even in the absence of sensory stimulation (see Discussion).

3.4.2 Response to a single gamma sequence of synaptic input

Timing of synaptic conductances and changes in membrane potential Figure 3.3 illustrates several different measures of the model's response to a single gamma sequence. Histograms for spike arrival times for different synaptic pathways are shown to the left of the schematized cell. Continuous forms of these histograms were used by Ketchum and Haberly (1993b) in their systems model analysis of piriform cortex CSD data.

Graphs of total synaptic conductance summed over different layers of the apical tree are shown to the right and indicate the different time courses of the induced synaptic conductances. A peak in afferent synaptic conductance clearly occurs first followed by a peak in fast $GABA_A$ inhibition followed by peaks in associative excitation in layer Ib. Interestingly, the peak $GABA_B$ inhibition occurs long after the rest of the synaptic conductance sequence has ended with a peak at roughly 170 $msec$.

The graph of membrane potential in the figure 3.3 inset marked "intracellular" shows a single spike that is generated by the gamma sequence. Synaptic inputs were never scaled so high that a single gamma sequence could generate more than a single spike. This was done to conform to experimental data in awake behaving

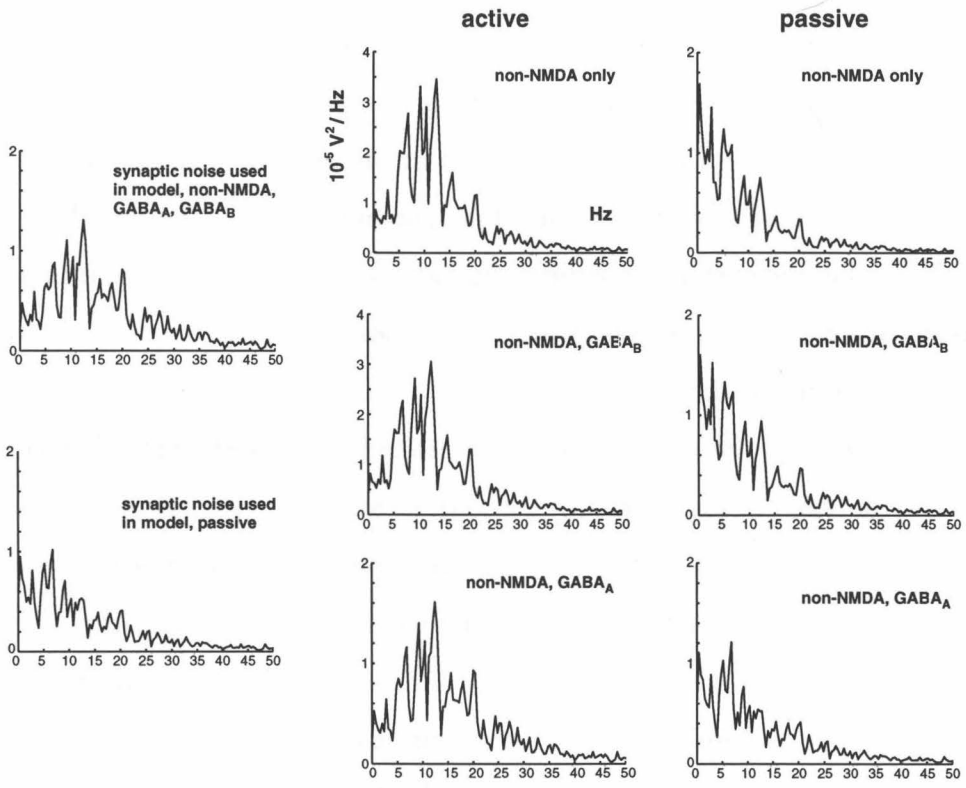

Figure 3.5: Power spectra of membrane potential recorded over 20 *sec* in the presence of synaptic noise. Power spectra were taken in the presence and absence of voltage-gated channels. Spectra taken in the presence of voltage-gated channels show an amplification of frequency components in the 5-15 Hz range (approximately theta/sniffing rhythm). Graphs on the right two-thirds of the figure show that different combinations of synaptic channels do not have a significant effect on the profile of power spectra.

animals which seems to suggest that piriform pyramidal cells generally do not spike at rates higher than 10 Hz (Schoenbaum and Eichenbaum 1995, McCollum et al. 1991). Additionally, intracellular recordings from piriform cortex pyramidal cells indicate that a strong shock to the LOT only elicits a single spike from individual neurons (Haberly and Bower 1984). The intracellular trace also shows that examination of a cell's membrane potential often gives little or no information about the complex patterns of synaptic input that the cell might be receiving.

Effect of synaptic conductances on dendritic electrotonic structure In figure 3.6 we examine the effects of a gamma sequence on the electrotonic structure of the apical dendritic tree. The apical tree is represented by a dendrogram where each layer is differentially shaded and segment length is indicative of electrotonic length. Each dendrogram is taken at the peak of summed synaptic conductance for different pathways. Here we use electrotonic length to measure changes in the passive structure of the model, but we do not mean to imply that changes in electrotonic length proportionally translate into changes in the efficacy of synaptic inputs. Although changes in the passive structure of the cell will have an impact on the efficacy of synaptic inputs, this will also depend on other factors such as the reversal potential of the synaptic conductance and the membrane potential of segments where synaptic input is arriving.

Changes in electrotonic structure occur in the following sequence. Dramatic changes in the electrotonic length of layer Ia compartments are seen within 4.0 $msec$ (from onset of gamma sequence) where the average electrotonic length in this layer increases by approximately a factor of two. This is followed by a 50 percent increase in layer II at 11.5 $msec$ in response to $GABA_A$ input. Superficial and deep Ib excitatory inputs then exert their peak influence on the electrotonic structure of the cell at 14 and 21 $msec$. Finally peak effects for $GABA_B$ inhibition occur at 167 $msec$. There are two interesting things to note about this sequence of events. The first is that excitatory inputs exert their effects on the electrotonic structure of the model in a distal to proximal direction. Past work has shown that this progression is optimal

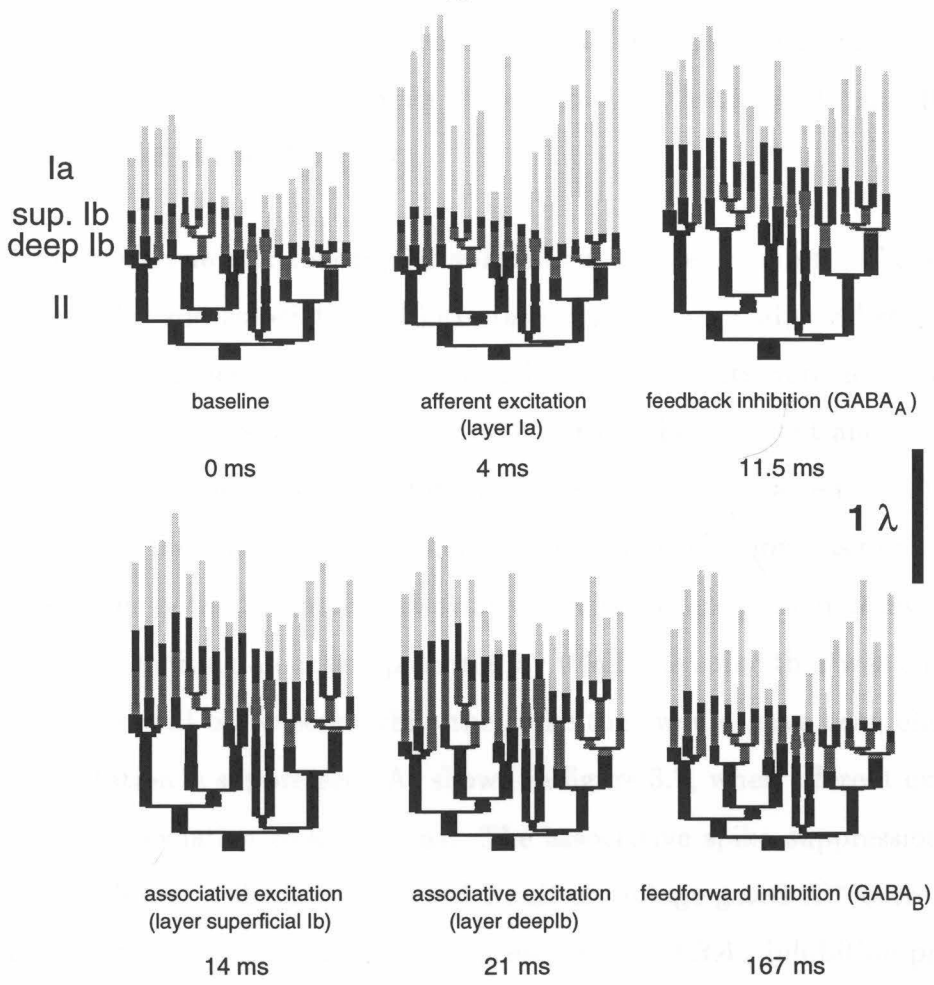

Figure 3.6: Changes in electrotonic structure of neuron during the course of a single gamma oscillation. Dendrogram in upper right shows the cell's electrotonic structure in the presence of synaptic noise prior to gamma-type synaptic input. Subsequent dendrograms are taken at times when the synaptic conductance elicited by activity along a particular pathway has peaked. The level of synaptic conductance induced by activity along different pathways was shown in figure 3.3. The time at which the dendrogram was taken and the pathway induced synaptic conductance that has peaked at that moment are shown beneath each dendrogram. Times correspond to the times shown in figure 3.3. At the peak of afferent excitation, the most distal portions of the apical dendrite show a dramatic increase in electrotonic length while the remaining dendrite maintains the electrotonic structure it had at baseline. $GABA_A$ inhibition is next to peak and dramatically increases the electrotonic length of the most proximal dendritic segments thereby isolating the soma from excitatory input. While proximal segments are electrotonically extended, excitation arriving via the associative superficial Ib pathway peaks. This is followed by peak deep Ib excitatory input which occurs just as the proximal portion of the dendritic tree is recovering from $GABA_A$ inhibition. $GABA_B$ inhibition is the last to peak (167 *msec* later) by which point dendritic segments proximal of layer Ia have settled down to baseline conditions, but Ia segments have become elongated, suggesting that the electrotonic effect of this inhibition is felt only by incoming afferent input.

for exciting a neuron (Rall 1964). The second is that the $GABA_A$ effects are maximal between the peak synaptic conductance of excitatory pathways in Ia and Ib. This may act to segregate Ia and Ib inputs.

Consequences of synaptic timing for somatic spike generation The strength of both afferent (Ia) and associative (Ib) excitatory inputs were adjusted so that each pathway was able to generate a somatic spike. Inhibitory inputs were not changed at all. Figure 3.7 shows the results of these simulations. When afferent and associative excitatory inputs were both present (normal situation for gamma sequence) a spike was generated with the same timing as when only afferent excitation was present. This indicates that when both afferent and associative excitation are present at levels where each is capable of eliciting an action potential by itself, the spike that was elicited by afferent excitation will be present, while the spike that would have been elicited by associative excitation is suppressed. As shown in figure 3.7, when afferent excitation is removed, the associative spike returns. The associative spike suppression in the presence of an afferent spike is a combined result of voltage-gated K^+ currents that are activated by the afferent spike and the presence of $GABA_A$ inhibition preceding associative excitation.

3.4.3 Response to multiple gamma sequences within a burst sequence

Impact of a single gamma sequence within a burst sequence One fundamental question that we wanted to answer is how individual gamma sequences interact with each other to affect the behavior of the neuron during the course of a burst sequence. We examined this first by looking at the impact on the electrotonic structure of the apical dendrite of a single gamma sequence. Figure 3.8 shows the results. For the sake of illustration, background synaptic activity was removed from these simulations. As can be seen in the figure, the electrotonic structure of the neuron is significantly altered from baseline even at 25 $msec$ following the onset of the gamma

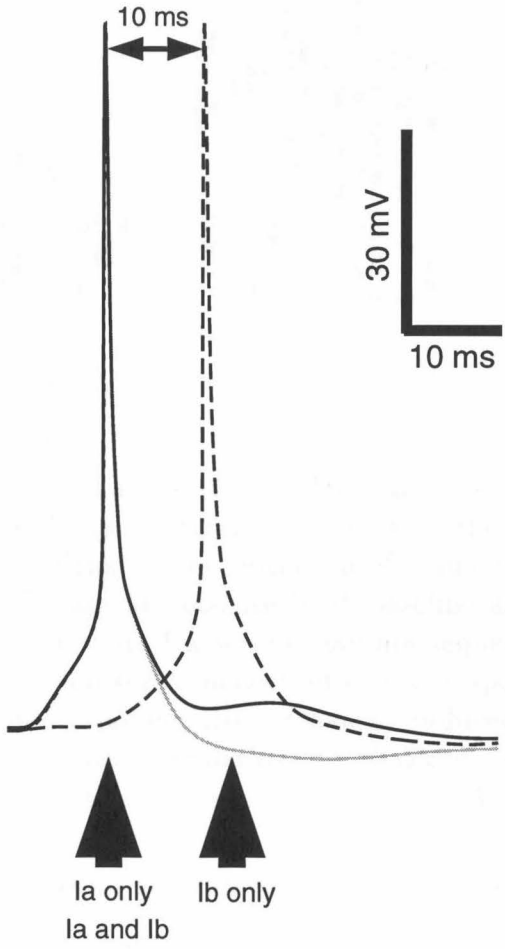

Figure 3.7: Spike timing can yield information about the origin of synaptic excitation. Using the pattern of excitation and inhibition believed to underlie gamma oscillations in awake behaving animals, afferent (Ia) and associative (superficial and deep Ib) excitatory inputs were each scaled to the point where each alone could elicit a spike. Afferent stimulation (gray line) produced a spike that took place 10 *msec* before the spike produced by associative input alone (dashed line). When the afferent and associative inputs used to generate the aforementioned spikes were combined, a single spike (solid black line) was generated at the same position as the spike elicited by afferent stimulation alone. The large difference in timing between the two spikes suggests that spike timing may contain information about the origin of excitation.

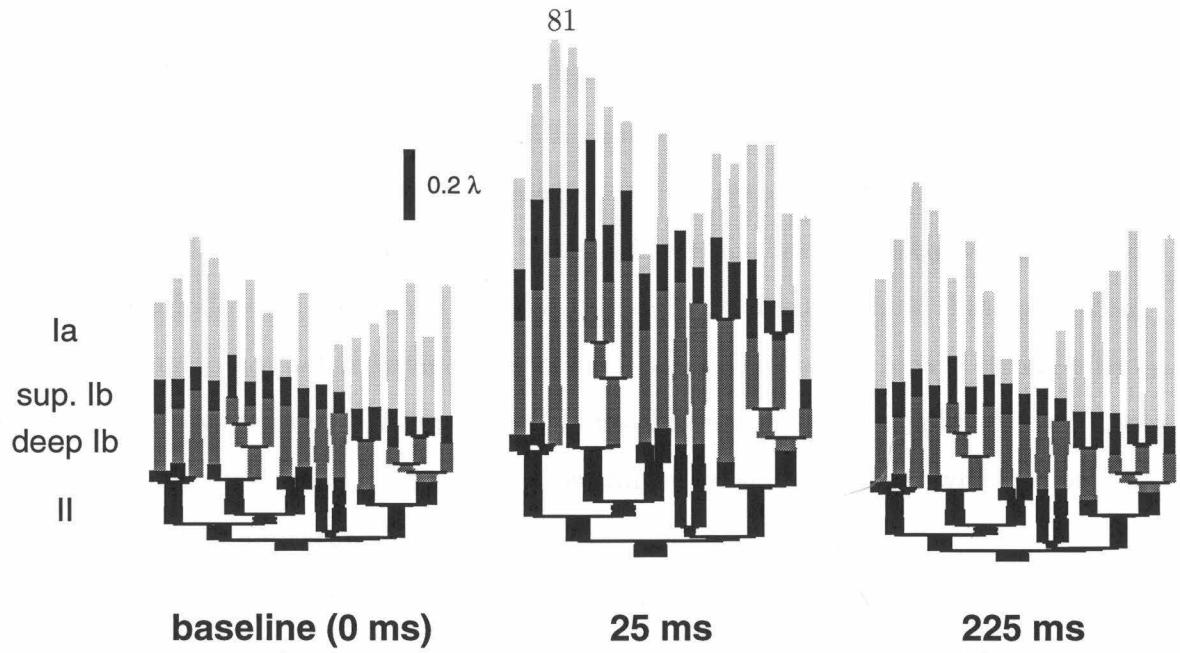

Figure 3.8: The duration of changes in the electrotonic structure of the piriform pyramidal cell exceeds the 25 *msec* interval time between the gamma sequences that make up a theta sequence. Prior to the initiation of a single gamma sequence, the electrotonic structure of the apical dendrite is at baseline as shown on the left of the figure. Prior to the initiation of a second gamma sequence 25 *msec* later, the electrotonic structure of the cell shows persistent changes, specifically elongations in the layer Ib and II portions of the dendrite. Changes induced from a single gamma sequence persist long after the last presynaptic spike has arrived at the dendrite. Even 225 *msec* later, layer Ia shows elongation resulting from $GABA_B$ synaptic activity.

sequence. At this time a second gamma sequence would be initiated as part of a burst sequence, yet it is clear that the electrotonic structure of the cell retains the influence of the previous gamma sequence. While segments in the Ia portion of the dendrite have reset to their baseline electrotonic lengths, segments in layers Ib and II are still significantly extended. This means that when synaptic input from a second gamma oscillation impinges on the cell, it will be filtered through an apical dendritic tree whose electrotonic structure has been determined by the previous gamma input.

If individual gamma inputs during a burst act relatively independently of each other, then one would expect that the number of spikes produced by a particular sequence of gamma inputs should be conserved when the ordering of individual gamma inputs is rearranged. To test this possibility, we changed the ordering of gamma inputs which had elicited two spikes during the course of a burst so that the strongest gamma

inputs were clustered around the center of the burst. A comparison of these simulation runs before and after the rearrangement is shown in part A of figure 3.9. When the inputs were rearranged the burst produced a total of one spike where it had produced two previously. This was due to the hyperpolarization mediated by voltage-gated K^+ channels following the induction of a spike. These results show that individual gamma inputs do not act independently of each other, but rather have a strong effect on each other. More precisely, this result shows that not only the amplitude, but also the temporal position of a gamma input within a burst determines whether or not that input will be suprathreshold.

To characterize the impact of a single gamma input on the course of a burst, we ran pairs of simulations where model parameters (including synaptic noise) were kept identical except for the amplitude of the first gamma sequence in the burst sequence. In one case (shown in part B of figure 3.9), a subthreshold input was scaled to be suprathreshold and the responses from the two runs were compared. This change resulted in the cancellation of a spike that had previously resulted from the second gamma sequence. It should further be noted that the two traces did not reconverge for 106 $msec$ (to within 100 μV) suggesting that the effects of a single gamma oscillation can be long lasting within a burst sequence. A less extreme divergence in behavior was observed when the first subthreshold input was scaled to a different subthreshold level. The results of these simulation runs are shown in part C of figure 3.9. Although this change was more subtle than turning a subthreshold input into a suprathreshold one, its effects were still long lasting. A reconvergence of the two traces (to within 100 μV) was only observed after 87 $msec$.

Effects of $GABA_A$ inhibition during a burst Initial simulations showed that $GABA_A$ mediated inhibition was able to alter the timing of individual spikes. We anticipated therefore that the $GABA_A$ inhibition would act to bin spikes during the course of a theta burst. However, when we ran multiple simulations with and without $GABA_A$ inhibition, we found that this was not the case. Figure 3.10 shows multiple overlaid graphs of intracellular activity during the course of a theta burst in the

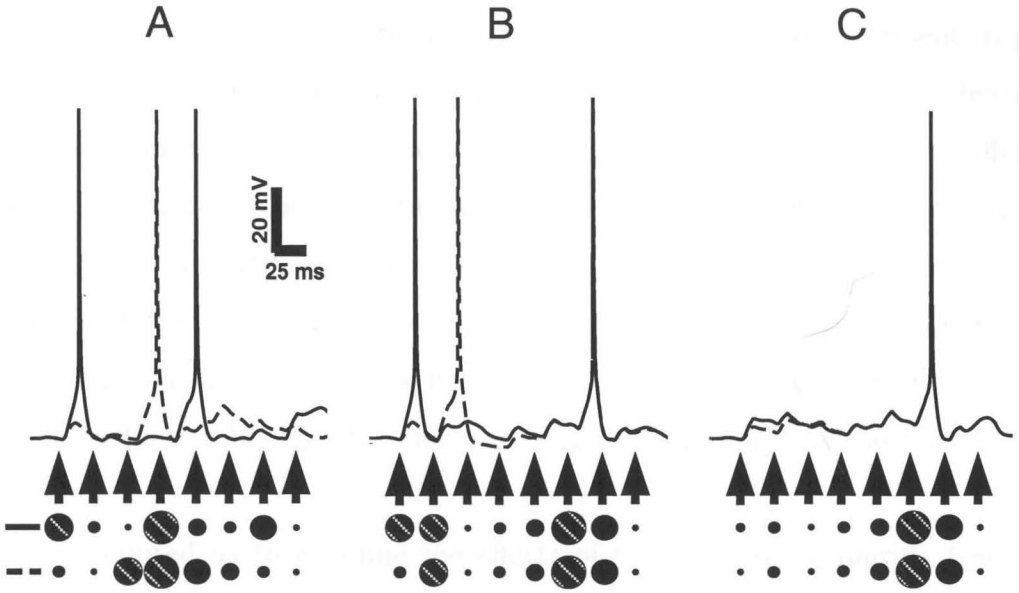

Figure 3.9: To simulate theta activity, the spatio-temporal pattern of synaptic input believed to underlie gamma oscillations was repeated eight times, scaling the strength of each iteration of the pattern randomly. The diameter of the circles is proportional to the strength of individual gamma inputs. Hatched circles represent suprathreshold synaptic input in the presence of only baseline noise. Arrows mark the beginnings of different gamma sequences. In part A, eight input patterns which produce two spikes in one case (solid line) are rearranged in time such that the strongest inputs are clustered in the middle (dotted line). In all parts of the figure the baseline noise was identical in the pairs of traces. In the case where the two suprathreshold inputs are clustered, only one spike is produced. This suggests that the timing of a synaptic input is as important as the amplitude in determining whether or not the cell will fire during the course of theta activity. In part B, the patterns of stimulation are identical except that in one case the first iteration of gamma activity is suprathreshold (solid line) and in the second it is subthreshold (dotted line). The effects of changing a single input from sub to suprathreshold are long lasting. It takes 106 *msec* for the two traces to converge ($\Delta V_m < 100\mu V$) again. This result also shows that responses to individual iterations of the synaptic pattern underlying the gamma oscillations are not independent from other iterations during the course of theta activity. Part C shows the effects of changing the amplitude of a subthreshold input to a subthreshold input with a different strength. As was the case in part B, the effects of this change last beyond the duration of a single iteration of gamma input with reconvergence (within 100 μV) of the traces taking place after 87 *msec*.

presence and absence of $GABA_A$ inhibition. Beneath each series of traces is a histogram of spike times for each time interval between successive $GABA_A$ inhibitory inputs. Each trace on the left side of the figure ($GABA_A$ inhibition present) is paired with a trace on the right side ($GABA_A$ not present) with both traces identical in the amplitude of individual gamma inputs and synaptic noise. Therefore, differences between the two halves of the figure are entirely due to the effects of $GABA_A$ inhibition. The two primary differences are in the total number of spikes (presence of $GABA_A$ inhibition causes a decrease) and in the standard deviation of spike timings between $GABA_A$ inhibitions (presence of $GABA_A$ increases standard deviation values). The latter result suggested that $GABA_A$ input does not act to bin spikes in a single neuron.

This prompted us to examine the effects of $GABA_A$ by comparing traces that were identical except for the presence of $GABA_A$ inhibition. Two examples of such comparisons are shown in figure 3.11. In one case (part A), the two traces are almost identical with spikes lining up almost perfectly despite the fact that one trace was generated in the presence of $GABA_A$ inhibition and the other was not. Part B, however, shows a very different story. In this case $GABA_A$ inhibition shifts the timing of the first spike by almost 10 $msec$ and eliminates a second spike entirely. This figure therefore suggests that $GABA_A$ input may increase the temporal requirements for spiking. If excitatory input arrives at "good" times as it does in part A, then the neuron will spike; however, if it arrives at "bad" times it will not spike as is the case in part B.

3.4.4 Consequences of delays between burst sequences

Previous sections showed that gamma sequences did not have independent effects on a pyramidal neuron during the course of a burst. A single gamma input could exert an effect that would last in excess of 100 $msec$. This prompted us to ask how far apart two bursts would have to be in order for them to have no effect on each other. The results of these simulations are shown in figure 3.12. A sequence of two bursts

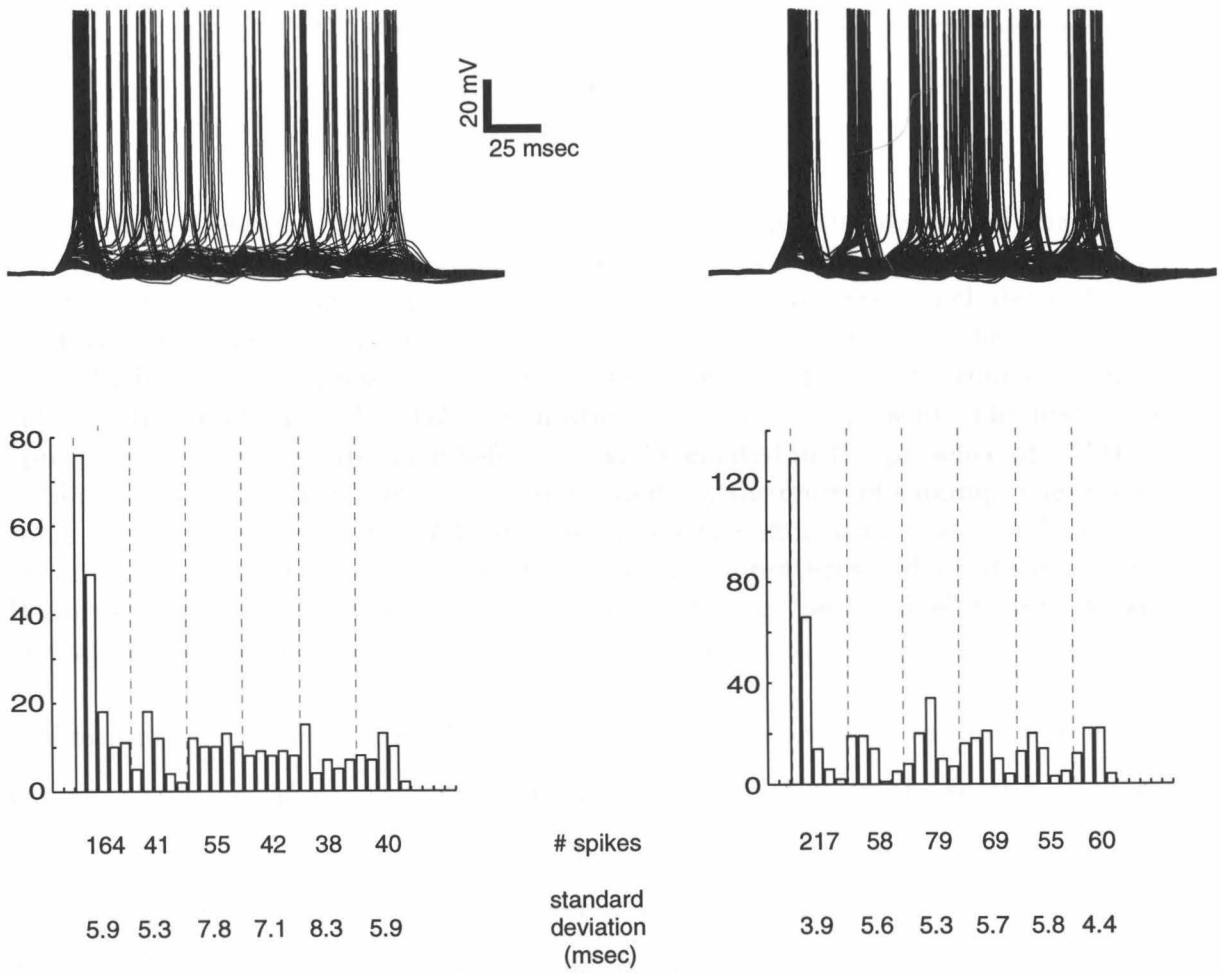

Figure 3.10: Dependence of spike timing on $GABA_A$ inhibition. Each trace on the left has an identical companion on the right which lacks $GABA_A$ inhibition. Presence of $GABA_A$ inhibition reduces the total number of spikes but increases the standard deviation of spike times in bins demarcated by onset of $GABA_A$ inhibition (indicated by dotted lines in figure).

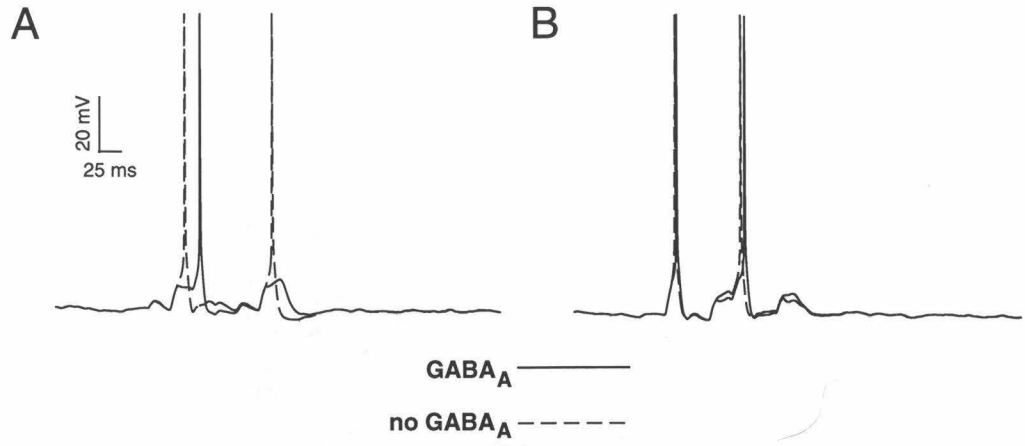

Figure 3.11: $GABA_A$ inhibition increases temporal requirements for spiking. Part A compares two traces where baseline noise and patterns of synaptic excitation are identical during the course of theta activity. The solid line trace includes $GABA_A$ inhibition whereas the trace made from the dotted line does not. In the case where $GABA_A$ inhibition is present, only one spike is elicited during the course of theta activity. In the absence of $GABA_A$ inhibition two spikes are present. The first spike appears approximately 10 *msec* before the spike elicited in the presence of $GABA_A$ inhibition showing that $GABA_A$ inhibition can delay the onset of spiking. The second spike is not present when $GABA_A$ inhibition is active indicating that $GABA_A$ inhibition can increase the temporal requirements for suprathreshold excitation. Part B shows what happens when excitation arrives during "permissive" times. Spikes overlap in the presence and absence of $GABA_A$ inhibition.

is shown in each of the traces where the first two bursts are different and the second two are the same. If activity in the first burst has no effect on the second, then we will expect the second set to overlap perfectly. This is not the case in the top set of traces, nor is it the case in the middle set where bursts are separated by 325 *msec*. The long lasting effect of a burst is primarily due to the late onset of the $GABA_B$ inhibition that is initiated by the first burst. In the bottom set of traces we see that an interburst separation time of 650 *msec* is sufficient to eliminate the effect of the first burst on the second. Of course the length of the "sufficient" gap is dependent on primarily the strength of $GABA_B$ activity in the first burst and the number of gamma sequences in the first burst. Had the first burst consisted of fewer gamma sequences, the gap would not have to be as long.

To better quantify the relationship between the number of gamma sequences and the strength of the $GABA_B$ inhibition, we generated multiple $GABA_B$ inputs at 25

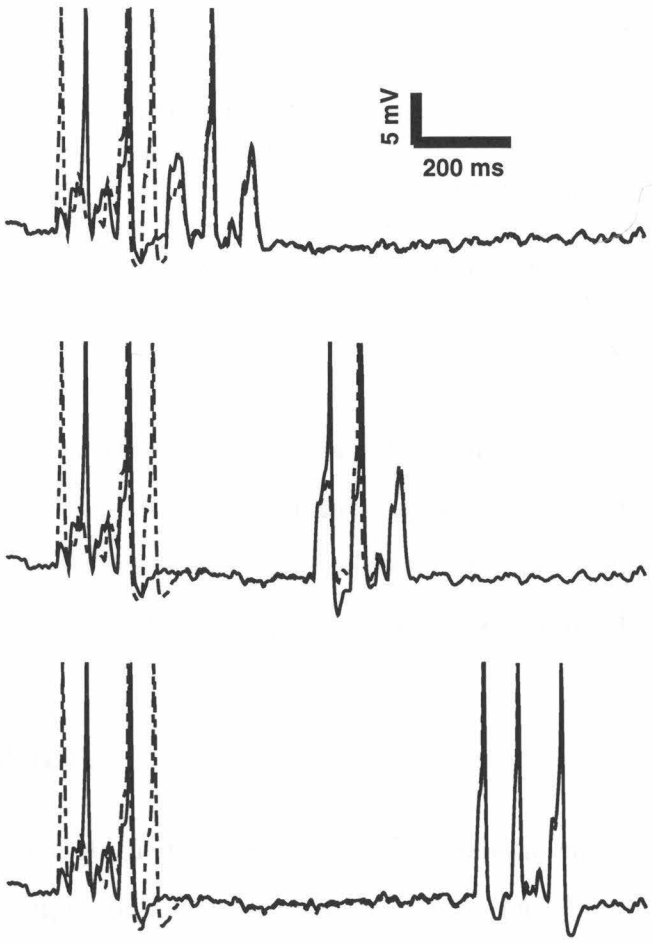

Figure 3.12: Temporal gaps between burst sequences determine how activity in the first burst will effect activity in the second. Gamma sequences underlying the two bursts in each set of traces is the same. Top set show burst sequences separated by 25 *msec*. Middle traces show bursts separated by 325 *msec* and bottom bursts are separated by 650 *msec*. Top two sets of traces show that activity in the second burst is clearly dependent on activity in the first. Bottom trace shows that the second burst is independent of activity in the first. In the biological network, $GABA_B$ inhibition may act to space out bursts so that they have minimal effects on each other. Top portions of spikes are truncated for the purpose of illustration.

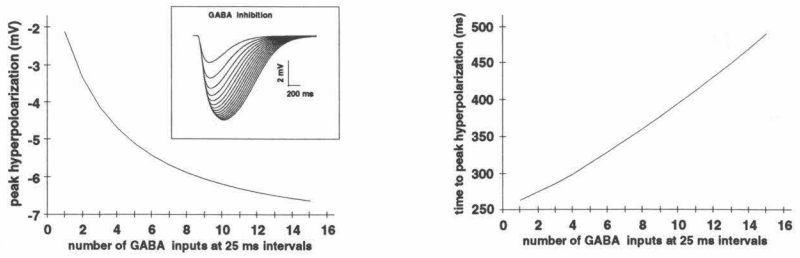

Figure 3.13: The effects of multiple $GABA_B$ inputs. The model activates a $GABA_B$ input during each gamma oscillation. For this figure $GABA_B$ inputs were repeated at 25 *msec* intervals. Left graph shows the relationship between number of $GABA_B$ inputs and peak hyperpolarization. Right graph plots number of $GABA_B$ inputs against time to peak hyperpolarization. The relationship is roughly linear with peak times ranging from 246 *msec* to 493 *msec*.

msec intervals and then plotted the time to peak hyperpolarization and the level of peak hyperpolarization vs. the number of $GABA_B$ inputs. The results of this analysis are shown in figure 3.13 and suggest that the hyperpolarizing effect of the $GABA_B$ inhibition will begin to saturate after approximately 8 repetitions while the time to peak only doubles as the number of repetitions increases from 1 to 15.

3.5 Discussion

In this chapter we have studied the response of a realistic single cell simulation to patterns of synaptic input believed to underlie gamma and theta oscillations in the piriform cortex. Past single cell models have examined the effects of idealized patterns of synaptic input (i.e., sparse vs. localized, synchronous vs. periodic, etc.) on the behavior of single neurons (Agmon-Snir and Segev 1993, Murthy and Fetz 1994, Bernander et al. 1994, Bernander et al. 1991, Rapp et al. 1992). Our study differs from this past work because the patterns of input are tied to specific biological phenomena. In the discussion below we explore some of the computational implications of our results and their possible importance in the context of network functioning.

3.5.1 Patterned response to unpatterned stimuli

Our model shows that temporally unpatterned synaptic input is capable of generating subthreshold membrane oscillations in the range of 5 to 15 Hz. This frequency range correlates nicely with the theta frequency (4-12 Hz) seen in EEG recordings from the piriform cortex of awake behaving animals which is further correlated to a rat's sniffing rate (Macrides et al. 1982). The synaptically induced subthreshold oscillations suggested to exist by our model could be used to sensitize the cell to inputs that arrive at the theta or sniffing frequency.

In our single cell simulations, we showed that the synaptically induced subthreshold oscillations in the theta range are generated by voltage-gated conductances. Interestingly, a network model of the piriform cortex developed in our laboratory (Wilson and Bower 1992) whose component pyramidal neurons were incapable of generating voltage-dependent subthreshold oscillations was still able to reproduce realistic EEG patterns, including theta modulation of gamma frequency activity. This suggests that the temporal relationships established by the network architecture are sufficient for generating aggregate activity that occurs on the time scale of the theta/sniffing frequency. An additionally interesting fact about this network model was that it was able to generate realistic EEGs in response to random input. This result showed that network connections alone can account for intrinsic rhythms at which the network operates. The single cell model presented here suggests that individual neurons may display oscillatory behavior that matches network rhythms. A similar phenomenon has been observed in the inferior olive where both neurons and the network are tuned to oscillate at similar frequencies (Lampl and Yarom 1997, Manor et al. 1997). In that case, individual neurons do not display spontaneous oscillations; however, when coupled with other neurons, subthreshold oscillations are generated which help to sustain the network level oscillation (Manor et al. 1997).

3.5.2 Biological plausibility of gamma sequences

The spatio-temporal patterns of synaptic input that are used as input to our model are derived from a systems model (Ketchum and Haberly 1993b) meant to replicate experimental CSD data. These patterns of synaptic activation are therefore biologically plausible in the sense that they were generated in the context of constraints imposed by experimental data. A question arises, however, as to whether or not the gamma sequence taken from the Ketchum-Haberly model is appropriate as input to a single cell. The crux of this question lies in the fact that CSD data comes from field potentials that are a function of a population of neurons rather than a single one. One could argue that such data reflects the "average" activity of a population rather than single neurons; however, oscillatory field potentials suggest a degree of synchrony among neurons (Freeman 1975). Therefore, an equally plausible explanation of the data would be to interpret the CSD data as reflecting many neurons receiving similar spatio-temporal patterns of synaptic input.

A second caveat to consider is that the CSD data was collected from anesthetized animals responding to a shock administered to the LOT (Ketchum and Haberly 1993b, Ketchum and Haberly 1993c). It is difficult to assess a priori how results from anesthetized animals may relate to functioning in awake behaving animals. However, the similarity of the oscillatory field potential elicited by a weak shock to the LOT in anesthetized animals (Ketchum and Haberly 1993c) to the fast oscillations seen in awake behaving animals is at least suggestive that CSD results may apply to the functioning of piriform cortex under more physiological conditions.

3.5.3 Computational utility of gamma sequence structure

A gamma sequence consists of afferent excitation followed by shunting inhibition followed by excitation from association pathways and ending with a late K^+-mediated inhibition. Experimental evidence and simulations suggest that this sequence of events may be stereotyped and underlie the fast (gamma) oscillations seen in olfactory cortex EEGs (Ketchum and Haberly 1993a, Ketchum and Haberly 1993b, Ketchum

and Haberly 1993c). In this chapter we examined some of the consequences of such stimulation on the behavior of a single pyramidal neuron.

One interesting result in this regard was how spike timing during the course of gamma activity reflected the origin of synaptic input that was used to excite the neuron. When afferent or a combination of afferent and associative excitation excited the cell to suprathreshold levels, the neuron generated a single spike at time t. When associative inputs alone were suprathreshold, a spike was generated at time $t + 10$ *msec*. This result suggests that, at least in principle, it is possible to deduce the origin of the synaptic input responsible for generating a spike in the pyramidal cell simply from the timing of the spike.

This idea prompted us to ask if the biological system could make use of such information from the spike timing. First we had to consider this question in the context of multiple gamma sequences. In the real brain, multiple gamma sequences would be occurring at 25 *msec* intervals and this could result in the blurring of associative input from one gamma sequence with afferent input from the next. This would not, however, be the case for the first gamma sequence in a burst sequence where afferent input would be unadulterated by a previous gamma sequence, and associative input, even if it were corrupted by subsequent afferent input, would still represent recurrent input (from cortex to bulb to cortex feedback loop) (Ketchum and Haberly 1993c). Therefore, in theory, this information could be extracted from the first gamma sequence in a theta sequence. The brain could then use the timing of spikes initiated by afferent input in the first gamma sequence as a timing signal indicating the onset of an olfactory stimulus or even a sniff as distinguished from spikes generated by inputs originating from within the network or recurrent activity.

3.5.4 Information processing in the context of a burst sequence

Our simulations showed that individual gamma sequences had an effect on the behavior of the cell that lasted longer than the 25 *msec* interval that separated gamma

sequences during the course of a burst sequence. Therefore, the cell did not reset to a baseline state following each gamma sequence. However, when burst sequences were separated by 650 *msec* or more, the structure of a previous burst sequence had no impact on the subsequent burst sequence. In the biological system, such delays can be accomplished through the slow acting $GABA_B$ inhibition. In this sense, one may imagine that from the perspective of a single cell, burst activity might, when properly spaced, appear packaged and self-contained. On the other hand, the cell is strongly affected by past gamma activity during a burst sequence. In this sense, gamma activity is not self-contained.

Ketchum and Haberly (1993c) showed that only the first oscillatory cycle in the gamma-like activity elicited by a LOT weak shock stimulus is directly evoked by the shock. Further oscillations appeared to be the product of neural circuitry. This would suggest that neural activity during the course of burst activity pertains to neural activity being generated by several different olfactory areas (i.e., olfactory bulb, orbitofrontal cortex, etc.), rather than being directly elicited by the odor stimulus. Only the first gamma oscillation would pertain to activity generated by a direct response to odorants. As previously mentioned, the onset and termination of these bursts is dependent on the passive respiration rate or sniffing duration (Freeman 1960). During passive respiration the slow wave has a frequency of 1-2 Hz (Freeman 1960) which would be sufficient to separate bursts such that activity in one burst would not affect a subsequent burst; however, during sniffing, bursts are spaced more closely (Woolley and Timiras 1965) together suggesting that there would not be a sufficient period of quiescence to erase the effects of a previous burst. Yet it is possible that periods of sniffing may be separated sufficiently to isolate groups of bursts associated with bouts of sniffing. In this way, quiescent periods would be sufficiently long so that pyramidal cells could reset themselves before the next group of sniffs. Pyramidal cells could then process olfactory information associated with one bout of sniffing without being affected by previous bouts of sniffing.

4

Spike Train Coding of Temporally Structured Stimuli

4.1 Abstract

Information theoretic techniques were used to quantify the amount of stimulus information in the spike trains of pyramidal cells from piriform cortex. Stimuli were current injections administered through patch electrodes to the somata of pyramidal cells in a brain slice preparation. All stimuli had the characteristics of Gaussian noise but were differentially bandpass filtered at 0-10 Hz, 4-12 Hz, and 0-40 Hz to approximate (respectively) the temporal structures of pyramidal cell spike rate, the sniffing rate / theta frequency, and a broader band stimulus meant to encompass all frequencies including the EEG gamma rhythm. A DC offset was added to the stimulus to achieve the 1-10 Hz spike rates seen in awake behaving and anesthetized animals. The amount of stimulus information in the spike train can be determined by reconstructing the stimulus and quantitatively comparing the reconstruction to the original stimulus. Our results showed that stimuli in the 0-10 Hz and 4-12 Hz ranges were represented in the neural spike trains twice as well as stimuli in the 0-40 Hz range. Furthermore, the amount of stimulus information in the spike train was highly correlated to the mean firing rate. Finally, we added norepinephrine (NE) to our slices during the course of stimulation to mimic the release of this neuromodulator during arousal. We observed that NE substantially increases the amount of stimulus information in the spike train. Furthermore, we found that the presence of NE does not usually require a change in the linear decoding procedure for spike trains, sug-

gesting that neurons may not have to change their spike train decoding strategy if a presynaptic neuron was modulated by NE.

4.2 Introduction

In the previous chapter, we discussed the response of a realistic model to the types of synaptic input believed to underlie gamma and theta oscillations in the piriform cortex. In this chapter, we explore how well piriform pyramidal cell spike trains encode stimuli with the temporal structure of these oscillations by using information theoretic techniques to quantify the amount of stimulus information contained in spike trains.

Similar techniques have been successfully applied to quantify the amount of information in spike trains from neurons in the blowfly visual system (Bialek et al. 1991), the cricket cercel system (Theunissen et al. 1996), and sensory neurons in the electric fish (Wessel et al. 1996). All of these studies (as well as this one) essentially attempt to reconstruct a known stimulus from neural spike train data. In all past applications of this technique (see Rieke et al., 1997, for extensive review), the stimulus has been a sensory one and the neural spike trains have usually come from sensory neurons (Wessel et al. 1996, Bialek et al. 1991) or neurons that are very close to the periphery (Gabbiani et al. 1996, Roddey and Jacobs 1996, Bialek et al. 1991). The stimulus always consisted of bandlimited Gaussian noise in the particular sensory modality. For example, in the case of the electric fish (Wessel et al. 1996), the stimulus was a fluctuating voltage signal with the characteristics of Gaussian noise bandpassed at 0-200 Hz. Unfortunately, it was not possible for us to use a sensory stimulus in the case of piriform cortex pyramidal neurons because the olfactory stimulus space is too vast (Buck and Axel 1991) and too poorly understood (Cain 1978) for us to sample in the way that is required by the stimulus reconstruction technique. Instead, we used a noisy current injection administered through a patch electrode to the somata of pyramidal cells in a piriform cortex slice. This is not meant to represent a sensory stimulus. Rather, it is meant to approximate the current that would be entering

the soma of the neuron via the dendrites; therefore, our stimuli were bandpassed to reflect the field potential oscillations that are believed to represent synchronous synaptic input to the pyramidal cell dendrites (Freeman 1975, Ketchum and Haberly 1993c).

Additionally, we explore the role of norepinephrine on the information content of pyramidal cell spike trains. NE is a neuromodulator produced in the locus coeruleus by neurons projecting to areas throughout the cerebral cortex (Foote et al. 1983). Behaviorally, NE release has been associated with arousal and attention (Aston-Jones and Bloom 1981, Aston-Jones et al. 1994) and may be present in the piriform cortex during periods of arousal when gamma oscillations are recorded in response to odor stimuli (Freeman 1960). Previous studies have shown that application of NE to cortical pyramidal cells increases the number of action potentials generated in response to constant current pulses (Madison and Nicoll 1982); however, the significance of this increase in the context of spike train information content has never been explored. In this chapter, we elucidate the role of NE in this respect in piriform cortex pyramidal neurons by quantifying changes in the quality of the stimulus representation in the spike train before and after application of NE.

4.3 Methods

A schematic of the methods described in this chapter is displayed in figure 4.1.

Experimental procedures Experiments were performed on slices from four week old female Sprague-Dawley rats. Animals were decapitated under ether anesthesia following procedures approved by the animal care and use committee at Caltech (protocol #1156). Brains were removed and bathed in cooled medium bubbled with 95% O_2 and 5% CO_2 during the slicing procedure. Five coronal sections 400 μm thick were cut starting roughly 0.4 mm caudal to the anterior commissure. Slices were incubated at 35 °C for 35 minutes and then transferred to vials at room temperature. Bathing medium contained (in mM): $NaHCO_3$ 26, $NaCl$ 124, KCl 5, KH_2PO_4 1.2, $CaCl_2$

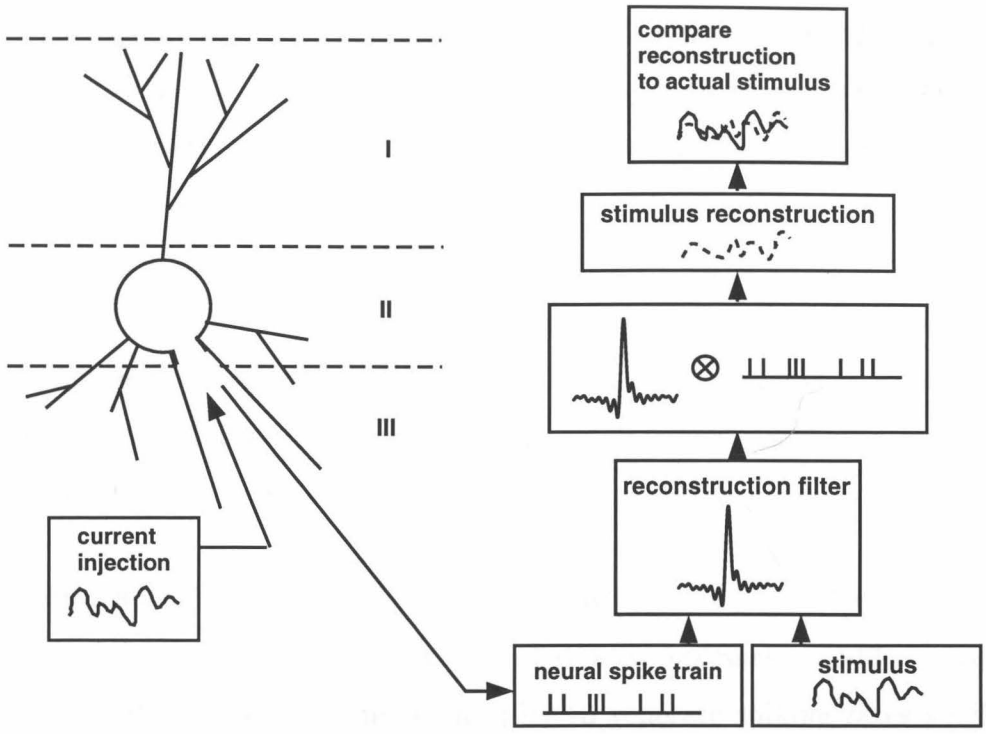

Figure 4.1: Schematic of experimental and data analysis methods used in this chapter.

2.4, $MgSO_4$ 1.3, and dextrose 10. Vials and incubation chamber were bubbled with the gas mixture previously mentioned. To prevent the damaging effects of excitotoxicity, the bathing medium contained 661 μM kynurenic acid; however, kynurenic acid was not present during recordings. During recording procedures the temperature of the slice chamber was maintained at 28.0 to 34.1 °C. Bubbled medium was passed through the chamber at a rate of approximately 3.5 ml/min. Synaptic blockers (in μM: APV 100, CNQX 30, Picrotoxin 50) were present during all recordings in order to minimize noise introduced by random synaptic inputs. Data acquisition and stimulus delivery software was developed in the lab.

Piriform cortex pyramidal cells are easily identified by their somatic position in layer II and their distinctive response to current injection (Haberly 1983, Barkai and Hasselmo 1994). Electrodes were positioned on the somata of pyramidal cells under visual guidance using a Zeiss Axioskop microscope. All recordings were done using the whole-cell technique on cells where seals of at least 10 $G\Omega$ had been achieved. Patch electrodes (impedances: 4-8 $M\Omega$) contained (in mM): potassium gluconate

120, KCl 10, $EGTA$ 10, $HEPES$ 10, $MgCl_2$ 2, $CaCl_2$ 2, and Na_2ATP 2, with pH 7.3 adjusted with KOH and osmolarity 290 $mosm$ (Major et al. 1994). Only cells with resting potentials of -60 mV or less (relative to bath potential) and initial spike heights of at least 80 mV were examined.

Stimuli usually lasted for 30 min, during which time enough spikes could generally be collected to construct adequate Kolmogorov-Wiener (KW) filters that are required for the reconstruction technique. Because we needed long periods of steady firing, concentrations of 10-100 μM NA were used in the data reported here, even though lower concentrations (as low as 1 μM) were able to transiently increase the spike rate.

Stimulus characteristics The calculation of KW filters requires that we use Gaussian noise as our stimulus; however, we found it was necessary to add a small DC current (0.05-0.30 nA) to the stimulus in order to generate spiking rates similar to those seen (roughly 1-10 Hz) in anesthetized and awake-behaving animals (McCollum et al. 1991, Nemitz and Goldberg 1983). This resulted in a net DC membrane potential depolarization of 5 - 34 mV (mean = 14.5 mV) which is similar in magnitude to reported differences in resting membrane potential between neurons from slices and awake animals (Baranyi et al. 1993). This stimulus produced peak to peak fluctuations in membrane potential that had a standard deviation (SD) of 2-9 mV, resulting in stationary spiking frequencies between 1 and 7 Hz. Higher steady state spiking rates could not be attained for the required durations in healthy cells.

Data analysis The Kolmogorov-Wiener (KW) filter (Weiner 1949) guarantees the best linear estimation (in a mean square error sense) of the stimulus. Given the spike train and known stimulus, the KW filter is computed from:

$$h(t) = \int_{-f_c}^{f_c} df \frac{S_{sx}(-f)}{S_{xx}(f)} e^{-i2\pi ft}, \tag{4.1}$$

where f_c is the cutoff frequency of the stimulus, S_{sx} is the Fourier transform of the cross-correlation of the stimulus and spike train, and S_{xx} is the Fourier transform of the autocorrelation of the spike train. When $h(t)$ is convolved with the neural spike

train, an estimate of the stimulus (s_{est}) is obtained. To quantify the quality of the reconstruction, the noise is first defined

$$n(t) = s_{est}(t) - s(t), \tag{4.2}$$

where $s(t)$ represents the actual stimulus. The total energy in the stimulus is represented by

$$\sigma^2 = \int_{-f_c}^{f_c} df S_{ss}(f), \tag{4.3}$$

where S_{ss} is the power spectrum of the stimulus. The mean square error of the reconstruction can be calculated from

$$\epsilon^2 = \int_{-f_c}^{f_c} df S_{nn}(f), \tag{4.4}$$

where S_{nn} is the power spectrum of the noise. A normalized measure of the quality of the reconstruction comes from the coding fraction(γ) (Gabbiani and Koch 1996)

$$\gamma = 1 - \frac{\epsilon}{\sigma} \tag{4.5}$$

When the reconstruction is identical to the stimulus $\gamma = 1$, and when it is no better than chance (i.e., compared to a random signal), $\gamma = 0$.

Finally, to measure the mutual information (between the stimulus and spike train) per unit time, the following expression is used (Wessel et al. 1996):

$$I_t = \frac{-f_c}{log(2)} log\left(\frac{\epsilon}{\sigma}\right) \tag{4.6}$$

where I_t is in units of $bits/sec$. The coding efficiency, I_s, which represents the amount of stimulus information per spike is obtanied by dividing I_t by the mean firing rate.

A detailed explanation of these techniques and their applications can be found in reference (Rieke et al. 1997).

All data analysis and stimulus construction were done using MATLAB (Mathworks, Natick, MA).

4.4 Results

4.4.1 Suitability and stability of KW filters

Stimulus reconstructions accomplished using KW filters require that a system be time-invariant. In the case of a neuron, this means that a neuron's response to input must be consistent over the time during which spike train data is collected for use in constructing a KW filter. To measure constancy of response, we interspersed stimulus repeats that were 10 *sec* in duration among 10 *sec* segments that were all different from each other. The repeats were then used to generate a raster plot which indicated that the 10 *sec* period was more than ample time for the neuron to respond to the repeated stimulus without being affected by the previous 10 *sec* of novel stimulation. If the spike trains elicited by the repeated stimulus over time were constant, then the neuron's response was considered time-invariant. Once periods of time-invariance were established, only spike train data from those periods were used to calculate KW filters. Furthermore only a single repeat and all of the novel segments were used to construct KW filters since this technique requires the use of a non-repeating stimulus. Because we found that periods of time-invariance in the response properties of neurons tended to always correlate with steady firing rates over time, we sometimes calculated KW filters from stimuli that were non-repeating but showed steady firing rates through their entire duration. The results of these experiments were not distinguishable as a class from those experiments that were done with the periodic stimulus repeats included.

The results of our test for time-invariance for a typical pyramidal cell are shown in figure 4.2. The number of spikes generated in response to the repeated stimulus decreases over the course of one minute and then remains constant for the remaining 19 minutes of the stimulation period which gives us an adequate number of spikes for construction of our KW filter (more on this below). Interestingly, the adaptation process involves a decrease in the number of spikes elicited by the repeated stimulus; however, the spikes that remain occur at similar temporal positions with regard to spikes that had occurred before adaptation. In this sense the spike trains generated

in the adapted neuron simply resemble sparser responses to the stimulus than before adaptation took place. Neurons in the rest of our sample showed the same type of response with periods of adaptation lasting from 20 to 320 *sec* (mean = 70 *sec*, n = 10).

Although most spike coding studies to date (Rieke et al. 1997) have found that a linear decoding strategy has been successful in extracting information from a spike train, there is no reason to assume that a neuron's spike train will be amenable to a linear decoding strategy. In generating stimulus reconstructions with KW filters, one is treating each spike in the same way (i.e., convolving each spike with the same filter) and ignoring any information that might be contained in the second order statistics of the spike train. One can test for the quality of the linear reconstruction by plotting the stimulus values conditional on the values of the reconstruction. If this relationship is linear, then this indicates that nonlinear terms would not significantly improve the quality of the reconstruction. Deviations from a straight line, however, would suggest that nonlinear terms may significantly improve the decoding process. Figure 4.3 shows the results of such an analysis for neurons that were stimulated with stimuli that were bandpassed at 0-10 *Hz*, 4-12 *Hz*, and 0-40 *Hz*. A linear relationship between the values of the stimulus reconstruction and the actual stimulus is seen in each case with deviations from linearity occurring in the data from neurons stimulated with 0-10 *Hz* and 4-12 *Hz* stimuli at extreme values of the stimulus reconstruction. To assess the possible impact of these deviations on the quality of our reconstruction, we compared the number of points in the stimulus that fall into the nonlinear range of the plot to the total number of points in the stimulus. We found that these points generally accounted for less than 10% of the total number of stimulus points, suggesting that even in the case where a nonlinear decoding strategy could improve the reconstruction quality, the improvement would not be significant. Examples of this analysis are shown in figure 4.3 where points in the nonlinear region of the stimulus estimate vs. stimulus plots account for no more than 4% of the stimulus values.

The final issue we must address in order to be confident of any results gleaned from our reconstructions is the stability of our KW filters. If the number of spikes

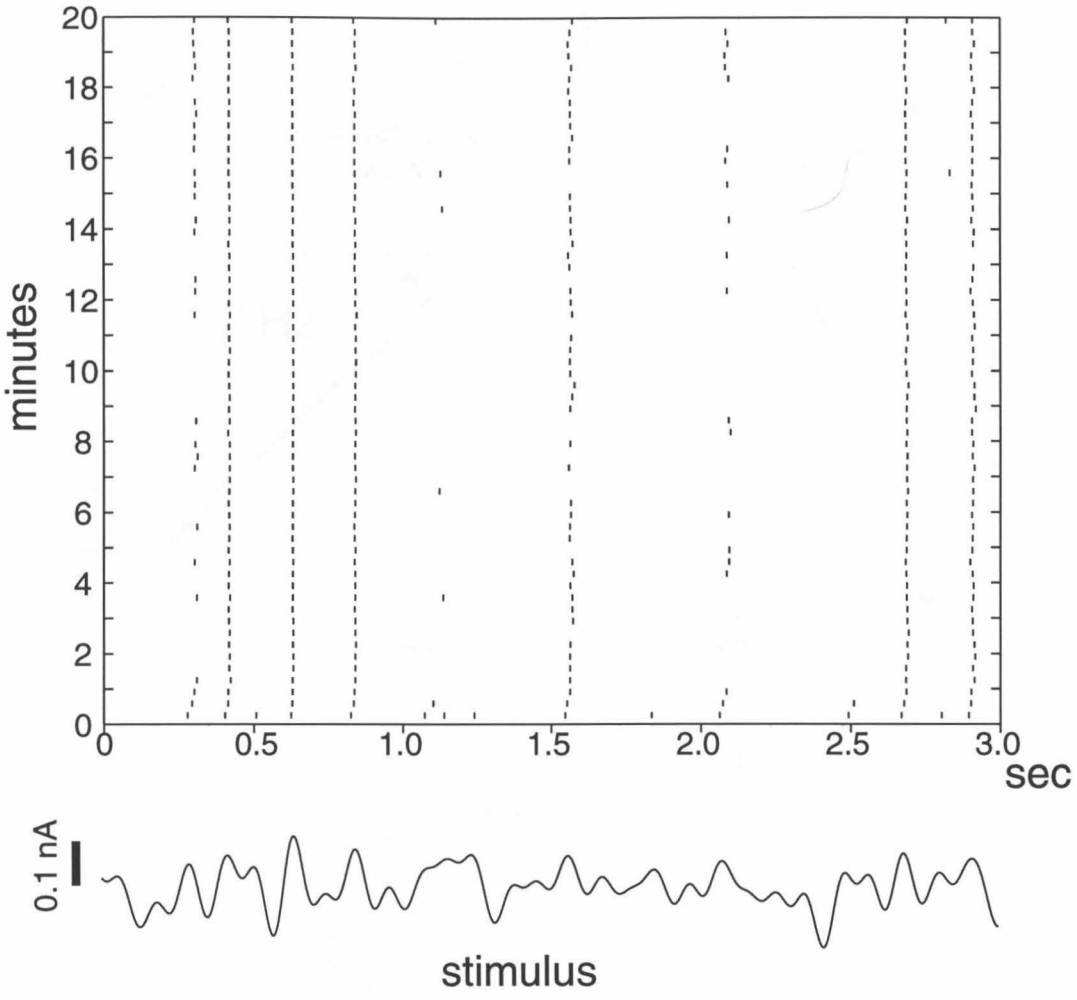

Figure 4.2: Raster plot illustrating pyramidal cell spike trains in response to the repeated current injection waveform shown at the bottom. Following an initial period of adaptation lasting approximately 60 *sec*, the neuron displays an invariant response to the repeated stimulus for the remaining 19 *min* of the recording duration. Only spike train data from such periods of time-invariance in the neural response can be used to calculate KW filters.

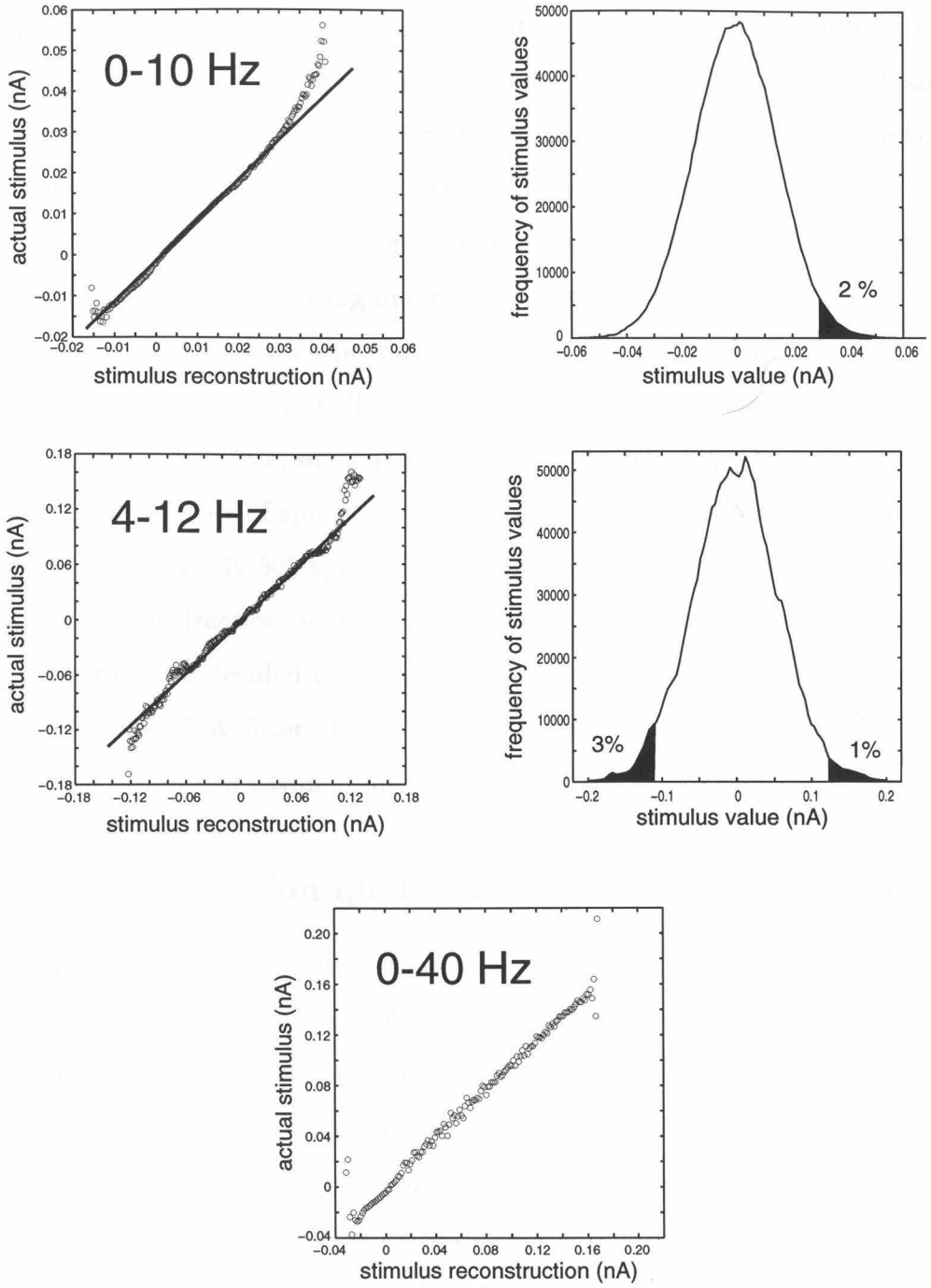

Figure 4.3: The appropriateness of a linear decoding method can be determined by plotting values of the known stimulus conditional on values in the stimulus reconstruction. Consistent deviations from linearity would suggest that nonlinear terms might improve the quality of the stimulus reconstruction. Two of the examples shown here show deviations from linearity; however, stimulus values in the range of deviation constitute a very small portion of the stimulus values as illustrated by the stimulus value histograms in the column on the right. Shaded regions in the histogram represent the stimulus values in the nonlinear portions of the plots on the left. Percentages represent the portion of the values in the nonlinear range compared to the total number of stimulus values.

in the spike train used to construct the KW filter is too small, then the filter can be biased to reflect features of the stimulus that underlie that particular spike train and will not have general applicability to decoding spikes that might occur in the context of a different stimulus. In order to determine the requisite number of spikes needed for a high quality KW filter, we first generated a series of filters calculated from spike trains that contained an increasing number of spikes. These filters were then used to reconstruct the stimulus from a portion of the spike train that had not been used in the calculation of the KW filter. The coding fraction of the reconstruction was then compared to the coding fraction achieved by using the KW filter that was calculated with the highest number of spikes from the sample. This data for five different cells is shown in figure 4.4. By 500 spikes the average coding fraction achieved is 95% the value of the coding fraction achieved with the highest number of spikes from each sample; therefore, we decided that a minimum sample of 500 spikes is sufficient for calculating a stable KW filter. KW filters for the neurons described in this chapter were calculated from spike trains that contained 502-11,806 spikes.

4.4.2 Reconstruction quality and stimulus characteristics

Because the KW filter essentially reflects the stimulus features that occur around an action potential, its structure is highly dependent on the frequency characteristics of the stimulus and the active and passive properties of the neuron. Therefore, one would ideally want to use a stimulus that is similar to the somatic currents that the piriform pyramidal cell experiences during awake-behavior. Studies in other systems have shown that reconstructions can be dramatically improved when using biologically relevant stimuli (Rieke et al. 1995). Unfortunately, such data is not available for piriform cortex. Instead we have chosen to bandpass our stimuli to reflect EEG rhythms which are believed to reflect synchronized synaptic input to the pyramidal cell. Stimuli bandpassed at 0-10 Hz were meant to reflect the spiking rate that is seen in piriform cortex pyramidal cells responding to odor stimuli (Nemitz and Goldberg 1983). Those bandpassed at 4-12 Hz were meant to approximate the theta

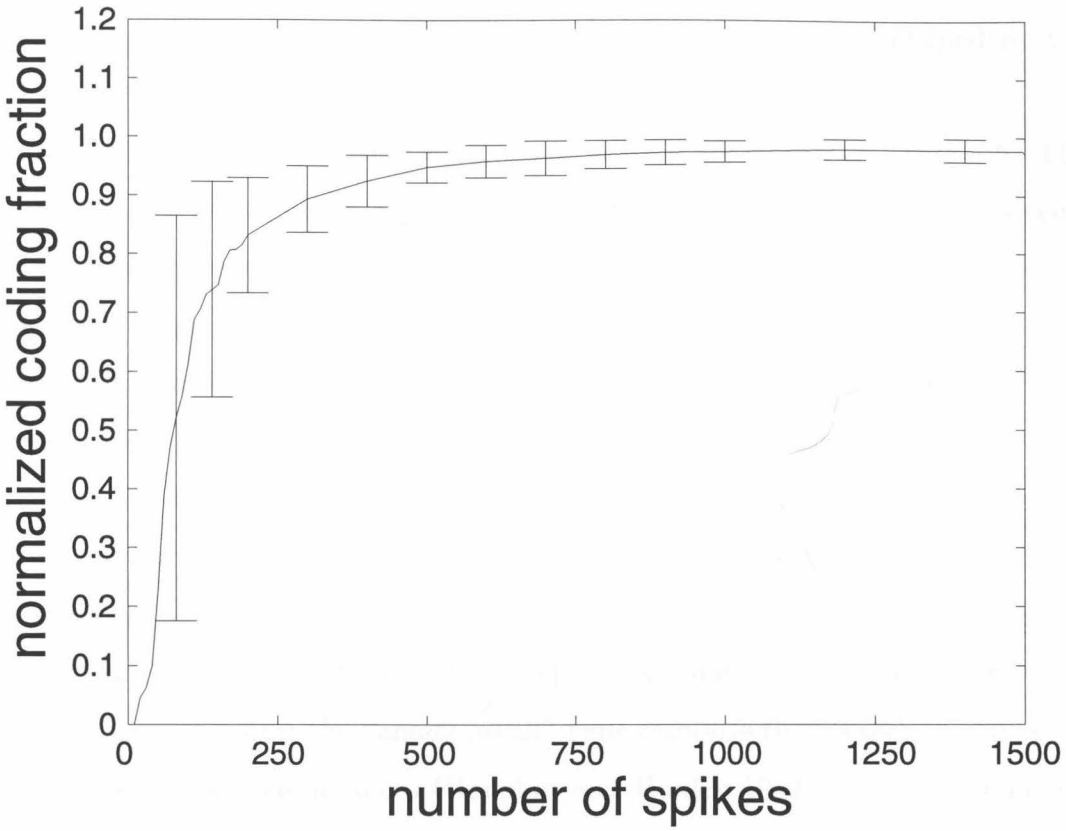

Figure 4.4: Plot of the number of spikes in the data used to calculate KW filters vs. the quality of the reconstruction achieved with those filters. A 60 *sec* portion of the spike train that is not contained in the data set used to calculate the filters is reconstructed and its coding fraction is measured. The quality of the filter (shown on y-axis) is measured by dividing the coding fraction achieved with a filter utilizing data consisting of n (shown on x-axis) spikes by the coding fraction achieved with the maximum number of spikes recorded in each trial (range: 1800 to 7000).

rhythm seen in the cortical EEG during sniffing and exploratory behavior (Woolley and Timiras 1965, Macrides et al. 1982, Ranck 1973). Stimuli with frequencies of 0-40 Hz were meant to encompass the spectral range of the respiratory waves (1-2 Hz), theta rhythm (4-12 Hz), and gamma rhythm (roughly 40 Hz) that are recorded from piriform cortex in awake-behaving animals (Woolley and Timiras 1965, Freeman 1960). The wide frequency range of these stimuli was also meant to account for the dendritic filtering effects that are likely to play a role as synaptic input makes its way from the dendrite to the soma (Rall 1989). A stimulus that was bandpassed at 0-400 Hz was used to generate a filter that was not limited by the bandwidth of

the stimulus. This was done primarily to generate a filter that was shaped by the properties of the neuron rather than the stimulus.

The KW filters calculated from each of our stimuli are shown in figure 4.5. The zero point in the filter graphs represents the time at which a spike would occur. Negative times represent the stimulus features that tend to precede a spike while positive times represent stimulus features that tend to follow a spike. A typical filter resulting from the 0-10 Hz stimulus shows a positive peak at the zero point that is preceded by a strongly negative peak. The amplitude of the positive peak is a reflection of the level current injection required to elicit a spike while the width of the peak appears to reflect the bandwidth of the stimulus. The width of the negative peak also appears to be bandlimited in this respect. The negative peak is not repeated at positive times suggesting that a more hyperpolarizing current tends to precede spikes. It is likely to reflect the "anode-break" type response that is seen in cells with Hodgkin-Huxley type conductances (Hodgkin and Huxley 1952). This phenomenon involves the generation of a spike following a hyperpolarization and subsequent return to resting potential. In the Hodgkin-Huxley model, the physiological mechanism governing this is a deinactivation of the Na^+ channel (Hodgkin and Huxley 1952).

Interestingly, when a 4-12 Hz stimulus is used, the filter appears to be symmetric. Although negative peaks precede and follow the zero point, it is difficult to ascribe a physiological meaning to them. Since a spike that would occur at the zero point would only be dependent on the stimulus that precedes it and the positive peak in this filter is surrounded by two negative peaks that are approximately equal in amplitude, it is likely that the negative peaks are a reflection of the stimulus rather than a neuronal property. Because the 4-12 Hz stimulus has a narrower bandwidth than other stimuli used here, any positive peak in the stimulus will more likely be preceded and followed by a negative peak. As an example of this, consider a stimulus that contains a single frequency (very narrow bandwidth). In this case any positive peak will always be surrounded by negative peaks.

The 0-40 Hz stimulus generates an asymmetrical filter resembling the 0-10 Hz filter. The primary difference between the two is that the negative peak does not

appear bandlimited by the stimulus as in the case of the 0-10 Hz stimulus, while the positive peak is bandlimited as in the previous case. Finally, the 0-400 Hz filter is similar to the 0-40 Hz stimulus except that the negative peak is absent and the positive peak is no longer bandlimited.

As a final assessment of the filters and the stimuli used to calculate them, we compared the coding fractions and coding efficiencies achieved by each one. One important caveat to consider in interpreting these results is that we were unable achieve prolonged spike rates that were higher than roughly 7 Hz. Although higher spike rates could be achieved transiently for periods of up to one minute, the cell quickly adapted, and in cases where a DC offset was added to compensate for this adaptation, the cell became sick and often ceased to fire altogether. Therefore, regardless of the stimulus characteristics, spike rates were always less than 8 Hz.

Table 4.1 shows the coding fractions, γ, the amount of stimulus information, I_t, and the coding efficiencies, I_s, achieved for different stimuli. Recall that coding fraction is a measure of the quality of the stimulus reconstruction while stimulus information represents an absolute measure in $bits/sec$ of the amount of information about the stimulus that is conveyed per unit time in the spike train. The highest coding fractions (γ values of 0.33 and 0.38) were achieved with stimuli that were bandpassed at 4-12 Hz stimuli. Cells that were stimulated with the 0-10 Hz stimulus also showed relatively high coding fractions with values of 0.14-0.30 (mean = 0.24, n = 8). In contrast, results using the 0-40 Hz stimulus never showed coding fractions greater than 0.16 (min = 0.08, mean = 0.12, n = 5) despite the fact that spiking rates for these trials (mean = 5.2 Hz) were higher than those for trials using the 0-10 Hz and 4-12 Hz stimuli (mean spike rates of 3.3 Hz and 3.5 Hz respectively). Results from the 0-400 Hz stimulus produced a negligible coding fraction (0.0037) and, for that reason, we chose to only use this stimulus once.

While coding fractions achieved with the 0-40 Hz stimulus were on average substantially lower than those obtained by using lower frequency stimuli, the amount of stimulus information shows an opposite trend with spike trains generated by the 0-40 Hz showing higher levels of stimulus information than those generated by the 0-10

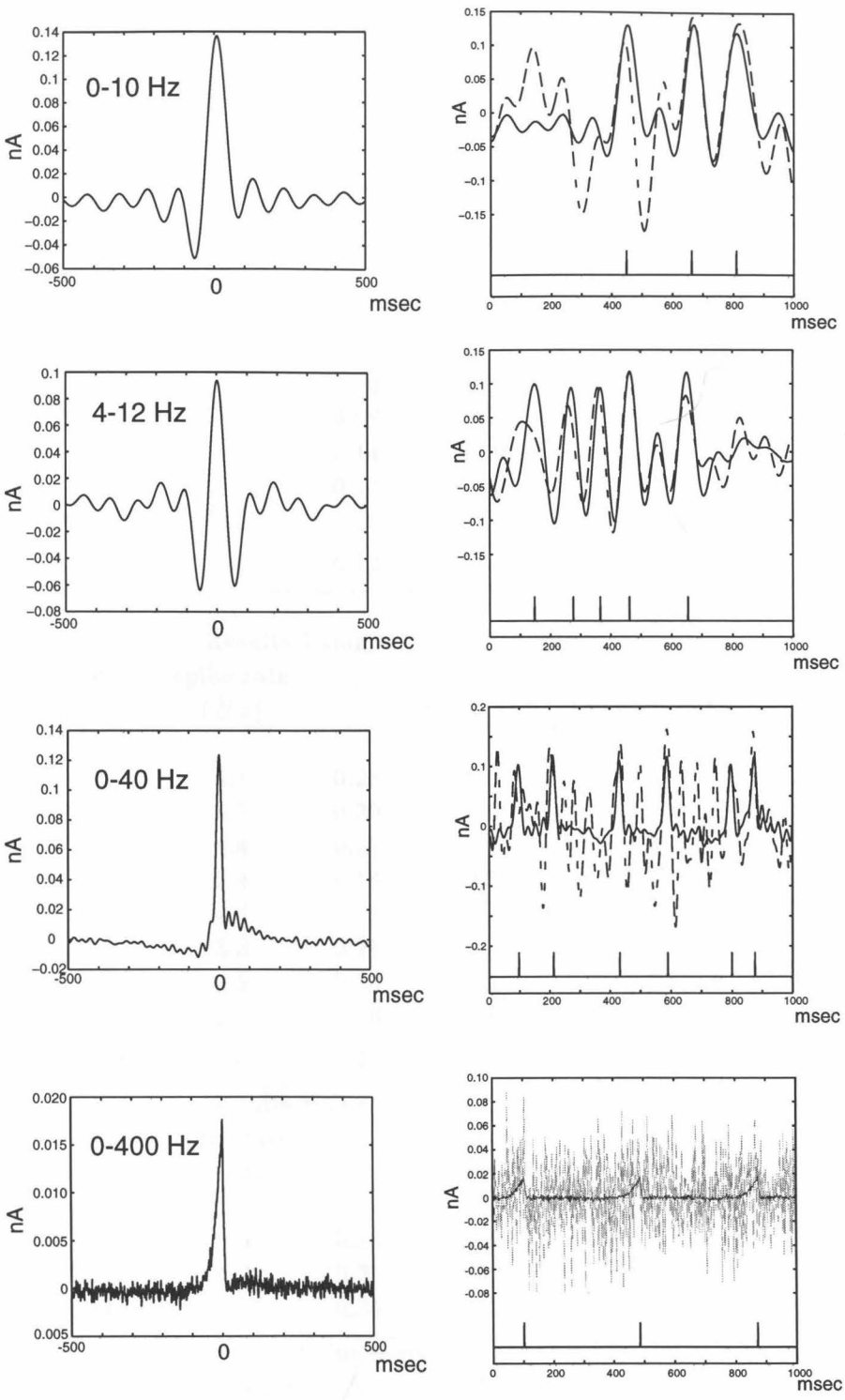

Figure 4.5: Comparison of KW filters and reconstructions achieved with different stimuli. Filters and bandwidth of stimuli are shown in the left column. Spike trains on the right are convolved with KW filters on the left to obtain a stimulus reconstruction (solid line) to be compared to the actual stimulus (dotted line). Negative times in filter graphs show the structure of the stimulus that tends to precede the occurrence of a spike, while positive times show the structure of the stimulus that tends to follow a spike. DC offset is subtracted from all reconstruction graphs.

Table 4.1: Coding Statistics for Different Stimuli

Results Using 0-40 Hz Stimulus				
cell	spike rate (Hz)	γ	I_t $(bits/sec)$	I_s $(bits/spike)$
A	2.6	0.10	6.8	2.6
B	2.8	0.08	8.7	3.1
C	6.5	0.14	11.0	1.7
D	6.6	0.14	11.9	1.8
E	7.6	0.16	11.4	1.5
mean	5.2	0.12	10.0	2.1

Results Using 0-10 Hz Stimulus				
cell	spike rate (Hz)	γ	I_t $(bits/sec)$	I_s $(bits/spike)$
F	4.1	0.28	6.6	1.6
G	4.1	0.30	6.6	1.6
H	4.4	0.26	5.7	1.3
I	2.4	0.14	2.5	1.1
J	4.4	0.29	6.4	1.5
K	3.3	0.28	5.9	1.8
L	2.5	0.20	4.1	1.7
M	1.5	0.16	2.8	1.9
mean	3.3	0.24	5.1	1.6

Results Using 4-12 Hz Stimulus				
cell	spike rate (Hz)	γ	I_t $(bits/sec)$	I_s $(bits/spike)$
N	2.9	0.33	6.8	2.2
O	4.2	0.38	8.0	1.9
mean	3.5	0.35	7.4	2.0

Results Using 0-400 Hz Stimulus				
cell	spike rate (Hz)	γ	I_t $(bits/sec)$	I_s $(bits/spike)$
P	1.6	0.0037	2.1	1.3

Hz and 4-12 Hz stimuli (see table 4.1 for comparison). This difference can be accounted for by the fact that higher bandwidth stimuli contain more information than those with lower bandwidth; therefore, a spike train will have to contain a greater amount of information to represent a higher bandwidth stimulus. This is illustrated by results showing that spike trains generated by 0-40 Hz stimuli that on average contained 10.0 $bits/sec$ of stimulus information could only produce stimulus estimates that had a mean coding fraction of 0.12, while a mean stimulus information level of 5.1 $bits/sec$ in the case of the 0-10 Hz stimuli resulted in an average coding fraction of 0.24.

Although the type of stimulus we used had an effect on the coding fraction we could achieve with our reconstructions, when the stimulus type was kept constant, the quality of the reconstruction appeared to be highly correlated with the mean spike rate. For example, we calculated correlation coefficients for spike rate and coding fraction for neurons that were stimulated with stimuli that were bandpassed at 0-10 Hz and 0-40 Hz and obtained values of 0.88 and 0.97 respectively.

A summary of coding efficiency results is shown in table 4.1. In contrast to the coding fraction results, the 0-40 Hz stimulus produced the highest coding efficiency (max $I_s = 3.1$ $bits/spike$, mean $I_s = 2.1$ $bits/spike$); however, the range of coding efficiencies for these neurons overlapped with those where stimuli in the 0-10 Hz and 4-12 Hz range were used.

4.4.3 Effects of norepinephrine

Norepinephrine (NE) is generally believed to be released into the cortex by the locus coereleus during periods of arousal (Aston-Jones et al. 1994). The locus coereleus makes extensive projections to the piriform cortex (Foote et al. 1983) and recent studies (Vanier and Bower 1993, Hasselmo et al. 1997) have shown NE to affect the synaptic efficacy of different pathways in piriform cortex. Furthermore, studies in hippocampal pyramidal cells have shown that NE can greatly increase a neuron's excitability independent of synaptic effects (Madison and Nicoll 1982). To explore

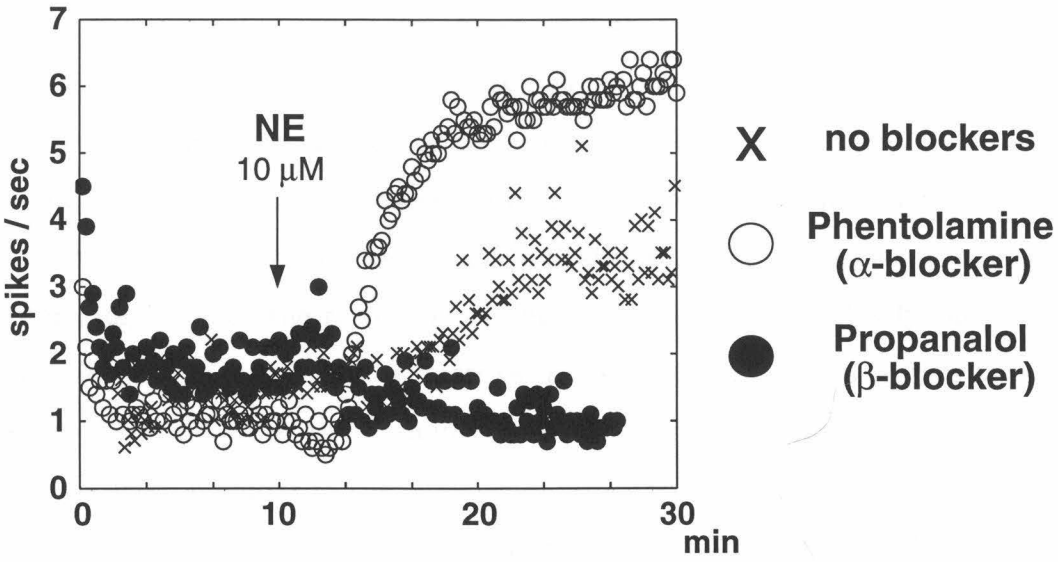

Figure 4.6: Effects of propanolol (β - adrenergic receptor blocker) and phentolamine (α - adrenergic receptor blocker) on NE's ability to increase firing rate during the course of a stimulus. Phentolamine (10 μM) does not appear to diminish the NE-induced increase in firing rate, while propanolol (10 μM) causes a slight decrease in firing rate following application of NE. These results suggest that NE-induced increases in firing rate are mediated by the β - adrenergic receptor. Data comes from three different pyramidal cells.

the way in which NE might affect spike coding in piriform cortex pyramidal cells, we performed the information theoretic analysis described above using spike trains that were generated in the presence and absence of NE.

The stimuli used for these experiments were bandpassed at 0-10 Hz and 4-12 Hz since the results described above had indicated that pyramidal cell spike trains represent higher frequency stimuli significantly worse than low frequency stimuli. When NE was added to the bath during the course of stimulation, it always (n = 20) increased the mean firing rate of the neuron. NE-induced increases in spike rate were diminished or altogether eliminated by the presence of the β-adrenergic antagonist propanolol (n = 5), but not by phentolamine (n = 5), an α-adrenergic antagonist. These pharmacological data are illustrated in figure 4.6. NE-induced excitability in hippocampal pyramidal cells has been shown to be mediated by β-adrenergic receptors as well (Madison and Nicoll 1986a, Madison and Nicoll 1986b).

As with previous data, we used stimulus repeats in order to assess the time-

invariance of the neuron's response. Figure 4.7 shows a raster plot of spike trains generated in response to stimulus repeats before and after the addition of NE. As can be clearly seen, there appear to be two periods of stable response, one in the absence of NE and one in the presence of it. Data from each of these periods is used to generate KW filters for the reconstruction of stimuli in the presence and absence of NE. Interestingly, when the raster data in figure 4.7 is examined closely, one notices that addition of NE results in an increase in the total number of spikes that are elicited by the stimulus while retaining the number and temporal position of spikes that had occurred previous to the addition of NE. Also, the bottom row in the raster plot representing the neuron's response prior to adaptation is identical to the rows showing the neural response after the addition of NE.

NE-induced changes in spike coding were measured by comparing coding fraction and coding efficiency for stimulus repeats and non-repeats before and after the addition of NE. An example of such data for a typical cell is shown in figure 4.8. As the figure illustrates, NE causes an increase in mean firing rate while increasing the coding fraction and decreasing coding efficiency.

To assess the effect NE had on stimulus information content in the spike train, we calculated changes in γ, I_t, and I_s. In every case examined ($n = 6$) the presence of NE increased the coding fraction (on average from 0.27 to 0.33 for non-repeats and 0.25 to 0.32 for repeats), suggesting that NE acts to improve the stimulus representation in the spike train. An example of this for one cell is shown in figure 4.8. Increases in coding fraction for all cells ranged from 17% to 89% for reconstructions of stimulus repeats and 10% to 72% for reconstructions of non-repeats. Likewise, stimulus information shows increases 19% to 118% for repeats and 6% to 110% for non-repeats. See table 4.2 for measurements regarding coding fraction and stimulus information. In the cases where changes in coding efficiency were statistically significant (n = 5/6, p < 0.05, Student's t-test), decreases of 13-21% for repeats and 11-33% for non-repeats were observed. Table 4.3 contains coding efficiency data for all neurons.

To understand how NE increases the coding fraction, we compared reconstructions of repeats that were accomplished in the absence and presence of NE. As figure 4.9

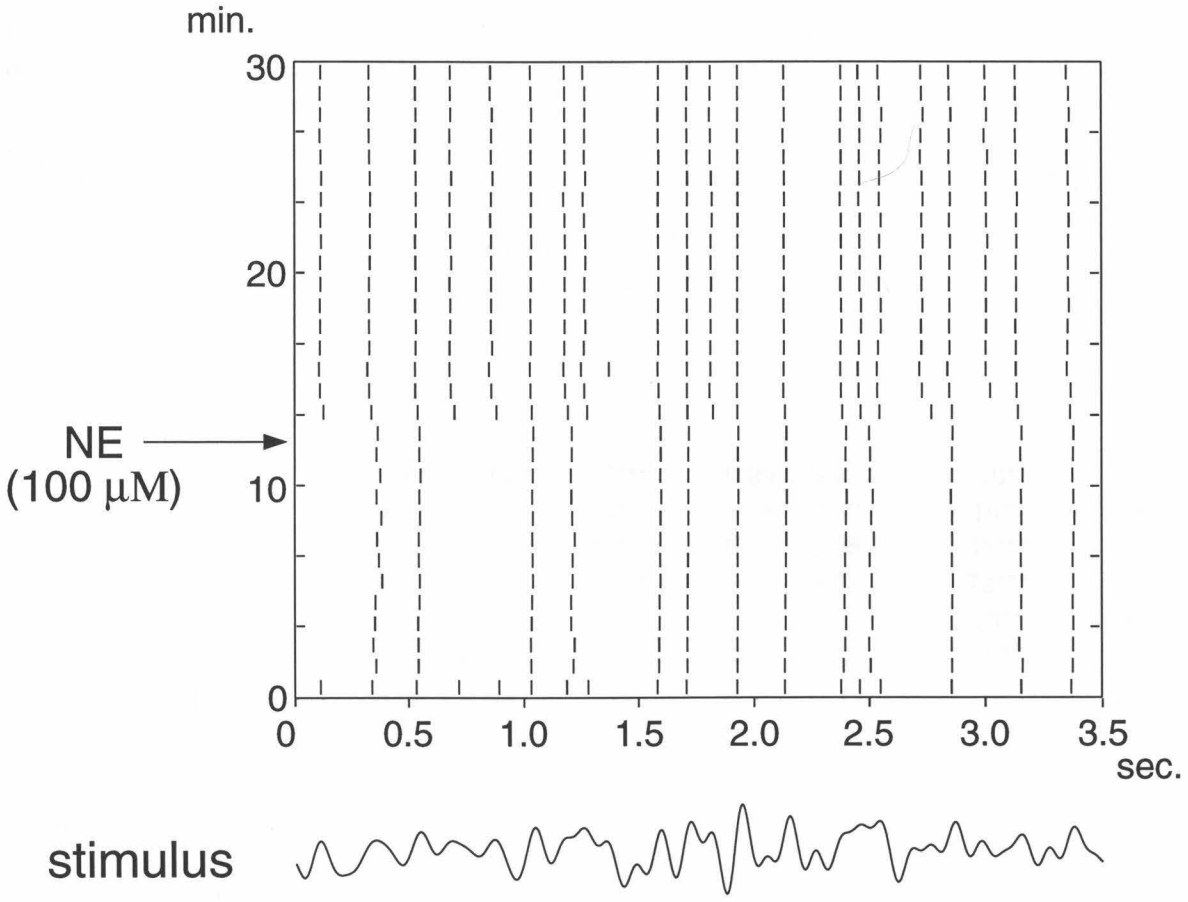

Figure 4.7: Raster plot showing spike trains over time in response to a repeated stimulus. The spikes that were present prior to the addition of NE continue to be present following the application of the drug; however, the total number of spikes increases. The raster plot shows two clear regions of steady state neural response that are demarcated by the application of NE. Data from these regions is used to calculate two separate KW filters, one to decode spike trains recorded in the absence of NE and one to decode them in the presence of NE.

Table 4.2: Effect of NE on stimulus representation. Δe signifies changes in the neuron's encoding properties following the addition of NE. This measure is explained in the text. Level of statistical significance is indicated by asterisks: one asterisk ($p < 0.05$), two asterisks ($p < 0.005$), three asterisks ($p < 0.0001$). Values in italics indicate statistical insignificance ($p > 0.05$). Statistical significance is assessed using *Student's t-test* in all cases. Cells J-M were stimulated with current injection waveforms that were bandpass filtered at 0-10 Hz. Stimuli for cells N and O were filtered at 4-12 Hz.

		Coding Fraction				
cell	spike rate pre- / post-NE (Hz)	$\gamma_{pre-}/\gamma_{post-NE}$ repeats	$\Delta\gamma$ repeats (%)	$\gamma_{pre-}/\gamma_{post-NE}$ non-repeats	$\Delta\gamma$ non-repeats (%)	Δe (%)
J	4.4 / 6.3	0.30 / 0.35	17***	0.29 / 0.32	10*	4
K	3.3 / 5.9	0.25 / 0.37	45***	0.28 / 0.33	16**	18
L	2.5 / 4.7	0.21 / 0.26	26***	0.20 / 0.28	36***	2
M	1.5 / 3.5	0.13 / 0.25	89***	0.16 / 0.28	72***	6
N	2.9 / 3.9	0.27 / 0.32	18***	0.33 / 0.37	13**	1
O	4.2 / 6.9	0.32 / 0.40	27***	0.38 / 0.42	10**	22
mean	3.1 / 5.2	0.25 / 0.32	37	0.27 / 0.33	27	8.8

		Stimulus Information			
cell	spike rate pre- / post-NE (Hz)	$I_{t,pre-}/I_{t,post-NE}$ repeats ($bits/sec$)	ΔI_t repeats (%)	$I_{t,pre-}/I_{t,post-NE}$ non-repeats ($bits/sec$)	ΔI_t non-repeats (%)
J	4.4 / 6.3	6.3 / 8.3	32***	6.4 / 6.8	*6*
K	3.3 / 5.9	5.1 / 8.3	63***	5.9 / 7.1	20**
L	2.5 / 4.7	4.2 / 5.3	26***	4.1 / 5.8	41***
M	1.5 / 3.5	2.2 / 4.8	118***	3.0 / 6.3	110***
N	2.9 / 3.9	5.7 / 6.8	19***	6.8 / 8.2	21**
O	4.2 / 6.9	6.4 / 9.0	41***	8.2 / 9.7	18**
mean	3.1 / 5.2	5.0 / 7.1	50	5.7 / 7.3	36

Table 4.3: Effect of NE on coding efficiency. See previous table caption for an explanation of asterisks.

	Coding Efficiency			
cell	$I_{s,pre-}/I_{s,post-NE}$ repeats (*bits/spike*)	ΔI_s repeats (%)	$I_{s,pre-}/I_{s,post-NE}$ non-repeats (*bits/spike*)	ΔI_s non-repeats (%)
J	1.4 / 1.3	-13^{***}	1.5 / 1.1	-24^{***}
K	1.6 / 1.4	-13^{***}	1.8 / 1.2	-33^{***}
L	1.6 / 1.1	-30^{***}	1.7 / 1.3	-24^{***}
M	1.5 / 1.5	*-1*	1.9 / 1.7	-13^{*}
N	2.1 / 1.8	-13^{***}	2.2 / 2.0	-11^{*}
O	1.6 / 1.3	-21^{***}	1.9 / 1.4	-29^{***}
mean	1.6 / 1.4	-15	1.8 / 1.4	-22

illustrates, NE does not appear to significantly change the structure of the KW filter. Instead it improves reconstruction quality by increasing the number of spikes elicited by the stimulus. Since each spike is convolved with a KW filter, the greater number of spikes elicited by NE essentially represents a greater sampling of the stimulus by the neuron. In fact, we found that we could mimic the effects of NE by increasing the DC offset in our current injection during the course of stimulation. When this was done we were able to increase a neuron's firing rate from 2.8 to 6.2 Hz which was accompanied by an increase in coding fraction from 0.24 to 0.38.

Although our analysis had suggested that changes in coding fraction were accomplished mainly through an increase in spike rate, we wanted to quantify differences between KW filters since these differences would imply differences in the way a spike must be decoded to extract stimulus information. Because the shape of the KW filter is partially shaped by the active properties of the neuron and NE is known to strongly diminish a potassium current in piriform pyramidal cells (Constanti and Sim 1987a), we expected a change in the structure of the KW filter after the application of NE. However, when filters generated in the presence and absence of NE were used to reconstruct the stimulus from spike trains recorded in the presence of NE, few differences between the reconstructions could be seen (figure 4.10). Interestingly, the

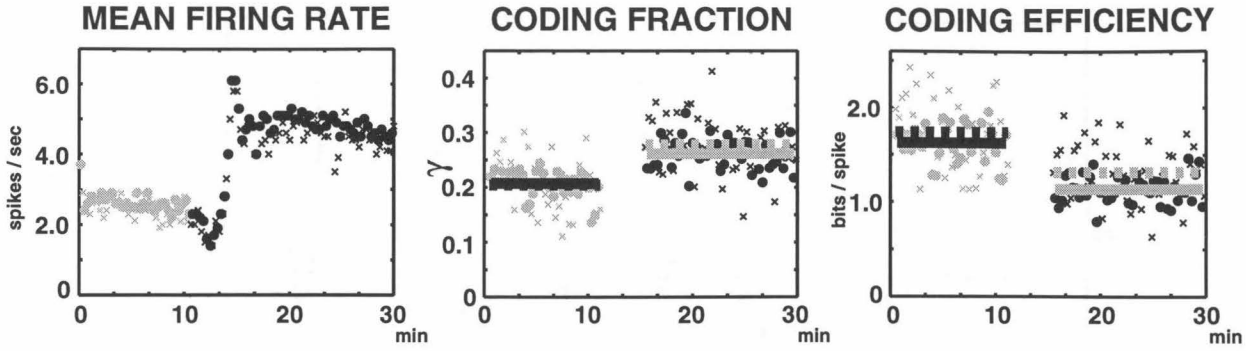

Figure 4.8: Changes in coding statistics in response to the application of NE. Application of NE appears to increase the spike rate and coding fraction while decreasing the coding efficiency for this particular cell. Data for non-repeats are indicated by the x's. Data for repeats are shown by the circles. Gray circles and x's represent data recorded prior to the application of NE, while black data points represent data recorded after the application of NE. The solid lines represent means for stimulus repeat data while the dashed lines represent means for stimulus non-repeats data. Shading of the lines is done for purely illustrative purposes. Lines correspond to data points on which they are superimposed.

only consistent change in the filter structure caused by NE was a reduction in the positive peak amplitude which presumably reflects a decrease in the amount of current injection required for the neuron to reach threshold. This result is consistent with the finding that NE reduces a very slow potassium current (see KAHP in chapter 2) which has a time to peak of approximately 1 *sec* and is believed to be involved in regulating adaptation in this class of neurons (Constanti and Sim 1987a). Presumably, the reduction of this current would increase the excitability of this neuron and this would be reflected in the smaller peak in the NE filter when compared to the non-NE filter. Because this membrane current is so slow it would not tend to play a significant role in structuring the width of our filters given the frequency range of our stimuli.

To quantify the similarity between filters, we first convolved a filter, $h(t)$, calculated from data in the absence of NE with a spike train, $\{t_i\}_{NE}$, generated in the presence of NE and calculated the mean coding fraction, $\gamma(h(t), \{t_i\}_{NE})$, for the resulting stimulus reconstruction. This was then compared to $\gamma(h(t)_{NE}, \{t_i\}_{NE})$, the mean coding fraction achieved by a stimulus reconstruction using the NE filter,

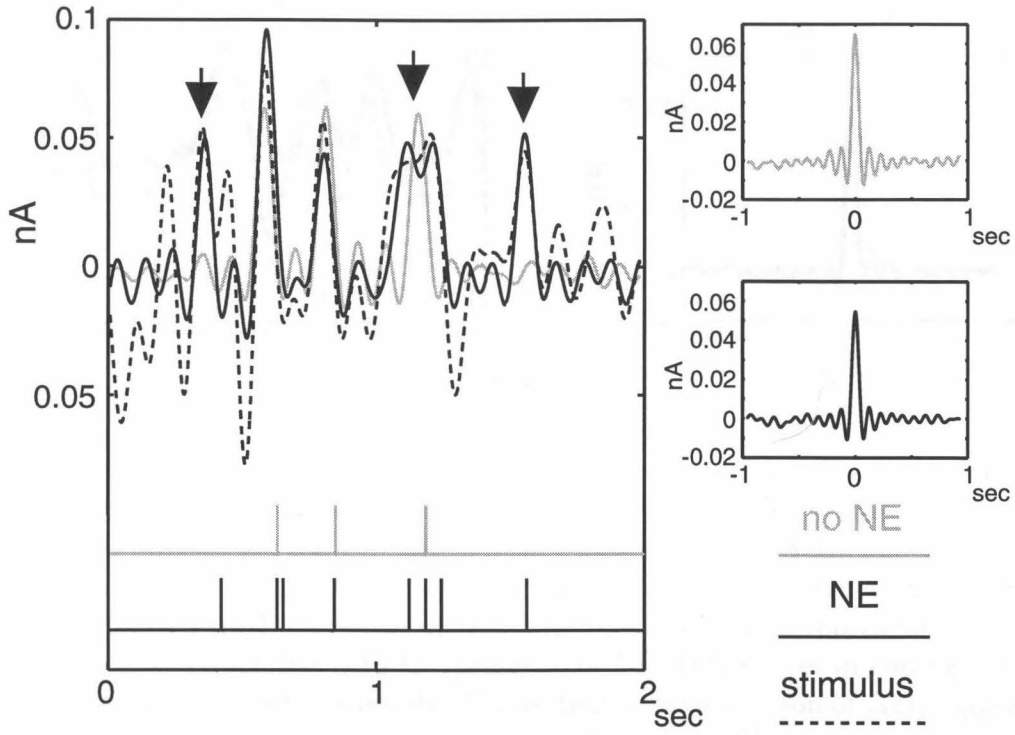

Figure 4.9: Stimulus reconstructions achieved in the absence and presence of NE. Filters used for the reconstructions are shown on the right and appear very similar. Spike trains generated in response to a stimulus repeat before and after application of NE are shown on the left where comparisons of the stimulus reconstructions achieved in the presence and absence of NE are compared. The higher quality reconstruction that is achieved in the presence of NE appears to be primarily the result of an increase in the number of spikes elicited by the stimulus. In this regard, NE permits the neuron to sample more features of the stimulus. Arrows indicate stimulus features that are only present in the NE reconstruction. All data come from the same cell.

$h(t)_{NE}$, using the following expression for difference in stimulus encoding:

$$\Delta e = 100 \left[1 - \frac{\gamma(h(t), \{t_i\}_{NE})}{\gamma(h(t)_{NE}, \{t_i\}_{NE})} \right] \tag{4.7}$$

measured as a percentage.

In four of the six cells examined, Δe was very small (1% - 6%). This implies that in these cases NE allows the neuron to encode a higher fraction of the stimulus in the spike train without changing the way in which individual spikes must be decoded. The values of Δe for the two cells which showed the most significant changes in their KW filters were 18% and 22%.

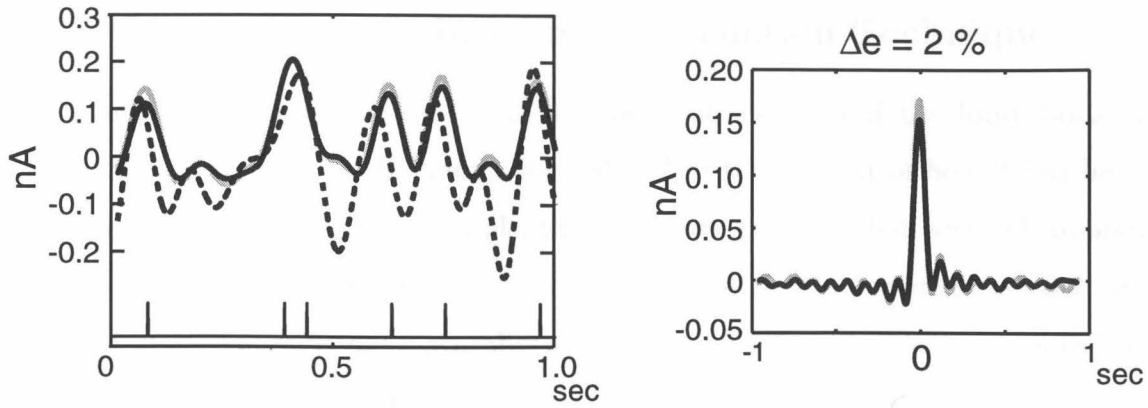

Figure 4.10: Comparison of reconstructions achieved when a spike train recorded in the presence of NE is convolved with KW filters that were obtained from the same cell using spike train data in the presence and absence of NE. The dashed line represents the stimulus while the gray line represents the reconstruction associated with filter generated in the absence of NE. The black solid line represents the filter and reconstruction associated with the presence of NE. Differences in coding fraction between the two reconstructions is only 2% (see text for explanation of Δe), suggesting that NE does not significantly change the properties of the filter.

4.5 Discussion

The goal of this chapter was to characterize the amount of stimulus information that is contained in pyramidal cell spike trains using stimuli with different kinds of temporal structure. We also examined the role that NE plays in modulating the amount of information in the spike train and the strategy required for decoding it. Our results can be summarized as follows. Stimuli that contained gamma frequency components (0-40 Hz) were much more poorly represented by physiological spike rates than lower frequency stimuli (0-10 Hz and 4-12 Hz). The addition of NE increased spike rates, coding fraction, and stimulus information, but decreased coding efficiency. Interestingly, the changes induced by NE did not result in a significant change in the structure of the reconstruction filters, suggesting that NE may increase the amount information in a spike train without requiring a change in the linear decoding strategy. In the discussion below we discuss some of the caveats associated with our methodology as well as the possible computational significance of the aforementioned results.

4.5.1 Limitations of Linear Reconstruction Technique

In interpreting the results of our analysis, we must understand the limitations of the linear reconstruction technique in general and in the context of how it has been applied here in particular. For example, this technique requires that we use Gaussian noise as our stimulus; however, statistical analyses of the environment (Olshausen and Field 1996) suggest that naturally occurring sensory stimuli are anything but noisy. Furthermore, studies of spike trains from bullfrog auditory neurons show that stimuli with the spectral characteristics of naturally occurring frog calls are far better represented than broadband noise (Rieke et al. 1995). Although we have made efforts to construct our stimulus based on the frequencies present in the EEG and pyramidal cell spike rates *in vivo*, it is probable that a more "natural" stimulus might have been represented more accurately.

A second issue we must contend with is the failure of the linear decoding scheme for some extreme (in the sense of a distribution) values of the stimulus. Although our analysis suggests that possible improvements that might result by the addition of nonlinear terms to the decoding process would be trivial because of the rarity of these extreme values, it is certainly possible that such events are more common in natural stimuli. Therefore, this issue warrants future investigation; however, it is equally possible that a natural stimulus may well cover a smaller range of values than those used by us.

4.5.2 Effects of different bandpassed stimuli

One of the primary goals of this chapter was to establish the extent to which stimuli with different frequency characteristics can be represented in pyramidal cell spike trains. Numerous authors have suggested that oscillations or events that take place on the same time scale as oscillations have a special significance in the context of neural processing. For example, some authors have suggested that fast oscillations (i.e., gamma, roughly 40 Hz) may reflect heightened attentiveness to a stimulus (Murthy and Fetz 1996). Others have suggested that slower oscillations may reflect

the computational parsing of information (Wilson and Bower 1992). Yet one must keep in mind that ultimately the importance of a stimulus is generally determined by whether or not it can generate a spike since this is the only thing that can be detected by the rest of the brain.

Our results suggest that the spike trains of individual pyramidal cells are capable of representing a substantial portion of stimuli that are bandpassed at 0-10 Hz and 4-12 Hz, while stimuli that were bandpassed at 0-40 Hz were represented half as well. Given that the filters generated by each of these stimuli consisted of only a single positive peak and the high degree of correlation that we found between spike rate and coding fraction, the inability of the neuron to accurately represent higher frequency stimuli may be entirely due to its limited spiking rate. As was previously mentioned, spike rates in the piriform cortex of rats typically show firing rates of 1-10 Hz (Nemitz and Goldberg 1983, McCollum et al. 1991) and, as we discovered in this study, it was not possible to obtain higher rates of firing for the durations of time that are required by the reconstruction technique. Therefore, the neuron's inability to accurately represent higher frequency stimuli may be limited in the awake behaving animal as well. However, given that spike rates are considerably higher prior to adaptation, it is possible that better representations of a stimulus may be accomplished in the biological system for brief periods of time. Unfortunately, the reconstruction technique described here requires long periods of time-invariance in the response which made it impossible to explore spike coding prior to adaptation.

The way in which the stimuli were bandpassed also appeared to affect the way in which negative peaks in the stimulus were represented. The reconstructions of both the 0-10 Hz and 0-40 Hz stimuli showed a very poor representation of the negative portions of the stimulus (see figure 4.5) while the 4-12 Hz stimulus was well represented in these areas. This is likely the result of the narrower frequency band occupied by this stimulus. When a spike occurs in response to this stimulus, it can only be preceded or followed by an oscillation in the narrow frequency range of 4-12 Hz while in the case of the other stimuli, a broader range is possible. Therefore, the ability of the neuron to represent negative peaks in the spike train may be more a

result of the mathematical properties of the stimulus rather than any physiological aspect of the neuron (although this certainly can not be ruled out). The possibility that the higher quality reconstructions possible with the 4-12 Hz stimulus are more a quality of the stimulus rather than the neuron should not trivialize this result since the occurrence of stimuli in this frequency range in awake behaving animals would also be better represented for the same reasons.

The structure of the of KW filters gives us insight into the properties of the neurons we are studying. For example, the structure of a filter at negative times (i.e., times before the occurrence of a spike) reflects the integration time of the neuron in the sense that it tells us how much stimulus history plays a role in the generation of a spike (Theunissen et al. 1996). However, the structure of the filter is bandlimited by the frequency range of the stimulus; therefore, such interpretations must be approached with caution. Previous studies (Theunissen et al. 1996, Bialek et al. 1991) have used broadband noise as stimuli, so that significant filter features reflect neuronal rather than stimulus properties; however, this approach carries a caveat with it as well. For example, one can consider a neuron where a hyperpolarization must have a duration of at least 100 $msec$ in order to elicit a spike via the "anode break" mechanism, while a depolarization must last only 10 $msec$ to elicit a spike. One might then expect that a stimulus in the 0-10 Hz range would produce a very different ratio of spikes generated by depolarization to spikes generated by hyperpolarization than a stimulus that was bandlimited at 0-100 Hz where one would expect a much higher proportion of spikes to be caused by depolarization. This point once again underscores the importance of using a naturally occurring stimulus.

Keeping these cautionary notes in mind, we can still discern the properties of the filter that are likely to reflect neuronal rather than stimulus properties. For example, the negative peaks preceding the zero-centered positive peaks in the filters generated from the 0-10 Hz and 0-40 Hz stimuli likely reflect some "anode-break" type behavior in these neurons since there is no reason that this asymmetry should exist given the stimulus frequency characteristics. However, the width of the zero-centered positive peak appears to be largely determined by the stimulus bandwidth in all of the filters

(except those calculated from the 0-400 Hz stimulus), yet the height of this positive peak reflects the amount of stimulus current necessary on average to evoke a spike.

4.5.3 Norepinephrine and spike coding

When NE was added to pyramidal cells during the course of stimulation, the firing rates of these neurons was increased. Accompanying this increase in firing rate was an increase in coding fraction and decrease in coding efficiency. Furthermore, the filters calculated from spike trains in the presence and absence of NE were very similar and almost identical coding fractions could be achieved using the non-NE filter to decode the spike train elicited in the presence of NE.

Previous authors (Segal and Bloom 1976, Madison and Nicoll 1982, Hasselmo et al. 1997) have suggested that NE may improve the cortical "signal to noise" ratio; however, no efforts have ever been made to quantify this in an information theoretic way. For example, Madison and Nicoll (1982) have suggested that NE-induced increases in excitability might contribute to a better representation of the signal. The data supporting this speculation was an increase in the number of spikes elicited by constant current pulses following the application of NE. However, the putative improvement in the quality of the signal representation was never quantified. Additionally, stimuli resembling constant current pulses are unlikely to occur in the brain which further complicates any conclusions that could be drawn from this study. In this chapter, we have used more realistic fluctuating stimuli to quantify the improvement of the stimulus representation in the spike train. We found that the amount of stimulus information in the spike train could increase by as much as 118% following application of NE. This result suggests that if NE does indeed act to improve the cortical "signal to noise" ratio, it may accomplish this partially by improving the stimulus representation in the spike trains of neurons.

In order to ascribe a biological meaning to these results, we must first assess how decoding in terms of the reconstruction technique relates to any decoding that would be done by a biological neuron. The analysis presented here establishes a

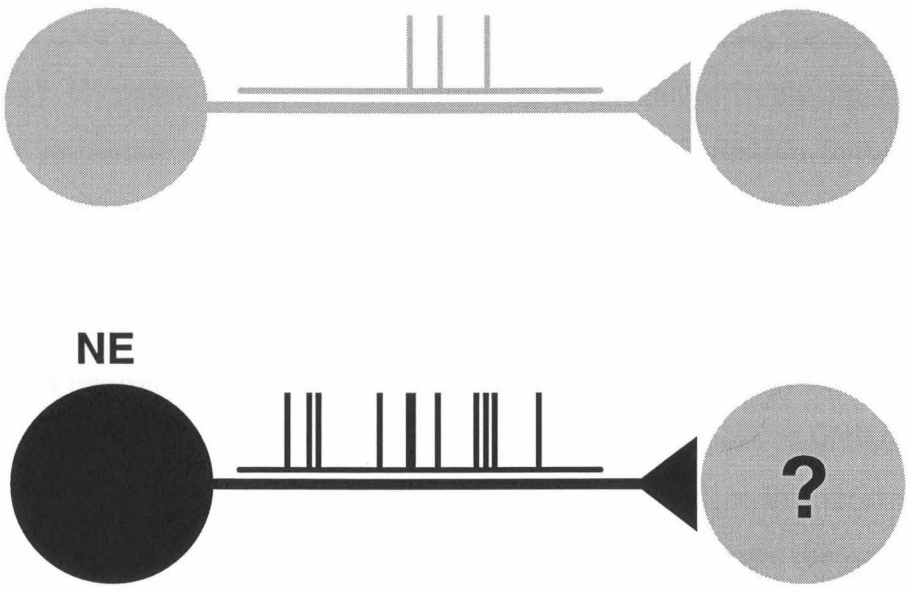

Figure 4.11: Possible advantage of having NE increase the number of spikes without changing the decoding strategy. A neuron receives input from a neuron that is then modulated by NE. How does it utilize spike train information in the modulated spike train? The study presented here suggests that the postsynaptic neuron receives a more informative spike train but does not have to change its decoding strategy to make sense of it.

statistical relationship between a current injection stimulus to the soma and the resulting spike train. The relationship between stimulus and spike train establishes theoretical boundaries regarding how much stimulus information can be extracted from a spike train given our experimental conditions. Assuming that our analysis is as accurate as possible, a postsynaptic neuron under the same experimental conditions could extract an equal or lesser amount of information, but never more. For example, a previous study has shown that neurons that are postsynaptic to electroreceptor cells in the electric fish extract only a subset of the stimulus features that are present in the receptor cell spike trains (Gabbiani et al. 1996). The study presented here does not speculate on what features a postsynaptic neuron may extract from a spike train, but rather it establishes the maximum amount of stimulus information that could be extracted from the spike train using a linear decoding method. The finding that NE does not necessitate a change in decoding strategy in most of the cells we examined suggests that the statistical relationship between the stimulus and the spike train

elicited by it does not change following application of NE (at least for the stimuli we chose to use); therefore, a downstream neuron is not required to change the way in which those spikes are utilized in order to preserve their information content.

Given the above caveats, the results presented in this chapter offer a possible solution to an important neural problem: How does a postsynaptic neuron interpret a presynaptic spike train that has been altered by the presence of NE? Our results suggest that a neuron is not required to change its decoding strategy in most cases to extract information from a presynaptic spike train that has been modulated by NE (figure 4.11). However, the luxury of maintaining a constant decoding strategy comes at a cost. Increases in the amount of spike train information require the production of a greater number of spikes, but these spikes each represent a smaller or equal amount of information about the stimulus (as measured by the coding efficiency). Since each spike has an energetic cost associated with it, the increase in spike train information associated with application of NE comes at a greater metabolic cost. Presumably, in a system as distributed as the brain, it is important to maintain consistency in the way information is coded, even if this consistency comes at a higher energetic cost.

5

Conclusions

In this chapter, I will discuss the contributions of the studies described in this thesis to the field of neuroscience and suggest future directions for research.

5.1 Contributions of this work

5.1.1 Pyramidal cell properties and single cell modeling

Previous models of piriform cortex pyramidal neurons have been used in network simulations (Wilson and Bower 1992, Barkai et al. 1994) and to test interpretations of voltage-clamp data (Banks et al. 1996); however, these models have been much simpler than the one I have presented here. For example, the pyramidal cell representations used in the Wilson and Bower (1992) model were integrate and fire units with passive properties based on sharp electrode data. When computer technology allowed for more sophisticated network simulations of piriform cortex, Barkai et al. (1994) constructed a model using pyramidal cells with three compartments and active behavior that was matched to experimental recordings (Barkai and Hasselmo 1994); however, this model was based on passive properties taken from sharp electrode data and was never able to replicate the fast adaptation or subthreshold oscillations that are observed experimentally. A simpler model of a pyramidal cell was constructed by Banks et al. (1996) to test the effects of different membrane distributions of the A-current on voltage-clamp recordings. This model had 21 compartments but did not attempt to model spiking behavior in the cell. The only active property it possessed was the A-current.

The model of a piriform cortex pyramidal neuron that has been presented here is

different from these previous studies in that it is more detailed and it has been able to match more of the experimentally recorded behavior of a real neuron. It is more detailed in the sense that it is based on a realistic dendritic morphology and has been matched to the passive properties of adult neurons with data from whole-cell recordings. It is more realistic because it can replicate the fast adaptation and subthreshold oscillations that are seen experimentally. It also suggested a novel explanation for the presence of subthreshold oscillations. While previous studies (Llinás et al. 1991, Gutfreund et al. 1995) have suggested that intrinsic subthreshold oscillations are simply the result of the interplay between different membrane currents, the modeling work presented here has suggested that membrane currents may generate oscillations with the help of intrinsic noise. Unfortunately, it was not possible to remove noise from the biological neuron, so this remains an untested hypothesis; however, the amplification of subthreshold oscillations in the 4-12 Hz range through the current injection of broadband noise is certainly consistent with this hypothesis.

5.1.2 Consequences of physiologically plausible patterns of synaptic input

Most previous single cell modeling studies have dealt with characterizing the responses of neurons to idealized patterns of synaptic input (Agmon-Snir and Segev 1993, Murthy and Fetz 1994, Bernander et al. 1994, Bernander et al. 1991, Rapp et al. 1992). In this thesis, I have presented a study which explores the significance of a physiologically plausible pattern of synaptic input for the behavior of a single pyramidal neuron. The results of these simulations provide an exception to a hypothesis put forth by Jefferys, Traub, and Whittingon that the gamma rhythm reflects the clocking of cortical computations. These authors make an analogy to digital computer technology and compare pyramidal cells to central processing units (CPUs) while inhibitory neurons acting through $GABA_A$-mediated inhibition are said to behave like computer clocks. In assessing the validity of this assertion, one must examine how computations actually occur in digital computers. The CPU is responsible for

carrying out all computations while the clock demarcates the beginning and end of a computation. Although an individual program may define a fixed sequence of computations over multiple clock cycles, there is nothing in the hardware of the computer that requires that a computation in one clock cycle be dependent on a computation in the previous clock cycle. However, the modeling results presented here suggest that the effects of single input patterns believed to underlie gamma oscillations last much longer than the duration of a single gamma oscillation which Jeffrys and colleagues consider a reflection of cortical clocking. Because synaptic inputs were tuned to the time courses associated with experimentally recorded synaptic currents, it is unlikely that the model would be so far off that effects that were shown to last 100 $msec$ (duration of 4 gamma oscillations) could last only 25 $msec$ in reality. Instead the model suggests that the much slower $GABA_B$ mediated inhibition might act to space out bursts of gamma activity so that a new burst would not be affected by the activity induced by previous bursts. In this sense, the $GABA_B$ inhibition may serve more of a clocking function in piriform cortex than the $GABA_A$ inhibition.

5.1.3 Spike coding in pyramidal neurons

The information theoretic analysis of piriform cortex pyramidal cell spike trains that is presented here is the first such investigation of a mammalian cortical neuron. The results presented here show that stimuli that incorporate the frequency of gamma oscillations (0-40 Hz) are only half as well represented as stimuli that encompass the *in vivo* spike rates of pyramidal cells (0-10 Hz) or the theta rhythm (4-12 Hz). However, previous studies have shown that multiple neurons may be able to encode a larger portion of stimuli that are otherwise poorly represented by individual neurons (Theunissen et al. 1996). The investigation presented here can not rule out the possibility that such multicellular coding may take place in the piriform cortex where a group of neurons all receive the same stimulus but each cell encodes a separate portion of it.

When Madison and Nicoll (1982) showed that NE can act to increase excitability

in hippocampal pyramidal cells, they suggested that this might somehow increase the neuronal "signal to noise" ratio. However, a precise mechanism by which this might be accomplished was never described nor did they attempt to quantify the putative improvement in signal representation. In the work presented in this thesis I have used the stimulus reconstruction technique (Bialek et al. 1991) to quantify an increase in spike train information induced by the application of NE. Furthermore, I show that for the stimuli I use, the presence of NE does not require a change in the linear spike decoding strategy. This result suggests that a neuron downstream of one that has been modulated by NE would not be required to change the way in which it processes spikes in order to maintain the stimulus representation in the spike train.

5.2 Future directions

The research reported here opens up a number of intriguing possibilities for future investigation. Some of these are briefly discussed here.

Given that past network models of piriform cortex have been based on pyramidal cell representations that are considerably less realistic than the detailed biophysical simulation described here, the incorporation of a simplified version of my single cell model should increase the level of confidence in the realism of a future network simulation. Although most of the dendritic complexity of the detailed simulation will have to be sacrificed in the name of computational feasibility, a simplified model would still display the active behavior of the full model since active conductances are restricted to the soma. Introduction of a simplified version of the model into a network would also allow an investigator to study the functional implications of subthreshold oscillations at the network level.

The information theoretic analysis of pyramidal cell spike trains suggests a number of avenues of inquiry. The work reported here utilized stimuli that were meant to approximate the temporal characteristics of field potential oscillations thought to reflect synaptic currents; however, the currents that enter the soma from the dendrites are most likely filtered in ways that may not be deducible from the field potentials

(Nunez 1981). The results in this study suggest that the type of stimulus used has a large role to play in the extent to which stimulus is represented in the spike train. It would therefore be useful to use a stimulus that more accurately represented somatic current input during an odor stimulus. Such a stimulus could be constructed by studying the statistics of intracellular fluctuations in membrane potential recorded *in vivo* from pyramidal cells during the course of odor stimulation.

The effects of NE on the information content and decoding requirements of spike trains raise a more general question: How similar are the effects of other neuromodulators on spike train information content? It is known that acetylcholine can increase excitability in piriform cortex pyramidal cells in much the some way that NE does (Constanti and Sim 1987a, Hasselmo and Bower 1992). It would therefore be interesting to see if this neuromodulator also increased spike train information content without requiring a change in the decoding strategy. Although the effects of dopamine and serotonin on piriform cortex pyramidal cells have not been studied, results from hippocampal pyramidal neurons suggest that these neuromodulators may change spike coding in ways that are different from NE. For example, dopamine is known to decrease neuronal excitability by increasing a Ca^{2+}-activated potassium conductance (Benardo and Prince 1982) and decreasing a sodium current (Cantrell et al. 1997). The effects of serotonin are similar to NE in the sense that the excitability of the neuron is ultimately increased; however, recent studies have suggested that serotonin modulates not only a Ca^{2+}-dependent potassium current, but also an inward rectifying potassium current (Okuhara and Beck 1994) as well as N- and P-type calcium currents (Foehring 1996). It would be intersting to see if the these modulators preserve the structure of the reconstruction filters in the same way that NE did. Intuitively, one might expect that a structure as complex as the brain might benefit from maintaining consistency in spike coding regardless of what neuromodulators might be present.

Appendix A: Role of piriform cortex in limbic epileptogenesis

The work reviewed in this appendix has little direct bearing on the research presented in this thesis. However, given that my stay at Caltech has been funded by the government, I felt obliged to provide at least one example of how a better understanding of piriform cortex might benefit the public.

The piriform cortex has recently attracted the attention of epilepsy researchers (see Löscher and Ebert, 1996, for a comprehensive and up-to-date review). Epileptic states can be induced in animals through kindling. This paradigm involves the periodic stimulation of cortical areas (typically in the limbic system) via chronically implanted electrodes. Although stimulation levels are initially subconvulsive, generalized seizures will eventually occur if the stimulation is continued. Interestingly, the piriform cortex has the lowest threshold of all limbic structures for induction of seizures via kindling (Racine et al. 1989). Additionally, even when seizures are induced in other areas of the limbic system (i.e., amygdala or hippocampus), the piriform cortex is the first area to show the interictal discharge which is considered a hallmark of many types of epilepsy (Kairiss et al. 1984). Further evidence of the crucial role that piriform cortex plays in the generation of limbic system seizures comes from studies which show that bilateral lesioning of the piriform cortex is successful in halting generalized seizures when kindling has taken place in the hippocampus and olfactory bulb (McIntyre and Kelly 1990). Although the precise reason has yet to be determined, it is believed that the central role piriform cortex plays in limbic epileptogenesis is most likely a result of the dense interconnectivity of excitatory elements within the cortex or possibly its proximity to certain motor structures (Löscher and Ebert 1996).

Unfortunately, almost all of our knowledge of the piriform cortex and its role in

epilepsy comes from animal models. Some circumstantial evidence, however, suggests that piriform cortex may play a role in human epilepsy as well. For example, generalized convulsions can be induced in human following stimulation of the uncus, the area which contains piriform cortex in humans (Penfield and Kristiansen 1951). In another study, uncinate fits were prevented by olfactory stimulation during olfactory auras (sensations preceding the onset of a seizure) (Efron 1956). One interpretation of this finding is that the piriform cortex is so involved in the perception of the stimulus that it can not be recruited in the spread of epileptic activity (Löscher and Ebert 1996).

Epilepsy affects approximately one percent of the global population, making it the second most common neurological illness (Martin 1991). At present, 10-20% of all epilepsies can not be treated with drugs (Theodore 1992) and often must be treated surgically. The majority of surgical patients suffer from temporal lobe epilepsy (encopassing the limbic system in humans) which is often treated by removal of portions of the amygdala and hippocampus. Tragically, these areas play an essential role in emotion and memory and their lesioning often has dire consequences for patients (Bauer et al. 1993, Adolphs et al. 1994). If the animal data discussed above can be generalized to humans, it is possible that removal of the piriform cortex may negate the necessity of removing areas in the amygdala or hippocampus that may be more essential to a patient's quality of life. Unfortunately, no studies assessing the value of piriform cortex removal in humans have been performed to date (Löscher and Ebert 1996).

Appendix B: Computational models of piriform cortex

A summary and critique of various computational models of piriform cortex is provided here for those readers who would be interested in a deeper analysis than the one provided in the introduction.

Wilson and Bower (1989) constructed a biologically realistic model of piriform cortex that was able to behave much like an associative memory. It was able to reconstruct partially degraded patterns of olfactory input, but was also able to discriminate between similar odor patterns. In this simulation, only synaptic connections between inhibitory neurons and pyramidal cells and between pyramidal cells (association pathways) were modifiable. The success of the model suggested that these pathways could be the site of synaptic plasticity in the real cortex as well. Further modeling work by Hasselmo et al. (1992) used a more abstract neural network architecture to study the effects of cholinergic modulation. Here too, associative memory function was accomplished via plasticity in the association fiber pathways. A later detailed biophysical simulation also supported this finding (Barkai et al. 1994).

Ambros-Ingerson, Granger, and Lynch constructed a model which identified odors through hierarchical clustering. These simulations had biologically plausible patterns of connectivity but lacked much of the biophysical detail contained in other realistic simulations (Wilson and Bower 1988, Barkai et al. 1994). Yet, unlike the previously discussed models, this simulation included a model of the bulb which made reciprocal connections with the piriform cortex. Odor identification was accomplished by an iterative process whereby the network clustered inputs into successively more exclusive groups of neural activity. Therefore, the first iteration of network activity may evoke a pattern of network activity that is general for all "fruity" smells, while the last may generate a pattern that is only active for "banana." This model assumes

that plasticity in the synapses of the afferent layer of piriform cortex are primarily responsible for accomplishing this.

A more recent conceptual model by Hopfield (1995) departs from traditional models of associative memory and suggests that odors are coded in piriform cortex by spike timings relative to subthreshold oscillations. In this model, the olfactory bulb provides input to the piriform cortex that codes for different odorant intensities that make up a smell. For example, one smell might be represented by an intensity vector that codes for three individual odorants (e.g., with concentration ratios of 1:3:2). The strength of bulbar input for individual odorants then determines how soon a piriform cortex cell will fire relative to subthreshold oscillations always present in piriform cortex neurons. An input representing a high concentration of odorant would make the cortical cell fire early in the upswing of the subthreshold oscillation, while a weaker input representing lower concentration would make the cell fire later. In this way, the piriform cortex would generate a temporal code based on spike timing to read out the odorant concentration vector and "recognize" the smell.

One advantage of the associative memory models is that they make predictions that are easily tested experimentally. For example, the Wilson-Bower (1988) model and those developed by Hasselmo and colleagues (Hasselmo et al. 1992, Barkai et al. 1994) all require that the primary location of synaptic plasticity be in the association fiber pathway. Experimental evidence from slice experiments does indeed show that long term potentiation (LTP) induced along the association pathway is significantly stronger than what is seen in the afferent pathway (Kanter and Haberly 1990). This seems to contradict an assumption of the hierarchical clustering model which made the afferent pathway the primary site of potentiation; however, *in vivo* experiments have shown the presence of significant levels of LTP in the afferent pathway following learning (Roman et al. 1987). Given the presence of $NMDA$ receptors in both Ia (afferent) and Ib (associative) layers of pyramidal cell dendrites, it is likely that LTP occurs at both pathways and that perhaps the present models are incomplete.

The success of abstract neural networks has prompted many researchers to suggest that different brain areas may serve as some form of associative memory. For exam-

ple, associative memory models exist for hippocampus (Treves and Rolls 1994) and the inferotemporal (IT) area of visual cortex as well (Rolls 1994). It is conceivable that many if not all brain areas subserve some type of associative memory function. Perhaps then a better question would be: If both area IT and piriform cortex subserve associative memory function, why are their structures so different? Given that one area deals with olfactory information and the other with visual suggests that the architectures of these brain areas are likely to reflect the computational problems associated with their respective senses. Unfortunately, the piriform cortex associative memory models discussed here use only idealized inputs that are unlikely to reflect the temporal or spatial structure of real olfactory input. The Hopfield (1995) model made some attempt to correlate the mechanism of odor recognition with the structure of olfactory stimuli, but its conceptual nature makes it difficult to test experimentally.

Although the above models are valiant attempts at explaining the function of piriform cortex, a complete model will necessarily require an understanding of olfactory stimulus space and the significance of input from the olfactory bulb. At present, olfactory stimulus space is poorly understood because the sensory transduction process remains murky. There was some reason for optimism in 1991 when Buck and Axel discovered a gene family that was thought to encode olfactory receptor proteins. Unfortunately, with the exception of one controversial report (Raming et al. 1993), these genes have yet to be functionally expressed and recent work (Mombaerts 1996) suggests that this gene family may be more important in olfactory system development.

Some intuition about the purpose of piriform cortex may come from looking at invertebrate olfactory systems. Interestingly, the neural architecture of insect olfactory systems is very similar to that of vertebrates' (for a review see Hildebrand and Shepherd (1997)), suggesting that the structure of these brain areas may reflect the computational challenges surrounding olfaction. For example, the mammalian olfactory system begins with odorant receptor cells in the mucus covered nasal epithelium which then project to anatomical structures called glomeruli in the olfactory bulb. Output from the bulb is then sent to the piriform cortex. Similarly, odorant recep-

tor cells in the insect antenna are surrounded by lymph. These cells also project to glomerular structures, but in the antennal lobe which then projects to the mushroom body which is believed, much like the piriform cortex, to be involved in olfactory memory (Connolly et al. 1996). Responses to olfactory stimuli are also similar. For example, both mammalian piriform cortex (Adrian 1942, Freeman 1960) and the insect mushroom body (Laurent and Naraghi 1994) have oscillatory responses to odor stimuli. The accessibility of insect olfactory areas and the ability to easily do experiments in the absence of anesthesia may make the insect a good model system from which ideas about piriform cortex can be developed. Unfortunately, at present the nature of olfactory stimulus space for insects is no better understood than it is for vertebrates. In the meantime, additional insights are likely to come from work being done to develop an artificial nose (Dickinson et al. 1996, Lonergan et al. 1996). These efforts are likely to uncover many of the algorithmic issues associated with olfaction much like computer vision has done for visual physiology (Marr 1982).

Bibliography

Abraham, A. and Mathai, K. V. (1983). The effect of right temporal lobe lesions on matching of smells, *Neuropsycologia* **21**: 277–281.

Adams, M. E. and Swanson, G. (1996). Tins neurotoxins supplement, *Trends Neurosci.* **19(6)**: Suppl.

Adolphs, R., Tranel, D., Damasio, H. and Damasio, A. (1994). Impaired recognition of emotion in facial expressions following bilateral damage to the human amygdala, *Nature* **372**: 669–672.

Adrian, E. D. (1942). Olfactory reactions in the brain of the hedgehog, *J. Physiol. (London)* **100**: 459–473.

Agmon-Snir, H. and Segev, I. (1993). Signal delay and input synchronization in passive dendritic structures, *J. Neurophysiol.* **70**: 2066–2085.

Ambros-Ingerson, J., Granger, R. and Lynch, G. (1990). Simulation of paleocortex performs hierarchical clustering, *Science* **247**: 1344–1348.

Angelides, K. J., Elmer, L. W., Loftus, D. and Elson, E. (1988). Distribution and lateral mobility of voltage-dependent sodium channels in neurons, *J. Cell Biol.* **106**: 1911–1925.

Aston-Jones, G. and Bloom, F. E. (1981). Activity of norepinephrine-containing locus coeruleus neurons in behaving rats anticipates fluctuations in the sleep-waking cycle, *J. Neurosci.* **1**: 876–886.

Aston-Jones, G., Rajkowski, J., Kubiak, P. and Alexinsky, T. (1994). Locus coeruleus neurons in monkey are selectively activated by attended cues in a vigilance task, *J. Neurosci* **14**: 4467–4480.

Bair, W. and Koch, C. (1996). Temporal precision of spike trains in extrastriate cortex of the behaving macaque monkey, *Neural. Comput.* **8**: 1185–1202.

Banks, M. I., Haberly, L. B. and Jackson, M. B. (1996). Layer-specific properties of the transient K current (I_A) in piriform cortex, *J. Neurosci.* **16(12)**: 3862–3876.

Baranyi, A., Szente, M. B. and Woody, C. D. (1993). Electrophysiological characterization of different types of neurons recorded *in vivo* in the motor cortex of the cat. II. Membrane parameters, action potentials, current-induced voltage responses and electrotonic structures, *J. Neurophysiol.* **69(6)**: 1865–1879.

Barkai, E. and Hasselmo, M. E. (1994). Modulation of the input/output function of rat piriform cortex pyramidal cells, *J. Neurophysiol.* **72(2)**: 644–658.

Barkai, E., Bergman, R. E., Horwitz, G. and Hasselmo, M. E. (1994). Modulation of associative memory function in a biophysical simulation of rat piriform cortex, *J. Neurophysiol.* **72(2)**: 659–677.

Barrie, J. M., Freeman, W. J. and Lenhart, M. D. (1996). Sptiotemporal analysis of prepyriform, visual, auditory, and somesthetic surface EEGs in trained rabbits, *J. Neurophysiol.* **76**: 520–539.

Bauer, R. M., Tobias, B. and Valenstein, E. (1993). Amnesic disorders, *in* K. M. Heilman and E. Valenstein (eds), *Clinical Neuropsychology*, Oxford University Press, New York, pp. 523–602.

Benardo, L. S. and Prince, A. (1982). Dopamine action on hippocampal pyramidal cells, *J. Neurosci.* **2**: 415–423.

Bernander, O., Douglas, R. J., Martin, K. A. C. and Koch, C. (1991). Synaptic background activity influences spatiotemporal integration in single pyramidal cells, *Proc. Nat. Acad. Sci. USA* **88**: 11569–11573.

Bernander, O., Koch, C. and Usher, M. (1994). The effect of synchronized inputs at the single neuron level, *Neural Comput.* **6**: 622–641.

Bialek, W., Rieke, F., de Ruyter van Steveninck, R. R. and Warland, D. (1991). Reading a neural code, *Science* **252**: 1854–1857.

Bower, J. M. and Beeman, D. (1995). *The Book of GENESIS: Exploring Realistic Neural Models with the GEneral NEural SImulation System*, Springer-Verlag, New York.

Bragin, A., Jandó, G., Nádasdy, Z., Hetke, J., Wise, K. and Buzsáki, G. (1995). Gamma (40-100 Hz) oscillation in the hippocampus of the behaving rat, *J. Neurosci.* **15**: 47–60.

Bressler, S. L. (1988). Changes in electrical activity of rabbit olfactory bulb and cortex to conditioned odor stimulation, *Behav. Neurosci.* **102**: 740–747.

Bressler, S. L. (1990). The gamma wave: a cortical information carrier?, *Trends Neurosci.* **13**: 161–162.

Brown, D. A., Gähwiler, B. H., Griffith, W. H. and Halliwell, J. V. (1990). Membrane currents in hippocampal neurones, *in* J. Storm-Mathisen, J. Zimmer and O. P. Ottersen (eds), *Progress in Brain Research, Vol. 83*, Elsevier Science Publishers, New York, pp. 141–160.

Buck, L. and Axel, R. (1991). A novel multigene family may encode odorant receptors: a molecular basis for odor recognition, *Cell* **65**: 175–187.

Buck, L. B. (1996). Information coding in the vertebrate olfactory system, *Ann. Rev. Neurosci.* **19**: 517–544.

Cain, W. S. (1978). History of research on smell, *Handbook of Perception, Volume VIA*, Academic Press, pp. 197–229.

Cantrell, A. R., Smith, R. D., Goldin, A. L., Scheuer, T. and Catterall, W. A. (1997). Dompaminergic modulation of sodium current in hippocampal neurons via cAMP-dependent phosphorylation of specific sites in the sodium channel α-subunit, *J. Neurosci.* **17**: 7330–7338.

Cattarelli, M., Astic, L. and Kauer, J. S. (1988). Metabolic mapping of 2-deoxyglucose uptake in the rat piriform cortex using computerized image processing, *Brain Res.* **442**: 180–184.

Cherubini, E., Ben-Ari, Y. and Krnjević, K. (1989). Anoxia produces smaller changes in synaptic transmission, membrane potential, and input resistance in immature rat hippocampus, *J. Neurophysiol* **62**: 882–895.

Cobb, S. R., Buhl, E. H., Halasy, K., Paulsen, O. and Somogyi, P. (1995). Synchronization of neuronal activity in hippocampus by individual GABAergic interneurons, *Nature* **378**: 75–78.

Connolly, J. B., Roberts, I. J. H., Armstrong, J. D., Kaiser, K., Forte, M., Tully, T. and O'Kane, C. J. (1996). Associative learning disrupted by impaired G_s signaling in *drosophila* mushroom bodies, *Science* **274**: 2104–2107.

Constanti, A. and Galvan, M. (1983). Fast-inward rectifying current accounts for anomalous rectification in olfactory cortex neurones, *J. Physiol.* **385**: 153–178.

Constanti, A. and Sim, J. A. (1987a). Calcium-dependent potassium conductance in guinea-pig olfactory cortex neurones *in vitro*, *J. Physiol.* **387**: 173–194.

Constanti, A. and Sim, J. A. (1987b). Muscarinic receptors mediating suppression of the m-current in guinea-pig olfactory cortex neurones may be of the m2-subtype, *Br. J. Pharmac.* **90**: 3–5.

Constanti, A., Galvan, M., Franz, P. and Sim, J. A. (1985). Calcium-dependent inward currents in voltage clamped guinea-pig olfactory cortex neurones, *Pfülgers Arch.* **404**: 259–265.

Crick, F. and Koch, C. (1990). Towards a neurobiological theory of consciousness, *Sem. Neurosci.* **2**: 263–275.

De Schutter, E. and Bower, J. M. (1994a). An active membrane model of the cerebellar Purkinje-cell II. Simulation of synaptic responses, *J. Neurophysiol.* **71(1)**: 401–419.

De Schutter, E. and Bower, J. M. (1994b). An active membrane model of the cerebellar Purkinje-cell I. Simulation of current clamps in slice, *J. Neurophysiol.* **71(1)**: 375–400b.

Dickinson, T. A., White, J., Kauer, J. S. and Walt, D. R. (1996). A chemical-detecting system based on a cross-reactive optical sensor array, *Nature* **382**: 697–700.

Eccles, J. C. (1994). *How the self controls its brain*, Springer-Verlag, Berlin.

Eckhorn, R., Bauer, R., Jordan, W., Brosch, M., Kruse, W., Munk, M. and Reitboeck, H. J. (1988). Coherent oscillations: A mechanism of feature linking in the visual cortex ?, *Biol. Cybern.* **60**: 121–130.

Efron, R. (1956). The effect of olfactory stimulation in arresting uncinate fits, *Brain* **79**: 267–281.

Eichenbaum, H., Morton, T. H., Potter, H. and Corkin, S. (1983). Selective olfactory deficits in case H.M., *Brain* **106**: 459–472.

Fisher, R. E., Gray, R. and Johnston, D. (1990). Properties and distribution of single voltage-gated calcium channels in adult hippocampal neurons, *J. Neurophysiol.* **64(1)**: 91–104.

Foehring, R. C. (1996). Serotonin modulates N- and P-type calcium currents in neocortical pyramidal neurons via a membrane-delimited pathway, *J. Neurophysiol.* **75**: 648–659.

Foote, S. L., Bloom, F. E. and Aston-Jones, G. (1983). Nucleus locus ceruleus: New evidence of anatomical and physiological specificity, *Physiological Reviews* **63**: 844–913.

Freeman, W. and Barrie, J. (1994). Chaotic oscillations and the genesis of meaning in cerebral cortex, *in* G. B. amd R. Llinas, W. Singer, A. Berthoz and Y. Christen (eds), *Temporal Coding in the Brain*, Springer-Verlag, Berlin, pp. 13–37.

Freeman, W. J. (1959). Distribution in time and space of prepyriform electrical activity, *J. Neurophysiol.* **22**: 644–665.

Freeman, W. J. (1960). Correlation of electrical activity of prepyriform cortex and behavior in cat, *J. Neurophysiol.* **23**: 111–131.

Freeman, W. J. (1975). *Mass action in the nervous system*, Academic Press, New York.

Freeman, W. J. (1991). The physiology of perception, *Sci. Amer.* **264**: 78–85.

French, C. R., Sah, P., Buckett, K. J. and Gage, P. W. (1990). A voltage-dependent persistent sodium current in mammalian hippocampal neurons, *J. Gen. Physiol.* **95**: 1139–1157.

Gabbiani, F. and Koch, C. (1996). Coding of time-varying signals in spike trains of integrate-and-fire neurons with random threshold, *Neural Comput.* **8**: 44–66.

Gabbiani, F., Metzner, W., Wessel, R. and Koch, C. (1996). From stimulus encoding to feature extraction in weakly electric fish, *Nature* **384**: 564–567.

Goldman, D. (1943). Potential, impedence, and rectification in membranes, *J. Gen. Physiol.* **21(1)**: 37–60.

Gray, C. M. (1994). Synchronous oscillations in neuronal systems: mechanisms and functions, *J. Comput. Neurosci.* **1**: 11–38.

Gray, C. M., Konig, P., Engel, A. K. and Singer, W. (1989). Oscillatory responses in cat visual-cortex exhibit inter-columnar synchronization which reflects global stimulus properties, *Nature* **338**: 334–337.

Gutfreund, Y., Yarom, Y. and Segev, I. (1995). Subthreshold oscillations and resonant-frequency in Guinea-pig cortical neurons: Physiology and modeling, *J. Physiol.* **483(3)**: 621–640.

Haberly, L. and Behan, M. (1983). Structure of the piriform cortex of the opossum. III. Ultrastructural characterization of synaptic terminals of association and olfactory bulb afferent fibers, *J. Comp. Neurol.* **219**: 448–460.

Haberly, L. B. (1983). Structure of the piriform cortex of the opossum. I. description of neuron types with golgi methods, *J. Comp. Neurol.* **213**: 163–187.

Haberly, L. B. (1985). Neuronal circuitry in olfactory cortex: anatomy and functional applications, *Chemical Senses* **10**: 219–238.

Haberly, L. B. (1990a). Comparative aspects of olfactory cortex, *in* E. G. Jones and A. Peters (eds), *Cerebral Cortex: Volume 8B Comparative Structure and Evolution of the Cerebral Cortex, Part II*, Plenum Press, New York, pp. 137–160.

Haberly, L. B. (1990b). Olfactory cortex, *in* G. M. Shepherd (ed.), *The Synaptic Organization of the Brain*, Oxford University Press, New York, chapter 10, pp. 317–345.

Haberly, L. B. and Bower, J. M. (1984). Analysis of association fiber pathway in piriform cortex with intracellular recording and staining techniques, *J. Neurophysiol.* **51**: 90–112.

Haberly, L. B. and Bower, J. M. (1989). Olfactory cortex – model circuit for study of associative memory, *Trends Neurosci.* **12**: 258–264.

Haberly, L. B. and Presto, S. (1986). Ultrastructural analysis of synaptic relationships of intracellularly stained pyramidal cell axons in piriform cortex, *J. Comp. Neurol.* **248**: 464–474.

Haberly, L. B., Hansen, D. J., Feig, S. L. and Presto, S. (1987). Distribution and ultrastructure of neurons in opossum piriform cortex displaying immunoreactivity to GABA and GAD and high-affinity tritiated GABA uptake, *J. Comp. Neurol.* **266**: 269–290.

Hasselmo, M. E. and Bower, J. M. (1992). Cholinergic suppression specific to intrinsic not afferent fiber synapses in rat piriform (olfactory) cortex, *J. Neurophysiol.* **67**: 1222–1229.

Hasselmo, M. E., Anderson, B. P. and Bower, J. M. (1992). Cholinergic modulation of cortical associative memory function, *J. Neurophysiol.* **67(5)**: 1230–1246.

Hasselmo, M. E., Linster, C., Patil, M., Ma, D. and Cekic, M. (1997). Noradrenergic suppression of synaptic transmission may influence cortical signal-to-noise ratio, *J. Neurophysiol.* **77**: 3326–3339.

Heimer, L. (1968). Synaptic distribution of centripetal and centrifugal nerve fibres in the olfactory system of the rat. An experimental anatomical study, *J. Anat.* **103(3)**: 413–432.

Hertz, J., Krough, A. and Palmer, R. G. (1991). *Introduction to the theory of neural computation*, Addison-Wesley Publishing Company, Menlo Park, California.

Hildebrand, J. G. and Shepherd, G. M. (1997). Mechanisms of olfactory discrimination: Converging evidence for common principles across phyla, *Ann. Rev. Neurosci.* **20**: 595–631.

Hille, B. (1992). *Ionic Channels of Excitable Membranes*, second edn, Sinauer Associates Inc., Sunderland, MA.

Hines, M. (1984). Efficient computation of branched nerve equations, *Int. J. Bio-Medical Computing* **15(1)**: 69–76.

Hodgkin, A. L. and Huxley, A. F. (1952). A quantitative description of membrane current and its application to conduction and excitation in nerve, *J. Physiol.* **117**: 500–544.

Hodgkin, A. L. and Katz, B. (1949). The effect of sodium ions on the electrical activity of the giant axon of the squid, *J. Physiol.* **108**: 37–77.

Holmes, W. R. and Levy, W. B. (1990). Insights into associative long-term potentiation from computational models of NMDA receptor-mediated calcium influx and intracellular calcium concentration changes, *J. Neurophysiol.* **63(5)**: 1148–1168.

Hopfield, J. J. (1982). Neural networks and physical systems with emergent collective computational abilities, *Proc. Nat. Acad. Sci. USA* **79**: 2554–2558.

Hopfield, J. J. (1995). Pattern recognition computation using action potential timing for stimulus representation, *Nature* **376**: 33–36.

Horn, R. and Marty, A. (1988). Muscarinic activation of ionic currents measured by a new whole-cell recording method, *J. Gen. Physiol.* **92**: 145–159.

Jack, J. J. B., Noble, D. and Tsien, R. W. (1988). *Electric Current Flow in Excitable Cells*, Oxford University Press, Oxford.

Jan, L. Y. and Jan, Y. N. (1976). L-glutamate as an excitatory transmitter at the drosophila larval neuromuscular junction, *J. Physiol.* **262**: 215–236.

Jefferys, J. G. R., Traub, R. D. and Whittington, M. A. (1996). Neuronal networks for induced 40 hz rhythms, *Trends Neurosci.* **19(5)**: 202–208.

Jones-Gotman, M. and Zatorre, R. J. (1988). Olfactory identification deficits in patients with focal cerebral excision, *Neuropsychologia* **26**: 387–400.

Jones-Gotman, M. and Zatorre, R. J. (1993). Odor recognition memory in humans: Role of right temporal and orbitofrontal regions, *Brain and Cognition* **22**: 182–198.

Jung, M. W., Larson, J. and Lynch, G. (1990). Role of NMDA and non-NMDA receptors in synaptic transmission in rat piriform cortex, *Exp. Brain Res.* **82**: 451–455.

Kairiss, E. W., Racine, R. J. and Smith, G. K. (1984). The development of the interictal spike during kindling in the rat, *Brain Res.* **322**: 101–110.

Kanter, E. D. and Haberly, L. B. (1990). NMDA-dependent induction of long-term potentiation in afferent and association fiber systems of piriform cortex *in vitro.*, *Brain Res.* **525**: 175–179.

Kanter, E. D., Kapur, A. and Haberly, L. B. (1996). A dendritic $GABA_A$-mediated IPSP regulates facilitation of NMDA-mediated responses to burst stimulation of afferent fibers in piriform cortex, *J. Neurosci.* **16(1)**: 307–312.

Ketchum, K. L. and Haberly, L. B. (1991). Fast oscillations and dispersive propagation in olfactory cortex and other cortical areas: A functional hypothesis, *in* J. Davis and H. Eichenbaum (eds), *Olfaction: A Model System for Computational Neuroscience*, MIT Press, Cambridge, Massachusetts, chapter 3, pp. 69–100.

Ketchum, K. L. and Haberly, L. B. (1993a). Membrane currents evoked by afferent fiber stimulation in rat piriform cortex. I. Current source-density analysis, *J. Neurophysiol.* **69(1)**: 248–260.

Ketchum, K. L. and Haberly, L. B. (1993b). Membrane currents evoked by afferent fiber stimulation in rat piriform cortex. II. Analysis with a system model, *J. Neurophysiol.* **69(1)**: 261–281.

Ketchum, K. L. and Haberly, L. B. (1993c). Synaptic events that generate fast oscillations in piriform cortex, *J. Neurosci.* **13(9)**: 3980–3985.

Kobayashi, T., Storrie, B., Simons, K. and Dott, C. G. (1992). A functional barrier to movement of lipids in polarized neurons, *Nature* **359**: 647–650.

Lampl, I. and Yarom, Y. (1997). Subthreshold oscillations and resonant behavior: Two manifestations of the same mechanism, *Neurosci* **78**: 325–341.

Larkman, A. U. (1991). Dendritic morphology of pyramidal neurones of the visual cortex of the rat: III. Spine distributions, *J. Comp. Neurol.* **306**: 332–343.

Laurent, G. and Naraghi, M. (1994). Odorant-induced oscillations in the mushroom bodies of the locust, *J. Neurosci.* **14**: 2993–3004.

Levin, H. S., High, W. M. and Eisenberg, H. M. (1985). Impairment of olfactory recognition after closed head injury, *Brain* **108**: 579–591.

Li, X.-G., Somogyi, P., Tepper, J. M. and Buzsàki, G. (1992). Axonal and dendritic arborization of an intracellularly labeled chandelier cell in the CA1 region of rat hippocampus, *Exp. Brain Res.* **90**: 519–525.

Ling, D. S. F. and Benardo, L. S. (1994). Properties of isolated $GABA_B$-mediated inhibitory postsynaptic currents in hippocampal pyramidal cells, *Neurosci.* **63(4)**: 937–944.

Llinás, R. R., Grace, A. A. and Yarom, Y. (1991). *In vitro* neurons in mammalian cortical layer 4 exhibit intrinsic oscillatory activity in the 10- to 50- hz frequency range, *Proc. Natl. Acad. Sci. USA* **88**: 897–901.

Lonergan, M. C., Severin, E. J., Doleman, B. J., Beaber, S. A., Grubbs, R. H. and Lewis, N. S. (1996). Array-based vapor sensing using chemically sensitive carbon black-polymer resistors, *Chem. Mater.* **8**: 2298–2312.

Löscher, W. and Ebert, U. (1996). The role of the piriform cortex in kindling, *Prog. in Neurobiol.* **50**: 427–481.

Luskin, M. B. and Price, J. L. (1983). The laminar distribution of intracortical fibers originating in the olfactory cortex of the rat, *J. Comp. Neurol.* **216**: 292–302.

Lynch, G. and Granger, R. (1991). Serial steps in memory processing: Possible clues from the olfactory-hippocampal circuit, *in* J. Davis and H. Eichenbaum (eds), *Olfaction: A Model System for Computational Neuroscience*, MIT Press, Cambridge, Massachusetts, chapter 6, pp. 69–100.

Macrides, F., Eichenbaum, H. B. and Forbes, W. B. (1982). Temporal relationship between sniffing and the limbic theta-rhythm during odor discrimination reversal-learning, *J. Neurosci.* **2**: 1705–1717.

Madison, D. V. and Nicoll, R. A. (1982). Noradrenaline blocks accommodation of pyramidal cell discharge in the hippocampus, *Nature* **299**: 636–638.

Madison, D. V. and Nicoll, R. A. (1986a). Actions of noradrenaline recorded intracellularly in rat hippocampal CA1 pyramidal neurones, *in vitro*, *J. Physiol.* **372**: 221–244.

Madison, D. V. and Nicoll, R. A. (1986b). Cyclic adenosine 3′, 5′-monophosphate mediates β-receptor actions of noradrenaline in rat hippocampal pyramidal cells, *J. Physiol.* **372**: 245–259.

Magee, J. C. and Johnston, D. (1995). Synaptic activation of voltage-gated channels in the dendrites of hippocampal pyramidal neurons, *Science* **268(5208)**: 301–304.

Magee, J. C. and Johnston, D. (1997). A synaptically controlled, associative signal for Hebbian plasticity in hippocampal neurons, *Science* **275**: 209–213.

Major, G., Larkman, A. U., Jonas, P., Sakmann, B. and Jack, J. J. B. (1994). Detailed passive cable models of whole-cell recorded CA3 pyramidal neurons in rat hippocampal slices, *J. Neurosci* **14(8)**: 4613–4638.

Manor, Y., Rinzel, J., Segev, I. and Yarom, Y. (1997). Low-amplitude oscillations in the inferior olive: A model based on electrical coupling of neurons with heterogeneous channel densities, *J. Neurophysiol.* **77**: 2736–2752.

Marder, E. and Calabrese, R. L. (1996). Principles of rhythmic motor pattern generation, *Physiol. Rev.* **76**: 687–717.

Markram, H., Lübke, J., Frotscher, M. and Sakmann, B. (1997). Regulation of synaptic efficacy by coincidence of postsynaptic APs and EPSPs, *Science* **275**: 213–215.

Marr, D. (1982). *Vision: A computational investigation into the human representation and processing of visual information*, W. H. Freeman, New York.

Martin, J. H. (1991). The collective electrical behavior of cortical neurons: The electroencephalogram and the mechanisms of epilepsy, *in* E. R. Kandel, J. H. Schwartz and T. M. Jessell (eds), *Principles of Neural Science*, Appleton and Lange, Norwalk, Connecticut, pp. 777–791.

Mason, A., Nicoll, A. and Stratford, K. (1991). Synaptic transmission between individual pyramidal neurons of the visual cortex *in vitro*, *J. Neurosci.* **11(1)**: 72–84.

McCollum, J., Larson, J., Otto, T., Schottler, F., Granger, R. and Lynch, G. (1991). Short-latency single unit processing in olfactory cortex, *J. Cogn. Neurosci.* **3(3)**: 293–299.

McIntyre, D. C. and Kelly, M. E. (1990). Is the piriform cortex important for limbic kindling?, *in* J. A. Wada (ed.), *Kindling, Vol. 4*, Plenum Press, New York, pp. 21–32.

McNaughton, B. L., Barnes, C. A. and Andersen, P. (1981). Synaptic efficacy and EPSP summation in granule cells of rat fascia dentata studied *in vitro*, *J. Neurophysiol.* **46(5)**: 952–966.

Mintz, I. M., Adams, M. E. and Bean, B. P. (1992). P-type calcium channels in rat central and peripheral neurons, *Neuron* **9**: 85–95.

Mitzdorf, U. (1985). Current source-density method and application in cat cerebral cortex: Investigation of evoked potentials and EEG phenomena., *Physiol. Rev.* **65(1)**: 37–100.

Mombaerts, M. (1996). Targeting olfaction, *Curr. Opin. Neurobiol.* **6**: 481–486.

Murthy, V. N. and Fetz, E. E. (1994). Effects of input synchrony on the firing rate of a three-conductance cortical neuron model, *Neural Comput.* **6**: 1111–1126.

Murthy, V. N. and Fetz, E. E. (1996). Oscillatory activity in sensorimotor cortex of awake monkeys: Synchronization of local field potentials and relation to behavior, *J. Neurophysiol.* **76**: 3949–3967.

Nemitz, J. W. and Goldberg, S. J. (1983). Neuronal responses to rat pyriform cortex to odor stimulation: an extracellular and intracellular study, *J. Neurophysiol.* **49**: 188–203.

Nicolelis, M. A. L., Baccala, L. A., Lin, R. C. S. and Chapin, J. K. (1995). Sensorimotor encoding by synchronous neural ensemble activity at multiple levels of the somatosensory system, *Science* **268**: 1353–1358.

Nunez, P. L. (1981). *Electric Fields of the Brain: The Neurophysics of EEG*, Oxford University Press, Oxford.

Okuhara, D. Y. and Beck, S. G. (1994). 5-HT-1A receptor linked to inward-rectifying potassium current in hippocampal CA3 pyramidal cellss, *J. Neurophysiol.* **71**: 2161–2167.

Olshausen, B. A. and Field, D. J. (1996). Emergence of simple-cell receptive fields by learning a sparse code for natural images, *Nature* **381**: 607–609.

Park, M. R., Kita, H., Klee, M. R. and Oomura, Y. (1983). Bridge balance in intracellular recording; introduction of the phase sensitive method, *J. Neurosci. Meth.* **8**: 105–125.

Penfield, W. and Kristiansen, K. (1951). *Epileptic Seizure Patterns*, Charles C. Thomas, Springfield.

Penrose, R. (1989). *The emperor's new mind: Concerning computers, minds, and the laws of physics*, Oxford University Press, New York.

Peters, A. (1987). Number of neurons and synapses in primary visual cortex, *in* E. G. Jones and A. Peters (eds), *Cerebral Cortex Volume 6: Further aspects of cortical function, including hippocampus*, Plenum Press, New York, pp. 267–294.

Potter, H. and Butters, N. (1980). An assessment of olfactory deficits in patients with damage to prefrontal cortex, *Neuropsychologia* **18**: 621–628.

Press, W. H., Teukolsky, S. A., Vetterling, W. T. and Flannery, W. P. (1992). *Numerical Recipes in C: The Art of Scientific Computing*, Cambridge University Press, New York.

Price, J. L. (1973). An autoradiographic study of complementary laminar patterns of termination of afferent fibers to the olfactory cortex, *J. Comp. Neurol.* **150**: 87–108.

Price, J. L., Carmichael, S. T., Carnes, K. M., Clugnet, M., Kuroda, M. and Ray, J. P. (1991). Olfactory input to the prefrontal cortex, *in* J. L. Davis and H. Eichenbaum (eds), *Olfaction: A model system for computational neuroscience*, MIT Press, Cambridge, Massachusetts, pp. 101–120.

Pusch, M. and Neher, E. (1988). Rates of diffusional exchange between small cells and a measuring patch pipette, *Pfülgers Arch.* **411**: 204–211.

Racine, R. J., Ivy, G. O. and Milgram, N. W. (1989). Kindling: clinical relevance and anatomical substrate, *in* T. G. Bolwig and M. R. Trimble (eds), *The Clinical Relevance of Kindling*, John Wiley and Sons, Chichester, pp. 15–34.

Rall, W. (1964). Theoretical significance of dendritic tree for input-output relation, *in* R. F. Reiss (ed.), *Neural theory and modeling*, Stanford University Press, Stanford, pp. 73–79.

Rall, W. (1969). Time constants and electrotonic length of membrane cylinders and neurons, *Biophys. J.* **9**: 1483–1508.

Rall, W. (1989). Cable theory for dendritic neurons, *in* C. Koch and I. Segev (eds), *Methods in Neuronal Modeling: From Synapses to Networks*, MIT Press, Cambridge, pp. 9–62.

Raming, K., Krieger, J., Strotmann, J., Boekhoff, I., Kubick, S., Baumstark, C. and Breer, H. (1993). Cloning and expression of odorant receptors, *Nature* **361**: 353–356.

Ranck, J. B. (1973). Studies on single neurons in dorsal hippocampal formation and septum in unrestrained rats. I. behavioral correlates and firing repertoires, *Exp. Neurol.* **41**: 462–531.

Rapp, M., Segev, I. and Yarom, Y. (1994). Physiology, morphology, and detailed passive models of guinea-pig cerebellar Purkinje cells, *J. Physiol.* **474**: 101–118.

Rapp, M., Yarom, Y. and Segev, I. (1992). The impact of parallel fiber background activity on the cable properties of cerebellar Purkinje-cells, *Neural Comp.* **4(4)**: 518–533.

Regan, L. J. (1991). Voltage-dependent calcium currents in purkinje cells from rat cerebellar vermis, *J. Neurosci.* **11(7)**: 2259–2269.

Rieke, F., Bodnar, D. and Bialek, W. (1995). Naturalistic stimuli increase the rate and efficiency of information transmission by primary auditory neurons, *Proc. R. Soc. Lond. Ser. B.* **262**: 259–265.

Rieke, F., Warland, D., de Ruyter van Steveninck, R. and Bialek, W. (1997). *Spikes: Exploring the neural code*, MIT Press, Cambridge, Massachusetts.

Roddey, J. C. and Jacobs, G. A. (1996). Information theoretic analysis of dynamical encoding by filiform mechanoreceptors in the cricket cercal system, *J. Neurophysiol.* **75**: 1365–1376.

Rodriguez, R. and Haberly, L. B. (1989). Analysis of synaptic events in the opossum piriform cortex with improved current-source density techniques, *J. Neurophysiol.* **61(4)**: 702–718.

Rolls, E. T. (1994). Brain mechanisms for invariant visual recognition and learning, *Behav. Proc.* **33**: 113–138.

Roman, F., Staubli, U. and Lynch, G. (1987). Evidence for synaptic potentiation in a cortical network during learning, *Brain Res.* **418**: 221–226.

Sah, P. (1995). Different calcium channels are coupled to potassium channels with distinct physiological roles in vagal neurons, *Proc. Royal Soc.-B* **260(1357)**: 105–111.

Sayer, R. J., Friedlander, M. J. and Redman, S. J. (1990). The time course and amplitude of EPSPs evoked at synapses between paris of CA3/CA1 neurons in the hippocampal slice, *J. Neurosci.* **10(3)**: 826–836.

Sayer, R. J., Redman, S. J. and Andersen, P. (1989). Amplitude fluctuations in small EPSPs recorded from CA1 pyramidal cells in the Guinea pig hippocampal slice, *J. Neurosci.* **9(3)**: 840–850.

Schoenbaum, G. and Eichenbaum, H. (1995). Information coding in the rodent prefrontal cortex. I. Single-neuron activity in orbitofrontal cortex compared with that in pyriform cortex, *J. Neurophysiol* **74**: 733–750.

Segal, M. and Bloom, F. (1976). Norepinephrine in the rat hippocampus. III. Stimulation of the locus coeruleus in the awake rat, *Brain Res.* **107**: 499–511.

Sik, A., Penttonen, M., Ylinen, A. and Buzsàki, G. (1995). Hippocampal CA1 interneurons: An *in vivo* intracellular labeling study, *J. Neurosci.* **15(10)**: 6651–6665.

Singer, W. (1993). Synchronization of cortical activity and its putative role in information processing and learning, *Ann. Rev. Physiol.* **55**: 349–374.

Slotnick, B. M., Kufera, A. and Silberberg, A. M. (1991). Olfactory learning and odor memory in the rat, *Physiol. and Behav.* **50**: 555–561.

Spruston, N., Schiller, Y., Stuart, G. and Sakmann, B. (1995). Activity dependent action potential invasion and calcium influx into hippocampal CA1 dendrites, *Science* **268**: 197–300.

Staley, K. J., Otis, T. S. and Mody, I. (1992). Membrane-properties of dentate gyrus granule cells - A comparison of sharp microelectrode and whole-cell recordings, *J. Neurophysiol.* **67(5)**: 1346–1358.

Strassberg, A. F. and DeFelice, L. J. (1993). Limitations of the Hodgkin-Huxley formalism: Effects of single channel kinetics on transmembrane voltage dynamics, *Neural. Comp.* **5**: 843–855.

Stuart, G. and Sakmann, B. (1995). Amplification of EPSPs by axosomatic sodium-channels in neocortical pyramidal neurons, *Neuron* **15(5)**: 1065–1076.

Stuart, G. J. and Sakmann, B. (1994). Active propagation of somatic action potentials into neocortical pyramidal cell dendrites, *Nature* **367**: 69–72.

Tanabe, T., Iino, M. and Takagi, S. F. (1975). Discrimination of odors in olfactory bulb, pyriform-amygdaloid areas, and orbitofrontal cortex of the monkey, *J. Neurophysiol.* **38**: 1284–1296.

Theodore, W. H. (1992). *Surgical Treatment of Epilepsy*, Elsevier, Amsterdam.

Theunissen, F., Roddey, J. C., Stufflebeam, S., Clague, H. and Miller, J. P. (1996). Information theoretic analysis of dynamical encoding by four primary sensory interneurons in the cricket cercal system, *J. Neurophysiol.* **75**: 1345–1364.

Traub, R. D., Whittington, M. A., Colling, S. B., Buzsáki, G. and Jefferys, J. G. R. (1996a). Analysis of gamma rhythms in the rat hippocampus *in vitro* and *in vivo*, *J. Physiol.* **493**: 471–484.

Traub, R. D., Whittington, M. A., Stanford, I. M. and Jefferys, J. G. R. (1996b). A mechanism for generation of long-range synchronous fast oscillations in the cortex, *Nature* **383**: 621–624.

Traub, R. D., Wong, R. K. S., Miles, R. and Michelson, H. (1991). A model of a CA3 hippocampal pyramidal neuron incorporating voltage-clamp data on intrinsic conductances, *J. Neurophysiol.* **66(2)**: 635–650.

Treves, A. and Rolls, E. T. (1994). Computational analysis of the role of the hippocampus in memory, *Hippocampus* **4**: 374–391.

Tseng, G. and Haberly, L. B. (1989a). Deep neurons in piriform cortex. II. Membrane properties that underlie unusual synaptic responses, *J. Neurophysiol.* **62**: 386–400.

Tseng, G. F. and Haberly, L. B. (1988). Characterization of synaptically mediated fast and slow inhibitory processes in piriform cortex in an *in vitro* slice preparation, *J. Neurophysiol.* **59(5)**: 1352–1376.

Tseng, G. F. and Haberly, L. B. (1989b). Deep neurons in piriform cortex. I Morphology and synaptically evoked-responses including a unique high-amplitude paired shock facilitation, *J. Neurophysiol.* **62(2)**: 369–385.

Tsien, R. W., Lipscombe, D., Madison, D. V., Bley, K. R. and Fox, A. P. (1988). Multiple types of neuronal calcium channels and their selective modulation, *Trends Neurosci.* **11**: 431–438.

Uneyama, H., Mitsutoshi, M. and Akaike, N. (1993). Caffeine response in pyramidal neurons freshly dissociated from rat hippocampus, *Brain Res.* **604**: 24–31.

Vanier, M. C. and Bower, J. M. (1993). Differential effects of norepinephrine on synaptic transmission in layers Ia and Ib of rat olfactory cortex, *in* F. H. Eeckman and J. M. Bower (eds), *Computation and Neural Systems*, Kluwer Academic Publishers, Norwell, Massachusetts, pp. 267–271.

von der Malsburg, C. and Schneider, W. (1986). A neural cocktail-party processor, *Biol. Cybern.* **54**: 29–40.

Weiner, N. (1949). *Extrapolation, interpolation, and smoothing of stationary time series*, John Wiley and Sons, Inc., New York.

Wessel, R., Koch, C. and Gabbiani, F. (1996). Coding of time-varying electric field amplitude modulations in a wave-type electric fish, *J. Neurophysiol.* **75**: 2280–2293.

Westenbroek, R. E., Hell, J. W., Warner, C., Dubel, S. J., Snutch, T. P. and Catterall, W. A. (1992). Biochemical properties and subcellular distribution of an N-type calcium channel $\alpha 1$ subunit, *Neuron* **9**: 1099–1115.

Whittington, M. A., Traub, R. D. and Jefferys, J. G. R. (1995). Synchronized oscillations in interneuron networks driven by metabotropic glutamate receptor activation, *Nature* **373(16)**: 612–615.

Wilson, C. J. (1992). Dendritic morphology, inward rectification, and the functional properties of neostriatal neurons, *in* T. McKenna, J. Davis and S. F. Zornetzer (eds), *Single Neuron Computation*, Academic Press Inc., New York, pp. 141–171.

Wilson, M. and Bower, J. M. (1988). A computer simulation of olfactory cortex with functional implications for storage and retrieval of olfactory information, *in* D. Anderson (ed.), *Neural Information Processing Systems*, American Institute of Physics, New York, pp. 114–126.

Wilson, M. and Bower, J. M. (1991). A computer simulation of oscillatory behavior in primary visual cortex, *Neural Computation* **3**: 498–509.

Wilson, M. and Bower, J. M. (1992). Cortical oscillations and temporal interactions in a computer simulation of piriform cortex, *J. Neurophysiol.* **67**: 981–995.

Woolley, D. E. and Timiras, P. S. (1965). Prepyriform electrical activity in the rat during high altitude exposure, *Electroencephalogr. Clin. Neurophysiol.* **18**: 680–690.

Yamada, W. M., Koch, C. and Adams, P. R. (1989). Multiple channels and calcium dynamics, *in* C. Koch and I. Segev (eds), *Methods in Neuronal Modeling: From Synapses to Networks*, MIT Press, Cambridge, Massachusetts, pp. 97–134.

Yang, Q. X., Dardzinski, B. J., Li, S., Eslinger, P. J. and Smith, M. B. (1997). Multi-gradient echo with susceptibility inhomogeneity compensation (MGESIC): Demonstration of fMRI in the olfactory cortex at 3.0 T, *Magnetic Resonance in Medicine* **37**: 331–335.

Zador, A. M., Agmon-Snir, H. and Segev, I. (1995). The morphoelectrotonic transform: A graphical approach to dendritic function, *J. Neurosci.* **15(3)**: 1669–1682.

Zatorre, R. J. and Jones-Gotman, M. (1991). Human olfactory discrimination after unilateral frontal or temporal lobectomy, *Brain* **114**: 71–84.

Zatorre, R. J., Jones-Gotman, M., Evans, A. C. and Meyer, E. (1992). Functional localization of human olfactory cortex, *Nature* **360**: 339–340.

Zhang, L. and Krnjević, K. (1993). Whole-cell recording of anoxic effects on hippocampal neurons in slices, *J. Neurophysiol* **69**: 118–127.